SAND2016-1594R

SANDIA REPORT

SAND2016-XXXX
Unlimited Release
Printed February, 2016

Basic Research of Intrinsic, Tamper Indication Markings and Patterns Defined by Pulsed Laser Irradiation: Final Report

David P. Adams
Ryan D. Murphy
Samantha K. Lawrence
David J. Saiz
V. Carter Hodges
Neville R. Moody
Catherine Sobczak
Cole Yarrington
Geneva Neiser
Steven M. Yalisove (University of Michigan)
David F. Bahr, Professor (Purdue University)

Prepared by
Sandia National Laboratories
Albuquerque, New Mexico 87185 and Livermore, California 94550

Sandia National Laboratories is a multi-program laboratory managed and operated by Sandia Corporation, a wholly owned subsidiary of Lockheed Martin Corporation, for the U.S. Department of Energy's National Nuclear Security Administration under contract DE-AC04-94AL85000.

Issued by Sandia National Laboratories, operated for the United States Department of Energy by Sandia Corporation.

Available to DOE and DOE contractors from
U.S. Department of Energy
Office of Scientific and Technical Information
P.O. Box 62
Oak Ridge, TN 37831

Telephone: (865) 576-8401
Facsimile: (865) 576-5728
E-Mail: reports@osti.gov
Online ordering: http://www.osti.gov/scitech

Available to the public from
U.S. Department of Commerce
National Technical Information Service
5301 Shawnee Rd
Alexandria, VA 22312

Telephone: (800) 553-6847
Facsimile: (703) 605-6900
E-Mail: orders@ntis.gov
Online order: http://www.ntis.gov/search

SAND2016-XXXX
Unlimited Release
Printed February 2016

Basic Research of Intrinsic, Tamper Indication Markings and Patterns Defined by Pulsed Laser Irradiation: Final Report

David P. Adams, Ryan D. Murphy, Samantha K. Lawrence*, David J. Saiz, V. Carter Hodges, Neville R. Moody*, Catherine Sobczak, Cole Yarrington, Geneva Neiser
Sandia National Laboratories
P.O. Box 5800
Albuquerque, New Mexico, 87185; *Livermore, CA, 94550

Steven M. Yalisove
Department of Materials Science and Engineering
University of Michigan
Ann Arbor, Michigan, 48109

David F. Bahr
Department of Materials Science and Engineering
Purdue University
West Lafayette, Indiana, 47907

Abstract

Pulsed laser irradiation has been used to create complex, intrinsic markings that can be used as unique identifiers for authentication and asset protection. Markings have been made on the surface of various materials by rapidly scanning a focused laser beam across a designated area as large as several square inches. Markings include macro-scale patterns, such as barcodes, that contain encrypted information. More complex markings are comprised of macro-scale patterns and embedded, unique micro-scale features. Micro-scale features form spontaneously during scanned laser irradiation and have different shapes, spacings, color and other characteristics that are virtually impossible to recreate. The macro-scale patterns can be interrogated rapidly in the field using a digital camera, while the embedded micro-scale features are best evaluated in the laboratory using microscopy or related optical techniques. Interrogated markings are compared with archived maps of the original patterns (obtained at the time of their manufacture) to

determine component authenticity. The majority of experiments have involved marking planar solids. A new instrument that marks non-planar substrates is described for future work.

Color markings have been produced on a variety of metals and alloys including bulk solids and thin film coatings. Multicolor patterns are made by rapidly scanning nanosecond-pulsed, focused, infrared (1064 nm) laser light across a surface at different rates. Color arises from oxide layers produced by pulsed laser heating in air as one or more metal species reacts with oxygen and/or nitrogen. A target color can be obtained by proper choice of accumulated fluence. The origin of color is attributed to the combined effects of oxide layer thickness, the layer's refractive index, its defect structure, and the spectral reflectance of underlying metal. The colors of oxide layers can be differentiated by the human eye when viewed at a constant angle; laboratory instruments such as spectrophotometry and ellipsometry fully resolve the spectral response of features. Intrinsic, microscale color islands form within macro-scale color markings. In many cases, these smaller features have a unique color compared with surrounding regions of uniformly laser-treated material, and their varied shape, size, spacing, and chromaticity can be archived as unique identifiers. The long-term performance of laser grown oxide layers has been assessed by completing mechanical testing (scratch, indentation), corrosion resistance experiments (salt spray, salt water immersion), and high temperature aging. Color markings are created without degradation to underlying material.

A second form of laser-fabricated marking includes periodic hill-and-valley surface morphology, referred to as ripples. Surface ripples are created by ultrashort-pulsed laser irradiation. All tested materials form ripples, suggesting this alternative laser marking technology can be applied to virtually all solids. Ripples form near asperities that are initially present on the initial surface or at roughness created in a first laser pass. Our team has investigated the detailed light-solid interactions that give rise to periodic surface structures. Research includes a.) a first determination of the picosecond timescales associated with ripple formation, b.) a study of how Fresnel diffraction of scattered light leads to ripple formation, c.) discovery of how laser light polarization direction influences ripple wavevector, and d.) investigation of how surface plasmon polaritons can locally modify ripple wavelength by affecting the local electric field within an irradiated area. Surface ripple markings can be tailored in ways that make them useful as barcodes, similar to color patterns. Ripple markings also contain irregular characteristics that make them difficult to recreate.

Most of the completed research is included in this report. DTRA year – end reviews and published papers may be consulted for additional information.

ACKNOWLEDGMENTS

The research team greatly appreciates the support of Calvin Shipbaugh (DTRA program manager) and Dianna Balir (Sandia manager). The authors acknowledge the assistance of M. Rye and A. Kilgo for sample preparation, P. Kotula for transmission electron microscopy, J. Griego for X-ray diffraction, R. Goeke for ellipsometry and M. Hobbs for finite element model simulations. This work was supported by the Defense Threat Reduction Agency, Basic Research Award # IACRO 10-4257I, to Sandia National Laboratories. Sandia National Laboratories is a multi-program laboratory managed and operated by Sandia Corporation, a wholly owned subsidiary of Lockheed Martin Company, for the United States Department of Energy's National Nuclear Security Administration under Contract DE-AC04-94AL85000.

CONTENTS

FIGURES

TABLES

NOMENCLATURE

α	Thermal Diffusivity
a	Major Radius
A	Area
a_c	Contact Radius
AES	Auger Electron Spectroscopy
AFM	Atomic Force Microscopy
Al	Aluminum
ASTM	American Society for Testing Materials
at.%	Atomic Percent
Au	Gold
b	Minor Radius
BAA	Broad Agency Announcement
bal.	Balance
Bi	Bismuth
C	Carbon
C_l	Heat Capacity of Liquid
CIE	Commission Internationale de l'Eclairage
cm	Centimeter
C_p	Heat Capacity
CP	Commercially Pure
Cr	Chromium
CSM	Continuous Stiffness Module
CTE	Coefficient of Thermal Expansion
Cu	Copper
ρ	Density
ρ_o	Initial Density
D	Heat Diffusivity
dB	decibel
DC	Direct Current
DIC	Differential Interference Contrast
DCM	Dynamic Contact Mode
DOE	Department of Energy
DSC	Differential Scanning Calorimetry
DTRA	Defense Threat Reduction Agency
^oC	Degrees Celsius
ΔH	Energy
ΔH_{fus}	Enthalpy of Fusion
ΔH_0	Heat of Formation
ΔT_m	Melting Range
E	Energy, Modulus
ECR	Electrical Contact Resistance
EDX, EDS	Energy Dispersive X-ray Spectroscopy
EELS	Electron Energy Loss Spectroscopy

EMA	Effective Medium Approximation
E_p	Energy per Pulse
Er	Erbium
E_r	Reduced Modulus
eV	Electronvolt
F	Fluence
Fe	Iron
F_{acc}	Accumulated Fluence
FIB	Focused Ion Beam
F_p	Single Pulse Fluence
fs	Femtosecond
FWHM	Full Width at Half Maximum
GIXRD	Grazing Incidence X-ray Diffraction
GPa	GigaPascal
H	Hardness
h	Film thickness
HAADF	High Angle Annular Dark Field
HAZ	Heat Affected Zone
Hz	Hertz
I	Current
In	Indium
IR	Infrared
k	Thermal Conductivity, Dielectric Constant
K	Kelvin
K-K	Kramer-Kronic
kHz	KiloHertz
κ_s	Thermal Conductivity
kV	Kilovolt
l	Liquid (subscript)
λ	Wavelength
LIPSS	Laser Induced Periodic Surface Structure
LLC	Limited Liability Company
m	Meter
mg	Milligram
min.	Minute
mm	Millimeter
Mn	Manganese
Mo	Molybdenum
μm	Micrometer
ms	Millisecond
n	Refractive Index
N	Newton, Nitrogen
Ni	Nickel
nm	Nanometer
N_p	Number of Pulses
ns	Nanosecond

O	Oxygen
ν	Repetition Rate, Poisson's ratio
ζ	Rayleigh Length
P	Power, Phosphorous
P_{avg}	Average Power
ps	Picosecond
Pt	Platinum
ϕ_m	Threshold Fluence for Melting
QS	Quasi-Static
R	Reflectance, Reflectivity
R_p	Complex Fresnel reflection coefficient for p- polarized light
R_s	Complex Fresnel reflection coefficient for s-polarized light
s	Second
S	Sulfur
S_a	Surface Roughness
SEM	Scanning Electron Microscopy
Si	Silicon
Sn	Tin
SNL	Sandia National Laboratories
sr	Steradian
SS304L	Stainless Steel 304L
STEM	Scanning Transmission Electron Microscope
t	Time
T	Temperature
T_o	Initial Temperature
TEM	Transmission Electron Microscopy
Ti	Titanium
$T_{liquidus}$	Liquidus Temperature
$T_{solidus}$	Solidus Temperature
τ_l	Pulse Length
θ_m	Melting Temperature
UV	Ultraviolet
V	Vanadium
V	Volume
V	Volt
W	Watt
w_o	Beam Waist
wt.%	Weight Percent
XRD	X-ray Diffraction
XRF	X-ray Fluorescence

1. BACKGROUND OF PROPOSED WORK

The research described herein was initially proposed in response to DTRA broad agency announcement (BAA): HDTRA1-08-10-BRCWMD-Service Call, Basic Research for Combating Weapons of Mass Destruction. Specifically, our proposal addressed the objectives of Topic Per4-F: Novel Materials for Unattended Sensing to Support Future Treaties (Thrust 5). This includes a desire to "identify microscale and nanoscale structures and phenomena in materials that can provide passive or active indicators of interference with unattended monitoring or sensing, to support compliance with treaties."

Our approach included study of how short and ultra-short pulses of laser light interact with the surfaces of various materials to create complex markings, or 'fingerprints', for potential use as tamper indicators - one step in the interference path. Produced markings are considered passive indicators of interference, for these do not actively report back status or state-of-health. A passive marking, nonetheless, is recognized as an important and relatively inexpensive deterrent to those intent on counterfeiting or tampering with a critical asset. Complex markings can be very difficult to duplicate by existing methods or replicate by alternative processes, and this is likely to be understood by an adversary.

With the original proposal we hypothesized that

- short and ultra-short pulsed lasers can be used to create different types of markings including color layers as well as periodic, nanometer-scale surface morphologies, and

- the formation of markings depends intrinsically on the interaction of light with material structure present prior to laser irradiation such that the variations present on a starting surface should lead to variations in the final marking that make it difficult to replicate or duplicate.

Depending on the application, markings may contain tailored patterns (i.e., programmed elements). An example of this is a barcode that contains encrypted information such as date of manufacture, country of origin, date or receipt, etc. that is read out in the field for identification. Markings that also contain unique, identifying features (perhaps embedded within patterns) add significant complexity and value as a deterrent. Of particular interest, features that form spontaneously due to an irregular interaction between light and solid are of great value as unique identifiers. There are many dynamic laser-solid interactions that can give rise to a local variation in the marking even when a focused laser beam of fixed power is scanned uniformly across a solid. For example, the beam may mark the local surface area in a different way if it encounters irregular surface topography, secondary phases, grains of different crystallographic orientation, or compositional variations. Owing to the randomness of a starting surface, these types of features should be virtually impossible to duplicate or replicate. One would have to begin anew with the same starting surface to achieve the final marking.

Figure 1 depicts an envisioned application of pulsed laser marking. In this drawing, a macro-scale color pattern is being created over a portion of the package/lid containing an integrated circuit. Rastering across different locations at various programmed velocities, a laser beam programs a complex, color pattern. Each of the square pixels in the example pattern have a single average color. In addition, there were envisioned to be micro-scale islands that have

different, readily identifiable colors – compared with surrounding areas. The produced macro-scale pattern and a map of color islands could be archived at the time of its manufacture for comparison during inspection at a later date. In one implementation, the macro-color pattern could be used solely to include encrypted information. In a second approach, the color pattern could also be used as a map to efficiently guide interrogation of particular pixels filled with color islands, whereby the size, spacing and color of islands are evaluated to compare with archived information. A color pattern can thus indicate tamper. For example, a color pattern made on a reversible seal (such as solder) would undoubtedly be disturbed during de-soldering resulting in a different appearance. On the other hand, a match to archived patterns could build confidence that such an event did not occur.

Throughout this document, the word 'intrinsic' refers to markings that are created in the surface of a given material or component. It is expected that intrinsic markings are more robust than external labels applied with adhesives. Intrinsic features are built into the component or material and are difficult to remove without significantly affecting the surrounding volumes.

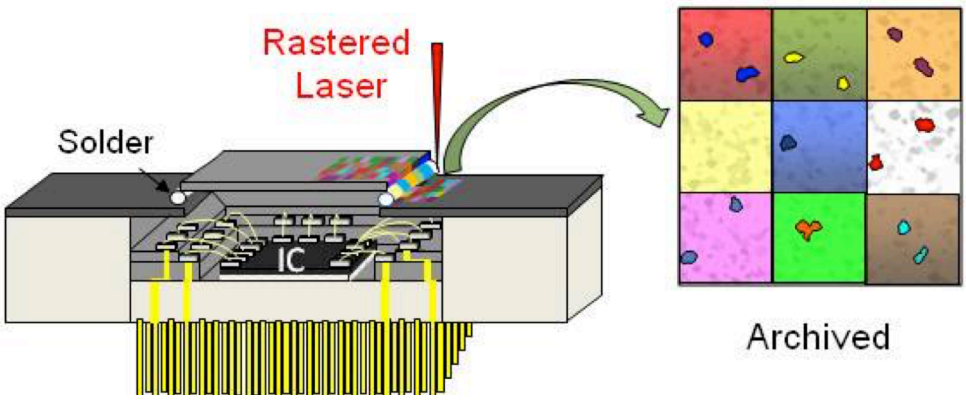

Figure 1. An envisioned application, wherein a pulsed laser creates a tailored, macro-scale color pattern across the lid and package of a microelectronic. Inspection of macro-scale color pixels reveals intrinsic, site-specific colored features.

In general, our research team has explored the fundamental physics and chemistry associated with laser irradiation and marking of various surfaces. This includes a study of the phase, microstructure, composition, stability, mechanical properties, and optical properties of colored oxide layers. In some cases, we document processes that can be used to build color patterns. The origin of periodic, nanometer - scale surface topography is also investigated using ultrafast pump-probe optical microscopy. Site-selective formation of laser-induced periodic surface structures (LIPSS) is demonstrated. A high level goal of our work identifies laser-marking methods that minimize the thermal load and residual strain on a marked component. The pulse duration, pulse energy and repetition rate are chosen to avoid significant thermal 'heat' load and associated effects.

2. GENERAL APPROACH

Our team envisioned several types of markings throughout the course of research. In general, markings include programmed patterns as well as embedded, unique identifiers.

Figure 2 includes a macro-scale color marking comprised of nine square pixels. Each pixel has a single major color that is commanded using archived, material-specific laser processes determined through study. Irregularly spaced and differently sized color islands are contained within many of the square pixels for added complexity as unique identifiers. As shown later in this report, the colors of islands are different than their immediate surroundings despite receiving the same laser fluence. In other cases, the pixels may have no color islands.

In Figure 3, a different type of laser-fabricated, macro-scale color marking is shown. It does not include color islands, however the scan lines associated with a translated beam are evident. The scan direction has been varied within each square color pixel to add complexity. Scan line direction along with scan hatch, i.e., spacing between lines, can be varied. The scan profile can readily be tailored with modern laser systems either by using precision sample stages or through the use of computer-controlled, galvanometric steering mirrors. Compared with that shown in Figure 2, the marking in Figure 3 does not include elements of randomness. No color islands are formed. Instead, all features of the pattern commanded by the laser operator making this particular marking less difficult to recreate.

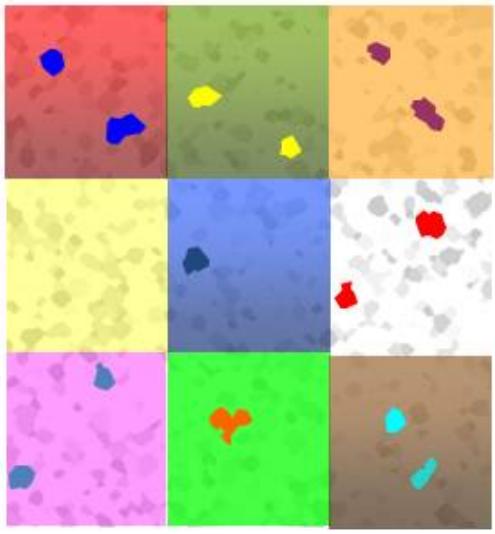

Figure 2. Depiction of a laser-defined, macro-scale color pattern having irregularly-positioned, embedded microscale color islands. The color islands have a unique chromaticity compared with their immediate surroundings.

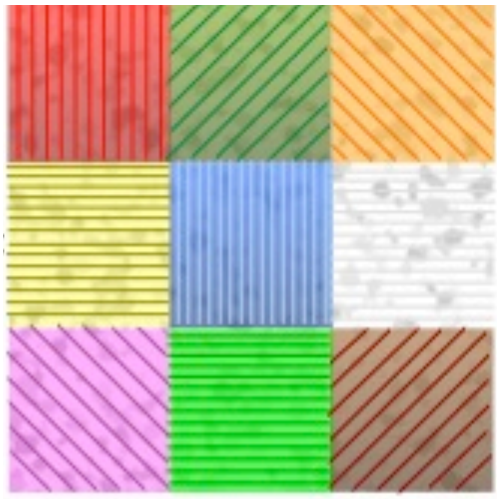

Figure 3. Depiction of a laser-defined, macro-scale color pattern having prescribed laser scan lines that vary in direction and hatch across the pattern.

Figure 4 shows a colorless marking composed of periodic surface morphology (called ripples) forming in isolated areas. Fourteen modified locations have formed ripples as a laser is scanned across the field of view. In this depiction, ripples are shown with black lines indicating a parallel hill-and-valley modulation is present on a surface. One such area is circled in 'red'. Our research demonstrates that a scanned, ultrashort-pulsed beam creates the hill-and-valley surface morphology (ripples) at asperities present on the starting surface; this includes both protrusions and depressions. If the initial surface is well polished (meaning Angstrom level roughness), there may be insufficient protrusions and depressions for ripple formation. However, a first laser scan can be used to decorate this type surface with rough features that will nucleate ripples on a second scan. This particular marking was made using a single laser light polarization direction, which generally aligns the ripple wave vector (vertical for the marking shown in Figure 4).

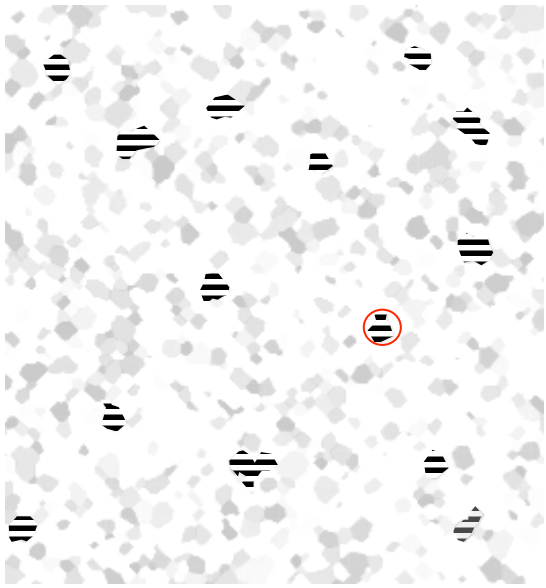

Figure 4. Depiction of a laser-marked surface that is composed of periodic surface ripples in localized regions.

Figure 5 shows a more complex colorless marking that builds on the ideas of Figure 4. A three-by-three square array is arranged similar to the earlier examples. Each discrete region (referred to as a pixel) differs from its neighbors by having a unique ripple wave vector orientation. Predominately set by programming the polarization direction of the incident laser light, the ripple orientation can be changed in different areas. There are several irregular characteristics in this marking including the location of ripple patterns (which varies according to the initial location of asperities on the starting surface) and the wavelength of surface ripples. The latter effect is attributed to the degree of surface plasmon polariton excitation and its effects on changing the electric field at a microscopic site of marking. The varying amplitude of surface ripple patterns is a third characteristic of topography that can be archived.

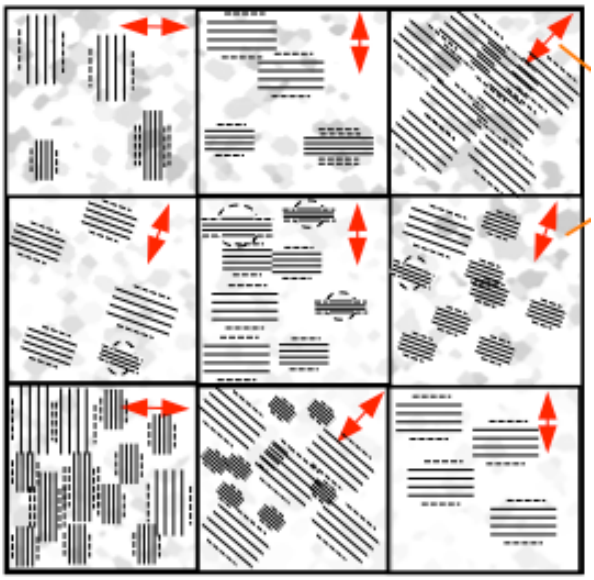

Figure 5. Depiction of a laser-marked surface that is composed of periodic surface ripples in localized regions. Laser light polarization direction (indicated with red arrows) is varied during beam scanning to tailor ripple wave vector within square pixels.

3. OBJECTIVES

The tasks stated in the original proposal were:

Task 1: Research of color layer formation during pulsed laser irradiation (Year 1) The awardees shall begin with an investigation of pulsed laser colorization. We shall start with pulse durations in the hundreds of nanoseconds - consistent with previous studies (sub-task 1.1). Next, we should utilize temporal lengths on the order of tens of nanoseconds in order to explore improved thermal management strategies (sub-task 1.2). The awardees shall demonstrate pixel-by-pixel definition of color layers in multiple material surfaces. Likely, this will utilize an Er-doped glass fiber laser with galvanometric deflection and control software. Repetition rate should also be a variable in these experiments. We should investigate thin film growth in at least two ambient environments: air and nitrogen. The awardees shall investigate the properties of color layers. This should include phase, optical properties and through-thickness structural uniformity (or non-uniformities) (sub-task 1.3).

Task 2: Research of laser-induced periodic surface structures (LIPSS) (Year1) The awardees shall research the temporal evolution of laser-induced periodic surface structures on initially smooth surfaces. After qualifying a pump-probe instrument (sub-task 2.1), we should use ultrafast pump-probe microscopy to investigate the timescales for laser-induced periodic surface structure formation (sub-task 2.2). We should investigate low-spatial frequency structures during this period. Additional characterization of the evolving surface profile will involve scanning and transmission electron microscopy.

Task 3: Modeling of Heat-Affected Zones (HAZs) (Year 1) The awardees shall implement required software/code that simulates heat affected zones as a function of laser process parameters (sub-task 3.1). We should include pulse duration and repetition rate. We should complete a thermal modeling code that can simulate the effects of laser irradiation as a function of pulse duration (excludes femtosecond regime), repetition rate, energy per pulse and incident wavelength in different target materials.

Task 4: Research of the mechanical properties of color layers (Year 1) The awardees shall research the mechanical properties (hardness and modulus) of color layers fabricated using approximately one hundred nanosecond - pulse length laser light (sub-task 4.1). These coatings should be analyzed using nanoindentation test methodologies. We should characterize the hardness and the modulus of laser-defined oxide layers fabricated on Ti and 300 series stainless steel.

Task 1: Research of color layer formation during pulsed laser irradiation (Year 2) The awardees shall investigate the site-selective formation of colors at the surfaces of various materials (sub-task 1.4). We should start with alloys and composites composed of different phases. We should test polycrystalline metals. Also, we should vary pulse durations from single nanoseconds to approximately 1 picosecond (sub-task 1.5). Varying repetition rate, we should explore the effectiveness of creating colors while seeking improved thermal management strategies that minimize thermal strain effects.

Task 2: Research of laser-induced periodic surface structures (LIPSS) (Year 2)

This work consists of two parts. First, the awardees shall continue with an investigation of the temporal evolution of low-frequency surface structures formed on initially polished surfaces (sub-task 2.2). Second, the awardees shall investigate the site-selective formation of periodic structures (sub-task 2.3). We should investigate how laser-induced periodic surface structures vary with phase, grain orientation, and the presence of grain boundaries. We should investigate how the initial surface roughness leads to site-selectivity.

Task 3: Modeling of heat-affected zones (HAZs) (Year 2) The awardees shall investigate, through modeling, the effects laser process parameters have on heat affected zone dimensions and temperature excursions (sub-task 3.2). We should vary pulse length from microseconds to single nanosecond lengths. These models will ultimately be the basis for chemical kinetic codes that predict color layer formation, etc. and the site variability in growth rates (when irradiating multi-phase materials).

Task 4: Research of the mechanical properties of color layers (Year 2) The awardees shall research the through-thickness toughness of color layers fabricated by pulsed laser irradiation (sub-task 4.2). This should involve nanoindentation. Specimens should be processed using different laser parameters.

Task 3: Thermal modeling of heat affected zones (HAZs) (Year 3)

The awardees shall investigate the effects of scanning a pulsed laser beam over a surface (sub-task 3.3) for the purpose of laser colorization. Materials to be modeled should include

monolithic substrates, monolithic substrates with a partially-fabricated oxide layer, and a substrate composed of two phases (sub-task 3.4).

Task 4: Research of the mechanical properties of color layers (Year 3) The awardees shall research the interfacial toughness of color layers fabricated by pulsed laser irradiation (sub-task 4.3). Specimens should be processed using different laser process parameters. Characterization should involve stressed superlayer techniques or four-point bend tests.

Task 5: Research how pulsed lasers can combine color layers with nanoscale laser-induced periodic surface structures (LIPSS) (Year 3)

The awardees should research 1.) laser-induced periodic surface structure formation during a single laser treatment also used for colorization (sub-task 5.1), 2.) the challenge of growing color layers over the top of pre-defined laser induced roughness (sub-task 5.2) and 3.) whether rough structures can be generated at substrate-film interfaces after colorization (sub-task 5.3).

Task 6: Research the stability/metastability of color layers and laser-induced periodic surface structures (LIPSS) (Year 3) The awardees shall investigate the stability and metastability of color layers and laser induced surface structures (sub-tasks 6.1 and 6.2). This should involve accelerated aging test methodologies (time, temperature). If changes in color occur, we should correlate these with phase and composition.

Additional tasks were added for extended years of research as follows. This information was included in the Addendum to the Statement of Work submitted May 28, 2014.

Task 7: Research of micro-spectrophotometry for inspection and validation of laser color markings (Option Year) The awardees shall investigate the reflectance signatures of laser-fabricated color markings using a microspectrophotometer in order to determine the potential of this method for rapid, unambiguous verification of authenticity. We shall start with color oxide patterns produced on stainless steel 304L that are comprised of color islands and surrounding matrix material (of a second, distinguishable color). We will evaluate whether color islands have unique spectral signatures compared to surrounding material. Our work will also determine the minimum size of islands that can be resolved optically with this technique. We will then expand this study to include laser color markings made on other materials such as titanium alloy.

Task 8: Investigate new laser fabrication techniques that produce color markings with improved corrosion resistance (Option Year) The awardees shall investigate new methods for fabricating corrosion-resistant color markings. This includes, but is not limited to, color markings made on stainless steel and titanium alloy. We will start with an investigation of multi-pass laser scan processes for attaining thick, crack-free, color oxide coatings. Experiments will scan a focused laser beam across a specimen at low fluences and repeat this until a desired larger thickness and color are attained. (It is anticipated that this method will avoid large thermal excursions) Additionally, we will investigate de-focused laser beam scanning as a method for growing color oxides to desired thickness and avoid oxide layer

cracking. The corrosion resistance of newly produced color features will be evaluated by either salt-water immersion or salt spray exposure tests.

Task 9: Research new methods for laser marking curved surfaces (Option Year) The awardees shall investigate laser marking of curved surfaces. This will include the creation of color markings as well as periodic ripple topography markings. This should involve the use of a 532 nm or a 1064 nm pulsed laser. The awardees will investigate an expanded set of materials including copper and aluminum. This research will utlize a modified galvo-mirror set that maintains a focused beam across the targeted non-planar surface. We will determine the curvature limits to laser marking of nonplanar surfaces.

Task 10: Complete model simulations of laser-induced ripple formation – involves an ElectroMagnetic field solver (Option Year) The awardees shall investigate the complex light-solid interactions that give rise to periodic ripple topography on a surface when irradiated by a laser. Specifically, the University of Michigan student will team with Sandia National Laboratories' staff to evaluate the fundamental mechanisms giving rise to periodic topography. This should involve a numerical modeling approach (COMSOL). We will investigate the relative roles of light polarization, surface plasmon polaritons, and Fresnel diffraction on forming periodic surface features. The awardees should predict the characteristic wavelength and orientation (i.e., wave vector) of surface ripples. Tests in the laboratory will validate model predictions.

4. NANOSECOND PULSED LASER COLOR MARKING OF METALS AND ALLOYS

4.1. Background

Laser stimulated oxidation has long been recognized as a method that can modify the appearance of metal and alloy surfaces. However, its application as a reliable marking technology has been limited by a lack of stable laser output, reproducible processes, and a thorough understanding of the laser-solid interactions underlying surface modification. Early attempts to reliably mark a surface with color were confounded by unstable laser output. With the advent of modern lasers that offer control of pulse power, pulse duration, and repetition rate, there is renewed interest to improve upon prior work and fully develop laser color marking technology.

Laser color marking generally refers to techniques that involve laser irradiation of a surface whereby one or more substrate species react with oxygen, nitrogen or other process gas to produce a semi-transparent (colored) coating. Layer growth is most often described as a pyrolytic process whereby a substrate or a growing film is heated via light absorption and this energy stimulates reactions [1,2]. Wautelet explains that growth in air involves gas-phase transport, chemisorption, interdiffusion, and chemical reactions [1]. Under certain conditions, photolytic processes also contribute to the growth of an oxide or a nitride layer. For example, plasma generated by high-intensity, pulsed laser radiation includes excited gaseous species that can interact with substrate metal atoms [2]. The many atomic-scale processes that contribute to pyrolytic and photolytic growth often occur at different rates, resulting in a dynamic series of events. A change in

thickness can be accompanied by an evolving absorption coefficient, and the resultant changes in heating rate can increase, decrease [3] or oscillate [4,5] the growth rate.

This Section describes our research of laser color marking various metals and alloys. Stainless steel 304L, commercially pure titanium, titanium alloy, copper and a few other alloys used as seals (Kovar™ and Georo) have been colored in a controlled manner. The origin of color has been investigated for a few of these materials. The detailed microstructure, composition and phase of laser-grown oxide layers is presented to shed light on observed colors. Ellipsometry has been used to probe the detailed optical properties of laser-grown oxide layers and demonstrate the importance of defect structure and the role of an underlying substrate. This thin film characterization technique elucidates how structure of the produced oxide layer varies with incident laser fluence. The changes to underlying metal are also included. Evidence for site-specific color islands is presented, confirming our initial hypothesis.

4.2. Experimental Setup

4.2.1. Laser, optics and stage

Laser color marking involved a SPI Lasers LLC, 20 Watt fiber laser (model SP-20P-HS-B-D-A-B). This particular instrument was chosen for its excellent stability, tunable pulse energy and compact size. Several parameters are controlled through software, including average power, frequency (0 to 500 kHz), and pulse duration (from 9 ns to 200 ns) making it amenable to research. This laser outputs at a wavelength of 1064 nm, consistent with manufacturer's specification.

Emitted coherent light passes through a variable beam expander and on to two galvanometer mirrors (Nutfeld model XLR8-10mm-1064nm). The mirrors are computer-numerically controlled to steer the beam across a specimen at a fixed rate or at different rates in different areas. The steering mirrors direct the beam of light into a Linos f-theta lens before irradiating a specimen. This setup is shown in Figure 6.

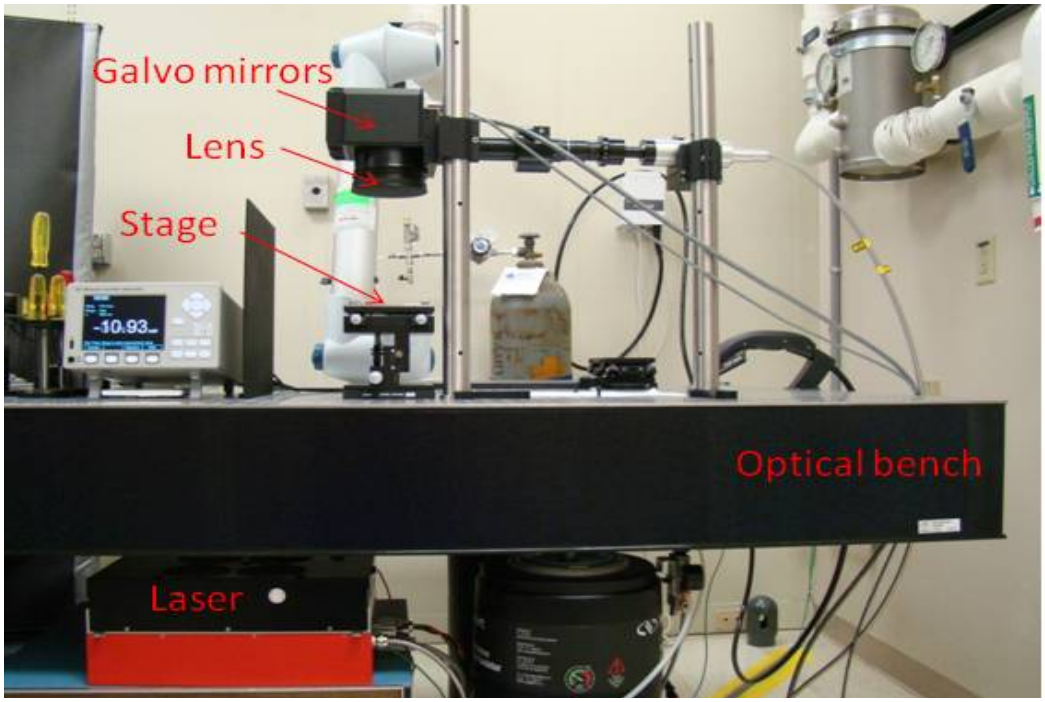

Figure 6. Photographic image of the pulsed laser setup used for laser color marking.

Two f-theta lenses were utilized for research. Lenses are listed in Table 1 along with the corresponding measured spot widths and calculated Rayleigh lengths. For a Gaussian beam propagating in free space, the Rayleigh length, ζ, is

$$\zeta = \pi w_o^2 / \lambda \qquad \text{Eq. 1}$$

where w_0 is the beam waist (or size of the beam at its narrowest point) and λ is the wavelength. Different lenses allow us to vary focused spot size. Spot size can be estimated by irradiating a polished specimen along a single line using the same laser process parameters planned for coloring. After irradiation the marked specimen is inspected optically, and an average line width is determined. The beam width and overall shape are more accurately determined using a beam profiler (DataRay Inc. WinCamD 14-bit beam profiling CCD camera). Beam shape was profiled at different working distances to evaluate Rayleigh length, also specified in Table 1.

Table 1. Specifications of the two lenses and spot sizes used for laser coloring.

Lens ID	f number	Calculated Rayleigh length	Measured spot size (at focus)	Working Distance
Linos f-theta #1	163	4.2 mm	57 μm when using 10 W	18.5 cm
Linos f-theta #1	163	4.2 mm	51 μm when using 5 W	18.5 cm
Linos f-theta #2	254	12.4 mm	65 μm when using 10 W	29.7 cm

The temporal profiles of pulses emitted by the SPI laser were quantified using a Thorlabs DET 210 high-speed silicon detector and a fast oscilloscope. Throughout this report, pulse duration is stated as a full-width-at-half-maximum value.

A scanned beam approach was used for all laser color marking experiments. A focused laser beam is scanned across a specimen while maintaining a fixed average power, pulse duration, and pulse frequency (repetition rate). Color layers were most often made using a single-pass procedure with significant beam overlap (depicted in Figure 7). This means that the beam is scanned over a sample once without repeated scanning, but there is significant beam overlap in subsequent, neighboring lines. As an example the f163 lens generates a Gaussian beam with a

FWHM of ~ 60 μm. With hatch equal to 10 μm, a given microscopic area is therefore irradiated six times when implementing an overlapped, scanned line approach.

Scan speed is commanded in the range of ~10 to ~800 mm/sec when laser color marking metals and alloys. Referenced speeds listed in figures and text are the values measured at a target surface. Most experiments involve scanning in one direction. Upon completion of a single line, a shutter blocks the beam until the mirrors return the beam to the start position of the next line. It is expected that this unidirectional scan approach should minimize differences in thermal history, and, compared with an alternative, down-and-back (boustrophedonic) scan mode, color should be more uniform. The delay between concluding one line and re-positioning the beam for a subsequent line is ~ 1 ms when scan line length is 4 mm. As the focused beam is steered across a planar specimen, the lens-to-sample working distance changes. In order to ensure that the fluence at the target remains unchanged for a given scan speed, our team has limited the maximum distance traveled on target such that the optical path length differences due to sweeping the beam is less than the Rayleigh length. A tip – tilt stage was used to level samples for uniform marking.

Single pass irradiation was completed in air having a relative humidity of 15 – 20 %.

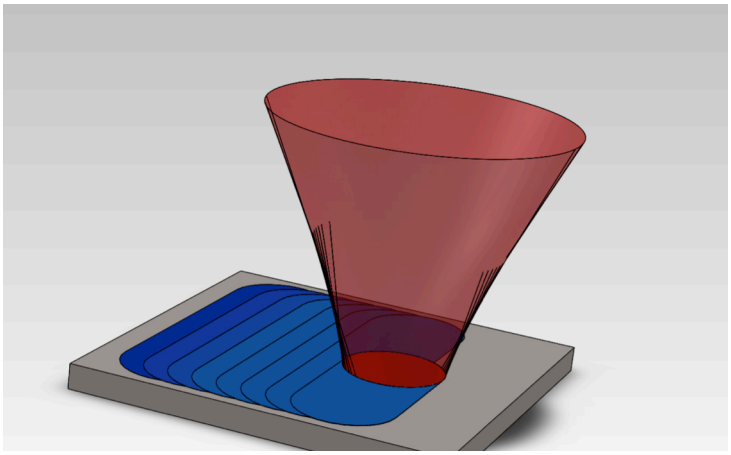

Figure 7. Depiction of the scanned laser approach used for coloring the surfaces of metals and alloys. The focused laser beam is shown in red. The produced oxide layer is blue.

4.3. Laser Coloring Bulk Solids

4.3.1. Sample Preparation and Analytical Instruments

Bulk samples of different area and thickness were used for laser marking research. A list of these materials is included in Table 2, along with the laser process parameters used to fabricate color markings.

Table 2. List of bulk materials colored using nanosecond pulsed lasers and the laser process parameters used.

Material	Measured Reflectivity (%)@1064nm	Average Power[+] (W)	Pulse Frequency (kHz)	Pulse Duration (ns)	Beam Expander/ Lens
SS304L	0.73	5.6; 6.6; 7.6	225	102 ± 2	8X/f163
SS304L	0.73	5.6	225	10 ± 0.5	8X/f163
SS304L	0.73	5.6	250,275,300,350	102 ± 2	8X/f163
Ti (CP2)	0.57	5.6; 6.6; 7.6; 8.6; 9.6; 10.6; 11.6	225	102 ± 2	8X/f163
Ti (CP2)	0.57	5.6; 6.6; 7.6; 8.6; 9.6; 10.6; 11.6	225	102 ± 2	8X/f254
Ti-6Al-4V	0.37	5.6	225	102 ± 2	8X/f163
*Kovar™	0.63	4.0; 5.6; 7.6	225	102 ± 2	8X/f163
†Georo	0.74	5.6; 6.6	225	102 ± 2	8X/f163
Copper	0.97	6.6	225	102 ± 2	8X/f163

*Kovar is a trademark of Carpenter Technology Corporation. It is a nickel-cobalt ferrous alloy.
†Georo is a solder alloy composed of $Au_{0.88}Ge_{0.12}$.
+ Power is measured using a Newport model 1936C meter with a Newport 818P-030-19 detector

Stainless steel 304L samples were prepared from cold-drawn, square-stock SS 304L. The manufacturer reports this material to have a chemical composition (by wt%) as follows: 18.11% Cr, 8.00% Ni, 1.63% Mn, 0.42% Si, 0.14% Mo, 0.083%N, 0.025% S and P, 0.023% C, with the

balance as Fe. Steel samples were ground and polished using a Struers Abrapol-2 grinder/ polisher. Grinding involved 180 grit SiC paper, water lubricant and 100-150 N of force; and polishing used 9, 6 and 3 μm diamond suspension with lubricant and a force of ~100 N. Final cleaning involved rinsing in Lenium^{TM} degreasing solvent, followed by acetone and then alcohol. Final sample dimensions were 12.5 x 12.5 x 3.4 mm. A Veeco Instruments DEKTAK profilometer and an ADE Phase Shift white light interferometer reveal a surface roughness (S_a) of 8-25 nm.

Commercially pure, grade 2 (ASTM B265) titanium and Ti-6Al-4V alloy substrates were used for laser color marking experiments. All Ti-based test samples were ground and polished using a Struers Abrapol-2 grinder/ polisher to have final dimensions of 12.5 x 12.5 x 3.4 mm and a roughness (S_a) equal to 2-10 nm. Prior to laser marking, each test piece was cleaned by rinsing in Lenium^{TM} degreasing solvent, followed by acetone and alcohol.

Three other bulk materials were studied. This includes Kovar^{TM} (an alloy of Ni, Fe and Co), Cu, and Georo (a solder alloy composed of Au and Ge that melts at ~356^{o}C). The Kovar, Ti-6Al-4V alloy and OFE copper pieces were roughly the same dimension as the Ti listed above. The Georo used in this study was 250 μm-thick foil bonded by silver paint to stainless steel. The laser wavelength specific reflectivity of all bulk test materials was determined using a Varian Inc. Cary 5000 UV-Visible-IR spectrophotometer and hemispherical analyzer. Measured values are included in Table 2.

Transmission electron microscopy (TEM), Energy-dispersive X-ray spectroscopy (EDX), and X-ray diffraction (XRD) were used to evaluate oxide layer thickness, composition, and phase. Cross-section TEM/EDX samples were prepared in a FEI Co. Helios dual beam system using an

ex-situ, FIB lift-out method. FIB sections were aligned relative to the direction of laser scanning depending on the task at hand. Characterization involved a FEI Co. Titan G2 80-200 probe aberration corrected, transmission electron microscope operated at 200 kV. The system has an integral, 4-sensor, windowless, silicon drift X-ray detector array with a combined collection solid angle of 0.7 sr. The STEM detectors consist of a high-angle annular dark field (HAADF) detector and three solid-state detectors (one bright field and two annular dark field). The microscope has a spatial resolution of 0.08 nm and high sensitivity to soft X-ray lines providing an ability to distinguish between species. The energy resolution of the EDX detector is specified by the original manufacturer to be 134 eV for Mn Kα. The energy resolution for this instrument has been determined to be in the range of 80 - 89 eV (full-width at half-maximum) for Ti L, N K and O K lines. Chemical phases were identified by diffraction analysis and located using dark-field imaging methods. Phases formed by laser irradiation were confirmed using XRD. X-ray diffraction data were collected using a Bruker D8 diffractometer with a Hi-Star area detector. This system was configured with a sealed tube source (Cu Kα), an incident beam mirror optic (for removal of Cu Kβ radiation), and a 500 μm pinhole optic. Scanning electron microscopy (SEM) was used to evaluate the extent of laser heating in underlying metals and other characteristics. SEM involved a Zeiss Supra 55 VP electron microscope, unless otherwise mentioned.

The spectral reflectance of oxide coatings was evaluated using a Varian Inc. Cary 5000 UV-Visible-IR spectrophotometer. Samples were fixtured within an internal diffuse reflectance accessory (integrating hemisphere) such that the reflectance of individual color features could be measured. The unit was configured to include the specular beam in detection. Chromaticity was evaluated using the WIN UV Color software for the spectrophotometer, and CIE 1931 photopic observer and D65 illuminant standards were implemented for analysis.

4.3.2. Colored Markings on Stainless Steel

This section describes the variety of color markings that are produced on polished, stainless steel 304L substrates by scanned, IR laser irradiation. We start by describing the microstructural, compositional and phase changes that occur as a function of different laser process parameters. Afterwards, the discussion turns to the optical properties of produced oxide layers. Evidence for local color islands is presented, consistent with our initial hypothesis. The color and chromaticity of produced layers is documented.

4.3.2.1 Structure and Composition of Oxide Coatings

Experiments systematically varied the laser fluence over a large range (as shown in Figure 8) in order to determine the variety of colors that can be produced on the surface of SS 304L. In this plot, 'fluence' represents the amount of energy accumulated in a particular feature area. It is calculated using the following relationship

$$F_{acc} = E/A = E_p N_p/A = P_{avg} N_p /A\nu, \quad \text{Eq. 1}$$

where E_p is the energy per pulse and N_p is the total number of pulses used to create a 16 mm^2 area (A) feature. Energy per pulse is simply the average power divided by the repetition rate, or P_{avg}/ν. Fluences are included in Fig. 8 for the three average powers used for oxide growth, and F_{acc} spans a large range from ~85 to 4500 J/cm^2. Note: error bars that represent variations in accumulated fluence are smaller than the symbols used in this plot. A small fluence variation, < 2%, is estimated for directions perpendicular to beam travel, when accounting for the beam shape and the relatively small hatch.

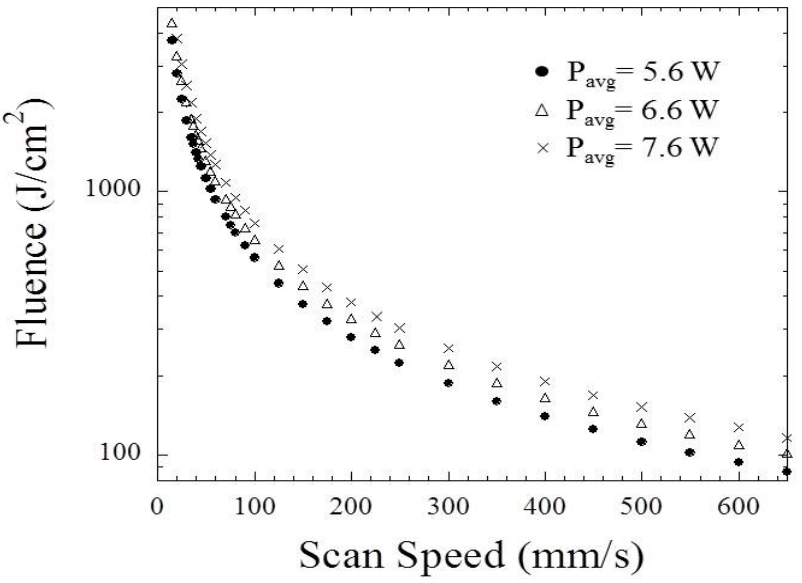

Figure 8. Plot of fluences used for laser-stimulated oxidation of stainless steel 304L. The abscissa indicates the laser scan speed at the surface of the specimen. Results are shown for three different average powers.

A representative oxide coating made using one set of laser process parameters (6.6 W, 300 mm/s; F_{acc} = 220 J/cm^2) is shown in Fig. 9 by cross section SEM. One can see a continuous oxide coating and a portion of the underlying substrate in this image. The coating appears as a dark layer with the bottom and top of this oxide marked using two arrows. SEM indicates that this laser-grown coating is approximately 230 nm thick, and no cracks are observed. There is a small variation in thickness as for other laser-fabricated oxides. The thin, faint coating adhered to the surface of the laser-grown oxide is a protective Pt film deposited as part of the FIB sectioning procedure. This SEM image is tilted vertically by 52^o with respect to the normal of the FIB-sectioned face.

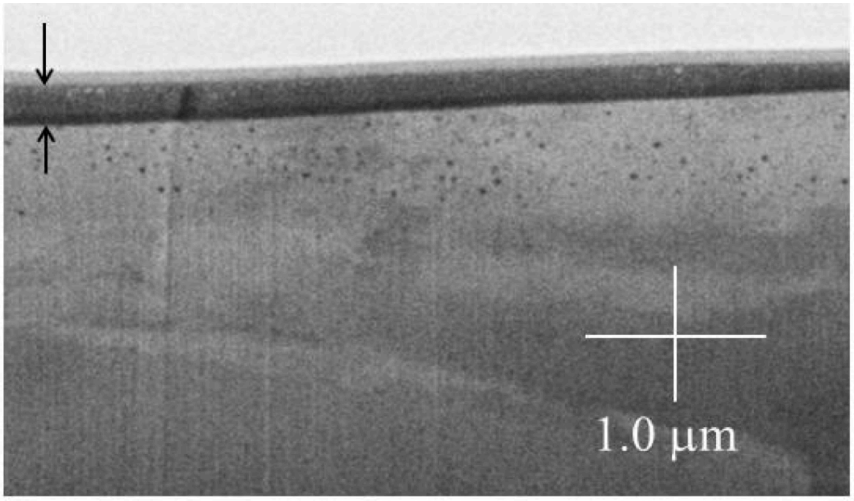

Figure 9. Scanning electron micrograph showing a portion of an oxide layer fabricated using P_{avg} = 6.6 W and a scan speed of 300mm/s.

Scanning electron micrographs like the one shown in Fig. 9 were used to determine an average oxide thickness and standard deviation for numerous oxide coatings. Thickness was measured at 25 equally spaced points per micrograph amounting to 75 measurements per color layer. Figure 10 plots the average thickness of oxide coatings versus laser scan speed for different P_{avg}. This plot of oxide thickness includes results from most experiments described in Fig. 8, covering a large range of accumulated fluence. Symbols represent average thickness, error bars represent one standard deviation of measured thickness, and the trend lines are guides to the eye for a particular P_{avg}.

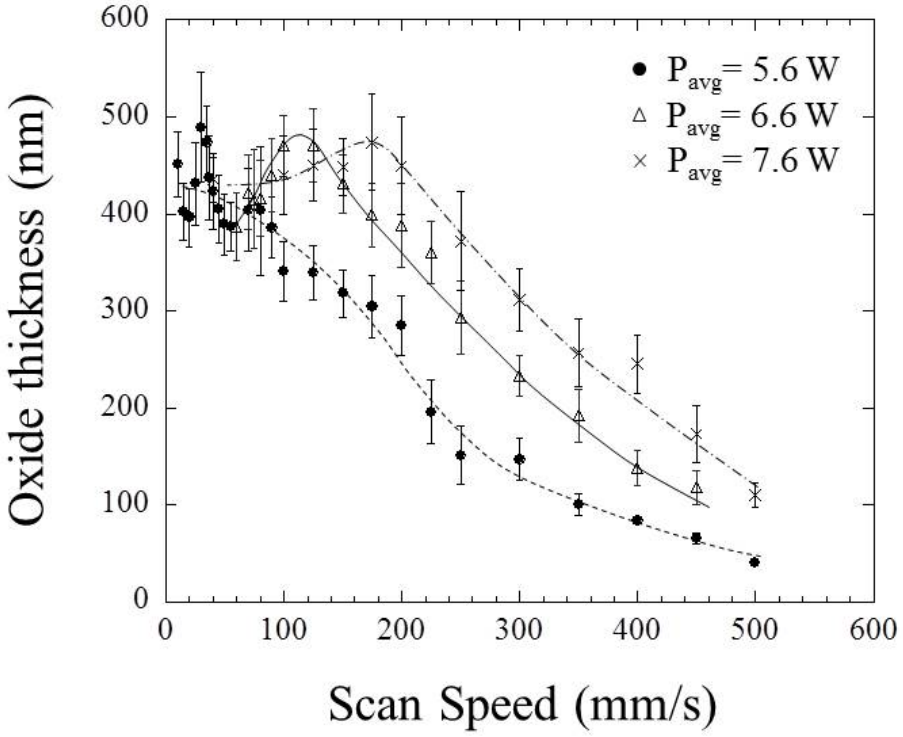

Figure 10. Plot of average oxide thickness measured by SEM. Thicknesses are plotted versus laser scan speed for different average laser powers.

Several trends are revealed with the data in Fig. 10. First, the thickness of continuous oxide coatings is in the range of ~20 to 500 nm. The larger scan speeds result in thinner oxides, because these coatings are made using a reduced fluence. Oxide thickness generally increases as scan speed is reduced, because more energy is directed to the surface. However, the oxide thickness does not increase above ~500 nm when using lower scan speeds (e.g., below 100 mm/s when using 6.6 W). Reduced oxide thicknesses at the lowest scan speeds are attributed to ablation. One observes fumes during laser irradiation when using the lowest speeds indicated in Figs. 8 and 10. Furthermore, measurements of oxide coating surface height referenced to the height of

surrounding, non-irradiated areas confirms mass loss in features created with F_{acc} > 800, 733 and 600 J/cm^2 for P_{avg} = 5.6, 6.6 and 7.6 W, respectively.

Turning to the composition of produced oxide coatings, TEM and EDS reveal several trends. Figure 11(a) shows a continuous oxide layer produced using P_{avg} = 5.6 W and scan speed = 42 mm/s (F_{acc} = 1333 J/cm^2). This particular oxide layer is on average approximately 400 nm thick and appears in Fig. 11(a) as a relatively dark volume compared with the underlying substrate. Individual grains are recognized within the oxide layer; grain widths are on the order of the oxide layer thickness. EDS shows that coatings are composed of Cr, Fe, Mn, Ni and O. Figure 11(b) shows three representative spectra obtained from different regions of the specimen marked in Fig. 11(a) using numbers of corresponding color. The spectrum obtained from the bottom half of this thick oxide coating reveals a Cr-rich oxide solution containing Mn, whereas the top half of this coating is an Fe-rich oxide. Composition maps in Fig. 11(c) and (d) additionally show compositional gradients through the thickness of these two regions. In terms of composition, this coating is similar to the 'duplex structure' that is reported to form during UV laser marking [6]. Regarding thinner coatings, having thicknesses < 200 nm, EDS demonstrates that the composition of the entire oxide is Cr-rich similar to the bottom half of thick coatings such as that shown in Fig. 11. Thin coatings contain Mn and some Fe; however, these do not include an Fe-rich oxide cap. Through thickness compositional gradients are still evident even in thinner laser-fabricated oxide coatings.

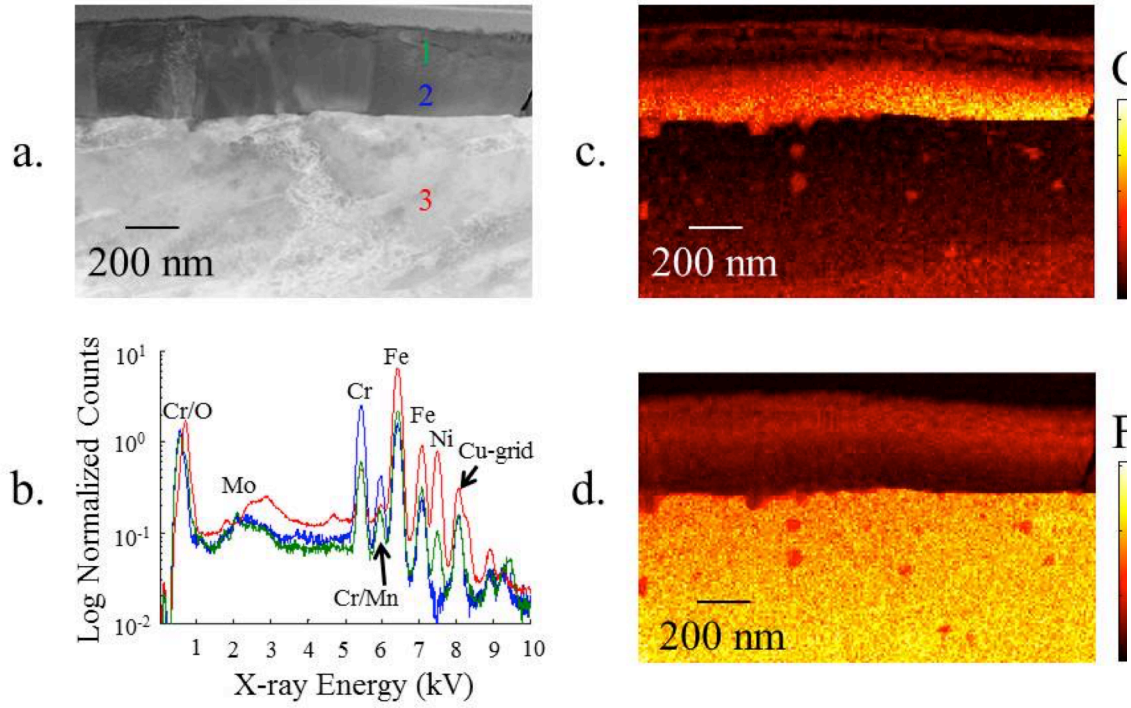

Figure 11. Cross section transmission electron micrograph in (a) shows a portion of an oxide layer grown on SS304L using an average power of 5.6 W and speed of 42 mm/s. Spectra in (b) were obtained from three different points identified in the micrograph using colored numbers. Images (c) and (d) map the Cr and Fe compositions.

X-ray micro-diffraction shows that many of the oxide layers created on SS 304L form a crystalline phase. As indicated in Fig. 12(a) for 5.6 W experiments, several diffraction peaks not associated with the original austenite structure emerge beginning at a scan speed of 150 mm/s (F_{acc} = 373 J/cm^2), and the peak intensities increase with reduced scan speed. The rather broad peak at $2\theta = 35.5^o$ is not consistent with the known reflections of stainless steel austenite or other forms of steel that may develop upon laser heating. Thus, the single peak at 35.5^o is attributed to a phase associated with the laser-grown oxide coating. Of note, the peak 2θ position is consistent with the

relatively intense (311) reflections of a few candidate spinel oxide phases including $MnCr_2O_4$ [7], $FeCr_2O_4$ [8] and Fe_3O_4 [9].

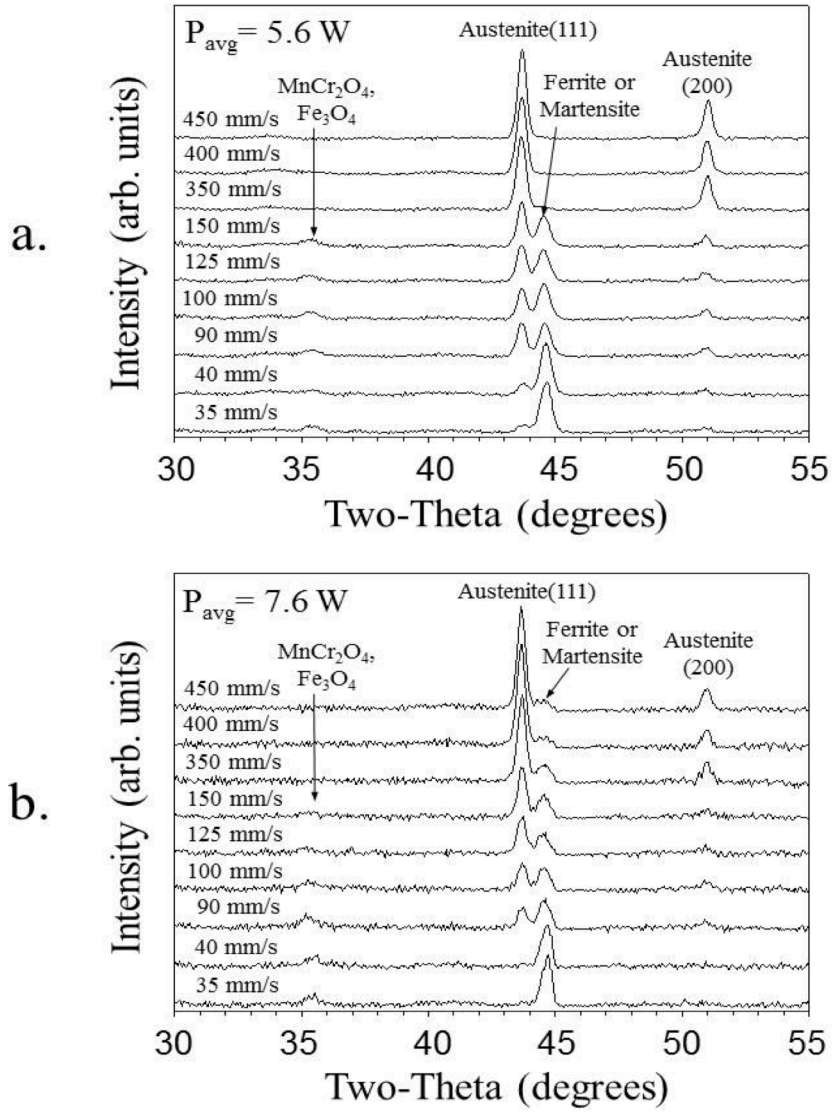

Figure 12. XRD patterns obtained from several laser-fabricated oxide layers grown on SS 304L. The rates listed over each pattern indicate the laser scan speed used for oxide growth.

In order to determine the crystalline oxide phase(s) formed in coatings during laser irradiation, cross-section samples were analyzed by selected area electron diffraction using a

transmission electron microscope. Figure 13 includes a selected area electron diffraction pattern obtained from multiple grains of the coating shown in Fig. 11. Multiple reflections are observed in this diffraction pattern, confirming that at least one crystalline phase is present. The electron diffraction patterns have been analyzed to determine the lattice spacings. These are listed in Table 3 for seven observed reflections. Considering that several metal oxide phases may have formed during laser treatment, comparisons were made to diffraction data of candidate phases including Fe_3O_4, $MnCr_2O_4$, $FeCr_2O_4$, Cr_2O_3, various manganese oxides and several intermetallics composed of the metal constituents.

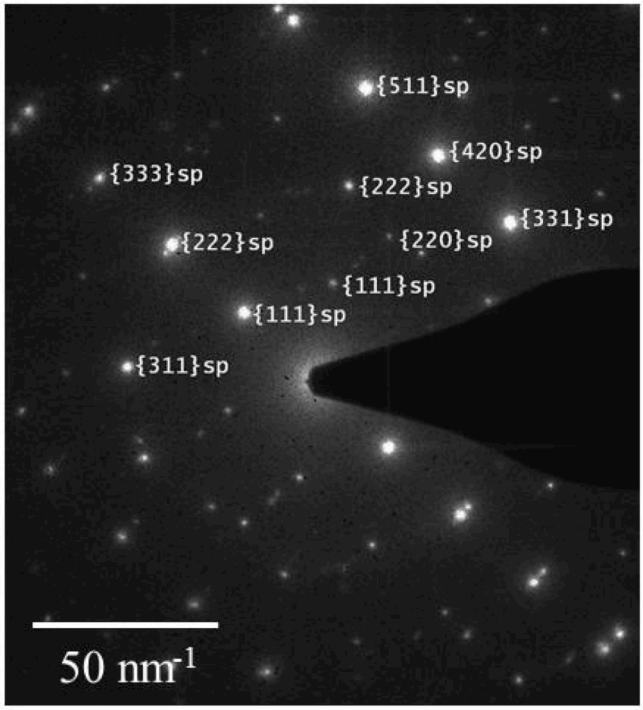

Figure 13. Selected area electron diffraction pattern obtained from a few grains composed within an oxide layer grown on SS 304L using an average power of 5.6 W and a speed of 42 mm/s. The reflections are indexed to the structure of a spinel phase having a = 8.40 Å.

The measured lattice spacings match closely to those of Fe_3O_4, $MnCr_2O_4$ and $FeCr_2O_4$, but are not consistent with those of Cr_2O_3 or various intermetallics. Fe_3O_4, $MnCr_2O_4$ and $FeCr_2O_4$ form similar spinel structures having a lattice parameter of approximately 8.40 Å [10-12]. In Table 3, the second and third columns include predicted lattice spacings for a spinel phase (having a Fd-3m space group) and a lattice parameter of 8.400 Å along with its allowed reflections. Excellent agreement is found when comparing the measured lattice spacings to those associated with the model spinel phase. For thick oxide layers having an Fe-rich oxide top half and a Cr-rich oxide bottom half, it is possible that two phases are present. If so, the top half is likely Fe_3O_4 and the bottom half is $MnCr_2O_4$. More detailed analysis is required to determine whether thinner oxide layers contain a single phase - possibly $MnCr_2O_4$.

Table 3. List of measured lattice spacings and those calculated for a Fd-3m space group with a = 8.40 Angstroms.

Measured spacing (Å)	Calculated spacing (Å)	Reflection {hkl}
4.85	4.849	111
2.98	2.969	220
2.53	2.533	311
2.41	2.425	222
2.09	2.100	400
1.94	1.927	331
1.62	1.617	333/511

4.3.2.2 Optical Properties of Oxide Coatings Fabricated on SS 304L

Oxide coatings created on laser irradiated SS 304L exhibit a variety of distinguishable colors. In Fig. 14, eight different color layers are shown on stainless steel samples. These oxide

layers were created using an average power of 5.6 W and different speed from 175 to 450 mm/s. Several colors are visible in this image. Colors are not saturated and appear diffuse to the eye.

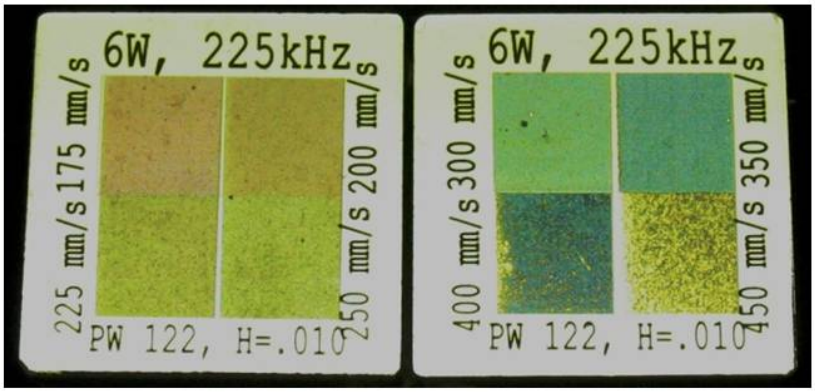

Figure 14. Optical micrograph showing several 4 x 4 mm color layers formed on SS 304L by scanned, pulsed laser irradiation in air. The measured power used for irradiation was equal to 5.6 W (listed as '6 W' commanded power on specimen). Scan speeds are listed.

Each of the 4 x 4 mm color layer features created by ns-pulsed laser irradiation have been examined by spectrophotometry to determine spectral reflectance. Compared with the human eye, spectrophotometry provides an unbiased determination of reflectance for different incident wavelengths. Implementing an integrating hemisphere for detection, one obtains reflectance spectra such as those shown in Fig. 15. In these plots, reflectance is plotted over a range of wavelengths from 350 to 700 nm. The reflectivity spectra of an unmodified SS 304L sample is also included in Fig. 15(a) for reference; this spectra is similar to that reported previously by another group [13]. The three colored coatings represented in Fig. 15(a) were grown using P_{avg} = 5.6 W and scan speeds of 600, 550 and 500 mm/s. These particular coatings developed small thicknesses of ~23, ~32 and 40 $\pm$ 5 nm, respectively.

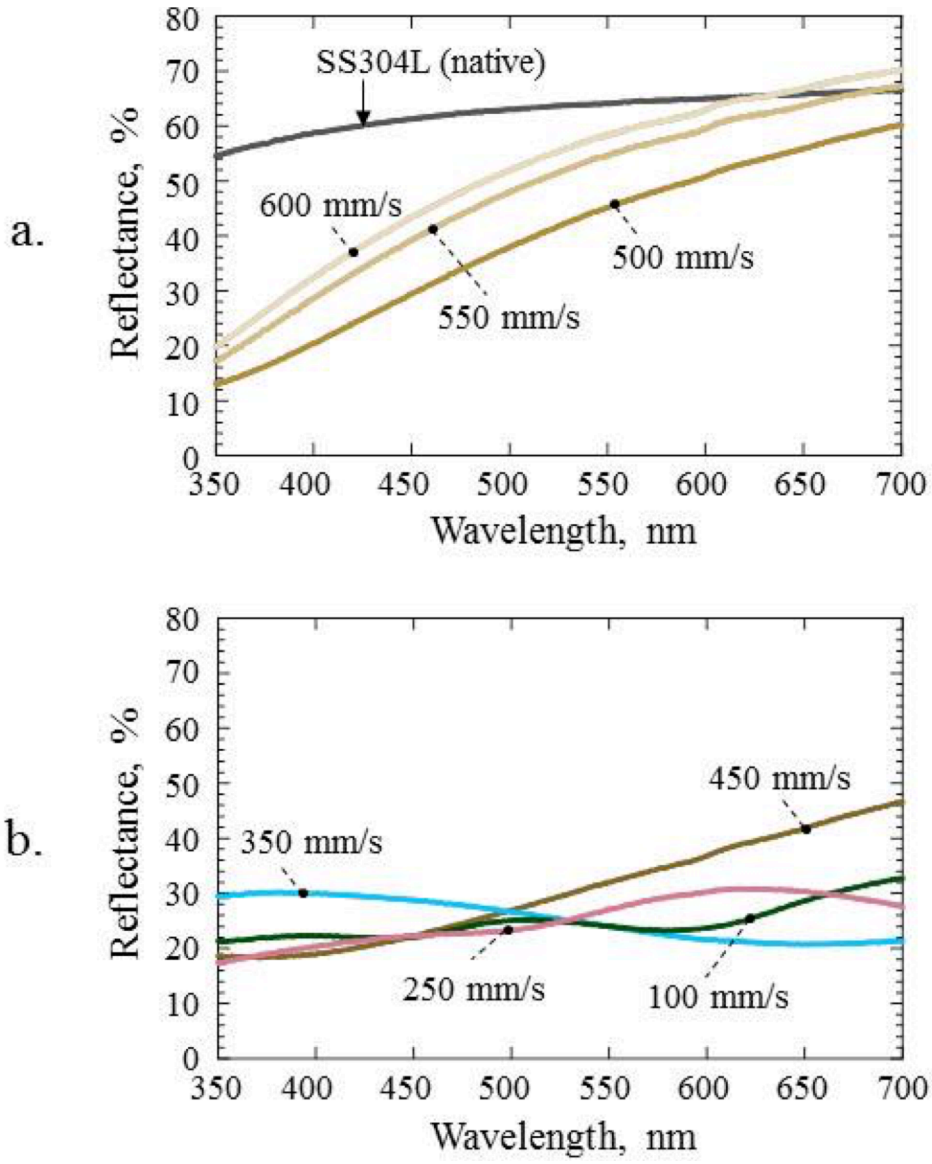

Figure 15. Plot (a) includes reflectance spectra from bare SS 304L and three thin metal oxide coatings made using P_{avg} = 5.6 W and scan speeds of 600, 550 and 500 mm/s. Plot (b) displays the reflectance spectra for four oxide coatings made using P_{avg} – 5.6 W and scan speeds of 450, 350, 250 and 100 mm/s.

As indicated in the spectra, the average reflectance of these continuous coatings was low. Reflectance was less than that obtained from SS 304L for almost all visible λ. Comparing the

optical properties of these three coatings, an increased oxide thickness led to decreased reflectance. It is expected that the reduced reflectance obtained from thin coatings is due to attenuation [14]. The three coatings described with Fig. 15(a) have a thickness that is less than ¼ λ for each of the incident wavelengths used for spectrophotometry. Therefore, interference effects should not play a large role.

On the other hand, the samples represented in Fig. 15(b) are likely affected by attenuation and interference. The thickness of the four oxide layers presented in this plot were much larger, ~65 $\pm$ 6, 100 $\pm$ 11, 285 $\pm$ 31 and 341 $\pm$ 31 nm, with thicker coatings forming with decreased scan speed. The spectra for the 450 mm/s oxide layer in Fig. 15(b) takes on the general shape of those shown in Fig. 15(a) although further reduced in reflected intensity consistent with a larger oxide thickness. The other three layers represented in Fig. 15(b) having oxide thickness $\geq$ 100 nm exhibit broad maxima and minima which suggests interference is prevalent. Thin film interference is a well-known effect that can influence the appearance of a semi-transparent oxide coating [15]. In general, interference involving the interaction of light scattered off the top surface of an oxide coating with light reflected from the substrate-coating interface can occur when the coating thickness is on the order of the wavelength of light incident on a specimen. Assuming that the index of refraction for oxide coatings is greater than that of the substrate [16], constructive interference is likely to occur when the oxide thickness is equal to $\lambda/4n$ where n is the index of refraction for the oxide [15]. Destructive interference would then occur when oxide thickness is equal to $2\lambda/n$ [15]. With characterization covering a large range of wavelength, constructive and destructive interference could manifest in a peak reflectance at a certain wavelength depending on oxide thickness. It is suggested that the peaks in reflectance in the spectra obtained from samples grown at 100, 250 and 350 mm/s are due to interference, because the thickness of these coatings is

on the order of the wavelengths of light used for characterization. Also consistent with this supposition, the peaks shift to higher wavelength when oxide thickness is made thicker. For example, compare the wavelengths (~ 350-400 nm) corresponding to a peak reflectance for the 350 mm/s oxide to the wavelength (~ 625 nm) that shows a peak reflectance for the thicker oxide grown using a laser scan speed of 250 mm/s.

In addition to reflectance, spectrophotometry was used to determine chromaticity – a second form of marking information that could ultimately be archived for protection against counterfeiting. Chromaticity is defined as a quality of color that is determined by hue and intensity [17]. Implementing the D65 illuminant standard and a CIE 1931 standard photophic observer, chromaticity was determined for each of the laser-grown color coatings. In Fig. 16, measured chromaticities are overlaid with the CIE 1931 color map [18,19]. This plot includes results for continuous coatings made on stainless steel 304L with different P_{avg} and scan speeds, covering the full range of thickness described in Fig. 10. For reference, a virgin SS 304L specimen exhibited a chromaticity of x = 0.315, y = 0.334.

This plot confirms that colors are not saturated as suggested by visual observations. Saturated colors would be indicated by a chromaticity that lies on the boundary of the CIE color diagram [17]. Instead, oxide layers fabricated on SS 304L form with a range of chromaticity from 0.29 to 0.38. The inset of this figure shows detectable differences in oxide sample chromaticity.

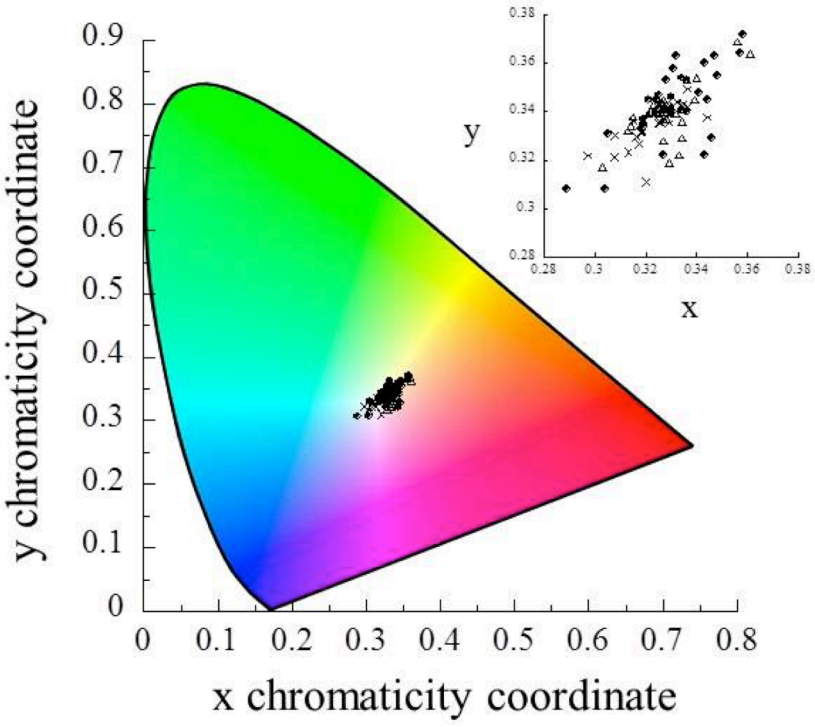

Figure 16. Chromaticity values for all oxide coatings made on SS 304L plotted over the CIE 1931 color space. Inset shows the same data over a limited range of chromaticity space. The symbols indicate the P_{avg} as follows: 5.6 W (●), 6.6 W (△) and 7.6 W (×).

4.3.2.3 Effects of Laser Heating on Underlying Stainless Steel Structure

Scanning electron microscopy and XRD have also been used to evaluate the changes to substrate structure and phase that result from laser irradiation and oxide growth. General observations by SEM show that substrate melting occurs for almost all laser processes used in this study. Examples of melting are shown in Fig. 17 for (a) a single line and (b) an area created using multiple, scanned lines. In these micrographs, the cross-sectioned samples are viewed perpendicular to the laser scan direction. A Gaussian-shaped melt zone is evident in Fig. 17(a).

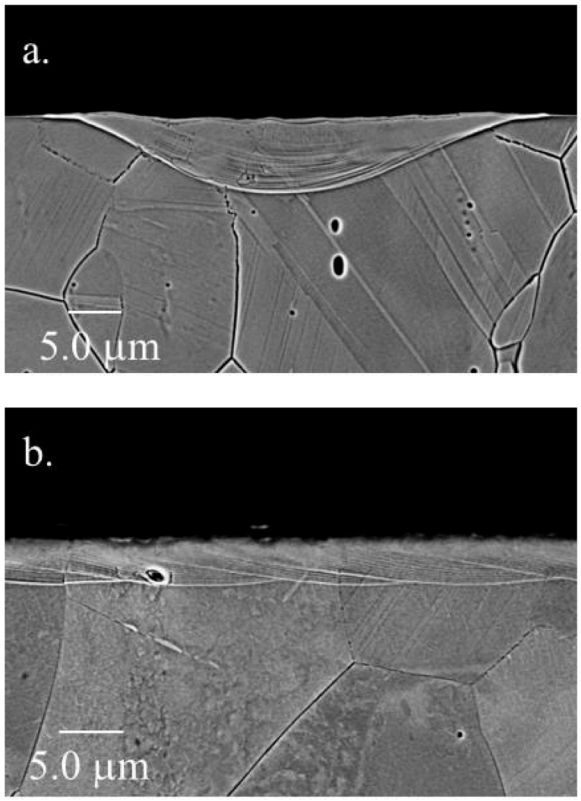

Figure 17. Cross section scanning electron micrographs showing the melt zones associated with (a) a single line of laser irradiation at 5.6 W and 30 mm/s and (b) multiple, spaced scans utilizing 6.6 W and 200 mm/s. Both metallographic sections are made transvers to the direction of laser scanning.

Multiple melt zone boundaries present in Fig. 17(b) are readily explained by the movement of a Gaussian-shaped, pulsed laser beam down a line such that the effects of individual melt/resolidification events are revealed. In addition, the resolidified structure presented in Fig. 17 shows evidence of epitaxy and a small amount of shrinkage porosity. An oxide layer covers the majority of the melted surface shown in Fig. 17(a). An oxide coating is not readily observed in Fig. 17(b) as this was inadvertently removed during sectioning.

Observations of substrate melting are consistent with predicted and measured pulsed laser melt threshold fluences for stainless steel. The single pulse threshold fluence for melting (ϕ_m) can be estimated using the theory by Bäuerle [2] and the expression

$$\phi_m = (\sqrt{\pi}/2)\kappa_s \theta_m (\tau_l / D)^{1/2} \quad \text{Eq. 2}$$

where κ_s is the thermal conductivity, θ_m is the melting temperature equal to 1700 K [20], τ_l is pulse length (119 ns) and D is heat diffusivity. Considering high temperature values for thermal conductivity and heat diffusivity (equal to 0.24 W $cm^{-1}K^{-1}$ and 0.041 cm^2s^{-1}, respectively [21]), Eq. 2 estimates ϕ_m = 0.61 J/cm^2. For our experiments, the single pulse fluence (F_p) can be expressed as

$$F_p = 2E_p/\pi ab = 2P_{avg}/\nu\pi ab \quad \text{Eq. 3}$$

where a and b represent the major and minor radii at $1/e^2$ intensity of the focused beam. For the three average powers used in this study, the estimated single pulse fluences are 1.8, 2.2 and 2.5 J/cm^2. Of note, these fluences are greater than the threshold for melting predicted by Eq. 2 as well as a previously-reported value (0.9 J/cm^2) determined by experiment [22].

SEM reveals that the composition and phase of melted / resolidified stainless steel change. As indicated in Fig. 11, Cr outdiffusion to form oxide layers reduced the composition of Cr in underlying, near-surface volumes. In Fig. 11(c), the Cr-composition map of the underlying substrate indicates substantial depletion of Cr to a depth of ~0.5 μm. EDS compositional analysis completed over larger areas indicates a reduced Cr concentration to depths as large as ~2.3 μm for

this specimen and other samples made with similar process parameters. Large Cr-denuded depths and melt depths result from laser irradiation as summarized in Fig. 18 for samples treated with 5.6 and 6.6 W. As shown in this plot, the Cr-denuded depth is generally equal to or less than the measured melt depth. Regarding other metal species that react to form metal oxide coatings, Fig.11(d) shows evidence for a decreased Fe concentration in the near-surface volume of substrates. Manganese was also depleted to similarly shallow depths. Measured melt depths are similar to values estimated by finite element model simulations.

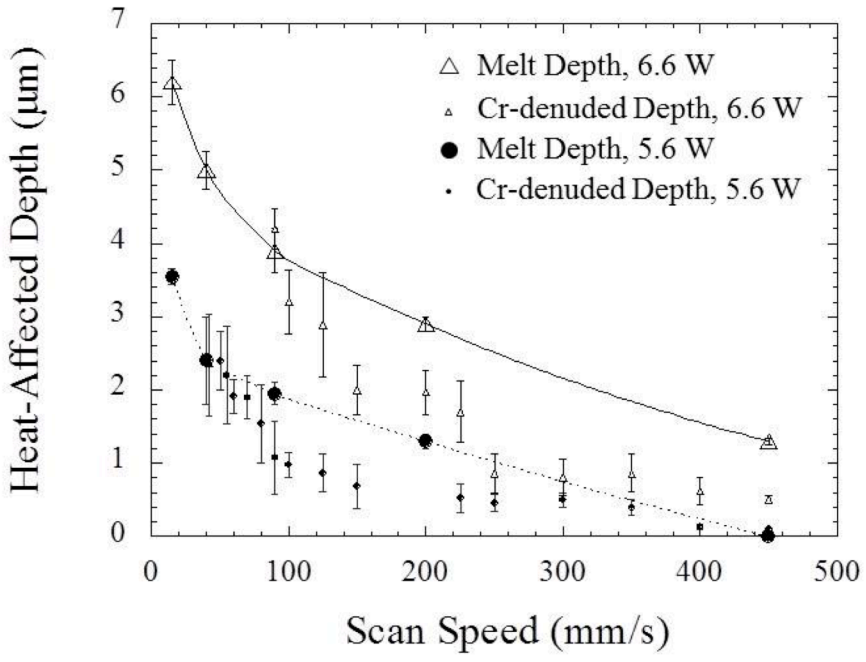

Figure 18. Cross section scanning electron micrographs showing the melt zones associated with (a) a single line of laser irradiation at 5.6 W and 30 mm/s and (b) multiple, spaced scans utilizing 6.6 W and 200 mm/s. Both metallographic sections are made transvers to the direction of laser scanning.

Within the heat-affected zone, the steel transforms from austenite to at least one different phase. The XRD data in Fig. 12 show evidence for localized transformation when using P_{avg} of 5.6 W and 7.6 W. In addition to the two XRD peaks at $2\theta = 43.6$ and 51.0^{o} which index as the (111) and (200) reflections of austenite, an additional peak at ~44.6^{o} appears in Fig. 12(a) beginning at a scan speed of 150 mm/s. Knowing that this reflection does not originate from the coating (confirmed by selected area transmission electron diffraction), this single reflection is attributed to a different phase within the near-surface volume. The detection of austenite and a second substrate phase in a single sample is consistent with the shallow melt depths shown and the attenuation lengths of CuKα X-rays used for characterization. For our range of 2θ analysis, X-rays can penetrate several microns which is greater than the melt depths of many samples. Calculations using the Beer-Lambert Law[23] indicate that 99% of the incident X-rays will be attenuated within a 6 μm depth and more than 50% of the beam interacts with the top 1 μm. Additionally, calculations show that the thickest $MnCr_2O_4$ or Fe_3O_4 coating (~500 nm) attenuates only ~16% of the X-ray beam. Thus, for many samples, XRD should probe the coatings, the resolidified melt zone, and volumes of substrates that lie below the melt zone.

Selected-area, electron diffraction confirmed that austenite is locally transformed to either ferrite (α-Fe) or martensite. Electron diffraction patterns showed multiple reflections originating from the heat affected zone of a substrate, and these index to the body-centered cubic (bcc) structure of α-Fe. Note: it is difficult to distinguish between ferrite and martensite in the resolidified volumes, because the low carbon content of SS 304L results in a low degree of tetragonal distortion for martensite, making it similar to bcc ferrite. EDS analysis of these sub-surface regions shows a nominal composition of 83% Fe, 17%Ni and almost no Cr aside from the scattered, sub-micron Cr-rich polyhedral inclusions shown by TEM.

4.3.2.4 Microscale Color Islands

Experiments have demonstrated the formation of microscale color centers contained with larger areas of metal oxide treated with uniform fluence. Two examples of isolated color centers are shown by optical microscopy in Figure 19. The two areas shown were treated with different accumulated fluences (both involved 5.6W, 225 kHz, 120 ns pulse duration but utilized different scan speeds), and two different average colors are evident. Within each area, small, isolated, round features are discovered. Close examination of these images shows that the colors of these micro-features are different than the surrounding matrix of oxide. In many cases, the color of a particular micro-feature is different than its neighboring micro-color centers. In terms of information that could be documented and archived for comparison at a future date, one recognizes the differences in location of these microscale features, their different sizes and unique colors.

The origin of the micro-scale color centers is under investigation. Cross section electron microscopy has revealed a common trait of these features. As shown in Figure 20, micro-color centers are raised. FIB sections demonstrate that the raised morphology is due to preferential oxidation under a metal grain initially contained in the substrate. Oxidation occurs at the periphery of a grain and proceeds under this object. If a sufficient fluence is provided, the grain will become captured within the oxide layer. On top of the metal grain is a thin layer of oxide. The reduced thickness on top of this asperity compared with surrounding oxide material is evident in Figure 20. The particular color island shown in Figure 20 is almost completely separated from the substrate. In this micrograph, the oxide appears as a dark layer. Electron and x-ray diffraction studies showed that this layer was manganochromite ($MnCr_2O_4$) or Fe_3O_4.

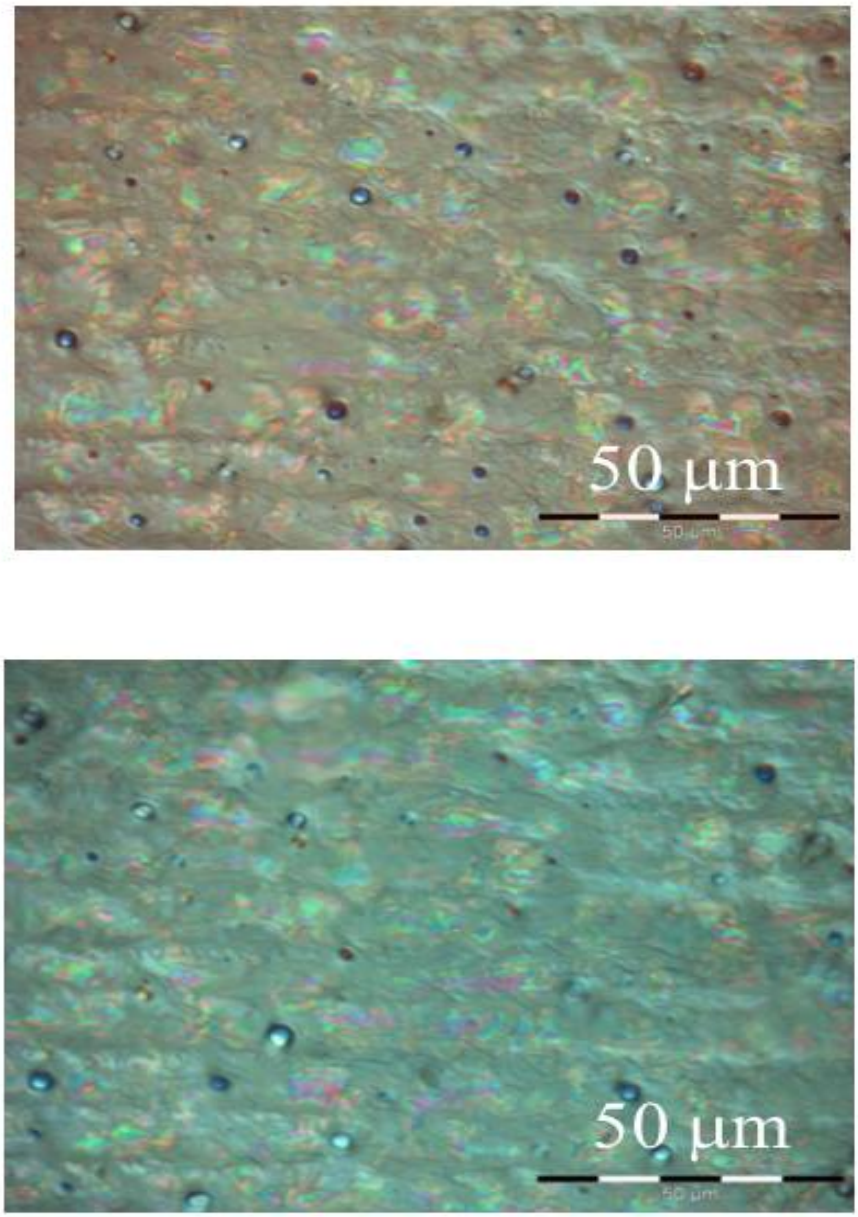

Figure 19. Plan view optical microscope images showing the color islands inside macro-scale color pixels. Each rectangular area was treated with a uniform laser fluence. Color islands generally round and randomly located.

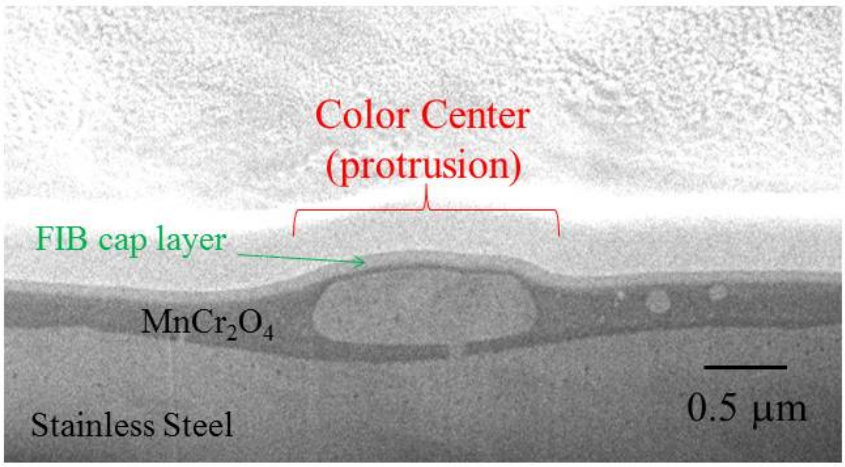

Figure 20. Cross section scanning electron micrograph of a micro-color center formed on stainless steel 304L. The oxide (labeled $MnCr_2O_4$) appears dark in this image. The color island protrudes from the surrounding material and includes a near-isolated metal grain. The oxide layer thickness on the island is reduced.

4.3.3. Color Markings on Titanium

This section describes the variety of color markings that are produced on commercially pure titanium during IR laser irradiation. Discussion begins with a description of microstructure and composition of oxide layers produced by laser-stimulated oxidation. Color is varied by control of the laser process parameters. Afterwards, the discussion turns to a detailed description of the optical properties of produced oxide layers. The color of oxide layers is affected by oxide layer thickness, oxide phase, its defect structure and the spectral reflectance of underlying volumes.

An example color QR code produced on Ti is shown in Figure 21. This pattern was created using an average power of 6.6 W, a repetition rate of 225 kHz, pulse duration = 119 ns and λ = 1064 nm. Colors were controlled by commanding laser scan speed as follows: blue (130 mm/s), red (180 mm/s), and yellow (240 mm/s). The sample is approx. 2.5 x 2.5 cm square.

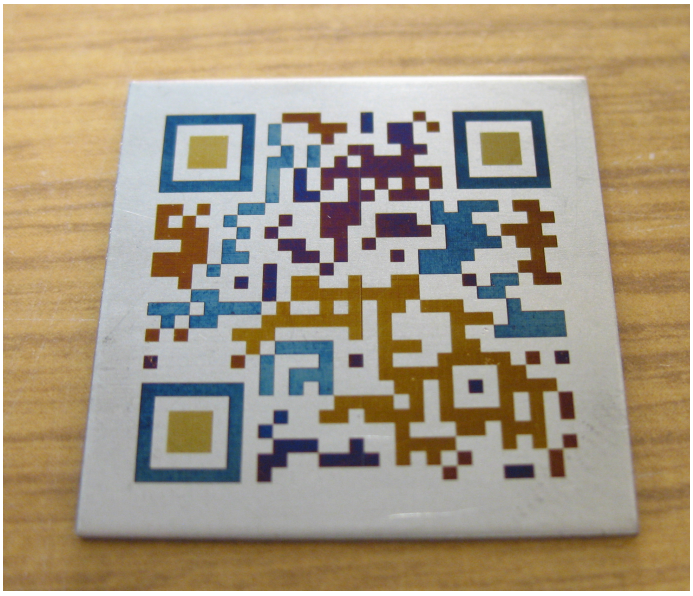

Figure 21. Multicolor, two dimensional bar code (QR type) created on Ti by scanned laser stimulated oxidation.

4.3.3.1 Microstructure and Composition of Laser-Grown Oxide Layers on Ti

Experiments systematically varied the laser fluence over a large range in order to determine the variety of colors that can be produced on the surface of commercially pure, grade 2 (ASTM B265) titanium. Figure 22 displays the different fluences used for laser-stimulated oxide growth on this substrate. As described earlier, 'fluence' represents the amount of energy accumulated in a particular feature area. The accumulated fluence is described by Equation 1. Fluences are included in Fig. 22 for the three average powers used for oxide growth, and F_{acc} spans a large range from ~85 to 4500 J/cm^2. Note: error bars that represent variations in accumulated fluence are smaller than the symbols used in this plot. A small fluence variation, < 2%, is estimated for directions perpendicular to beam travel, when accounting for the beam shape and the relatively small hatch.

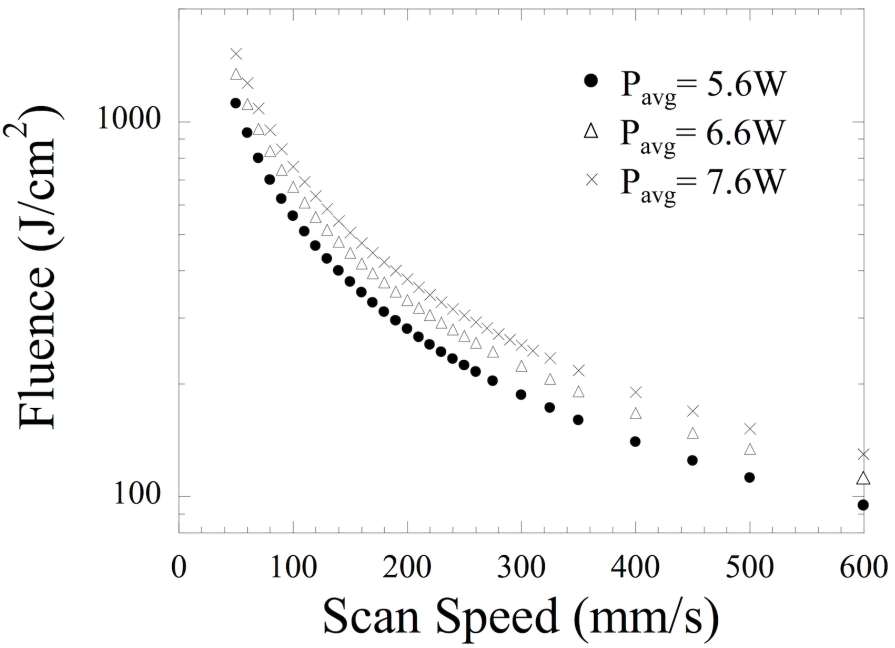

Figure 22. Plot of accumulated fluences used for laser-stimulated oxidation of titanium substrates.

Figure 23 includes a cross-section, transmission electron micrograph of a laser-grown oxide coating along with accompanying EDX compositional maps of oxygen and nitrogen. This particular coating was fabricated by one set of pulsed laser parameters (P_{avg} = 5.6 W, scan speed = 90 mm/s, F_{acc} = 622 J/cm^2) but is included because it shows many of the characteristics of produced oxide layers.

Coatings are comprised of up to three distinct layers. The thin, top layer of the shown oxide is 30 $\pm$ 8 nm thick and is composed of Ti and O. Labeled as TiO_2, it appears as a dark volume in the displayed high angle annular dark field image. Below the top layer of oxide lies a thicker

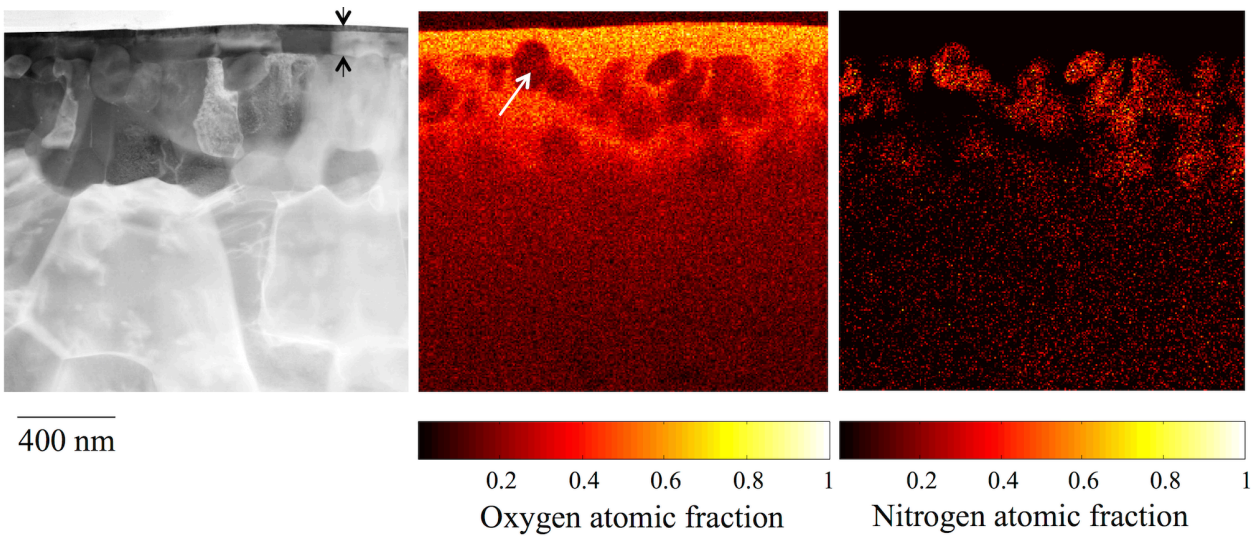

Figure 23. High angle annular dark field transmission electron micrograph and accompanying EDX compositional maps of an oxide coating fabricated using P_{avg} = 5.6W and a scan speed of 90 mm/s. A portion of the underlying substrate is included. The middle image shows a map of the O concentration. The N concentration map of the same area is shown on the right.

thicker, continuous titanium oxide layer labeled TiO. This middle oxide layer is measured to be 73 $\pm$ 8 nm thick, has a uniform O concentration, and contains minimal amounts of N. Below the two continuous titanium oxide layers is an inhomogeneous mixture of Ti, O, and N. In this volume, there are grains composed of Ti with varying amounts of N and O. For example, one grain composed mostly of Ti and N (marked with a white arrow) has penetrated through half of the overlying TiO layer shown. Unlike the top two layers, the bottom interface of this third layer is poorly defined with trace O extending at least 2 μm into the Ti substrate.

Electron diffraction shows that capping layers are composed of TiO_2 rutile. The measured lattice spacings derived from diffraction analysis of multiple capping layers are included in Table 4 along with the lattice spacings of candidate phases such as cubic TiO, monoclinic TiO, Ti_2O_3, TiO_2 rutile, and TiO_2 anatase [25-29]. Excellent matching to TiO_2 rutile is found for the ten evaluated reflections. Systematic dark field images, such as the one included in Fig. 24, show that TiO_2 cap

layers are continuous although the thickness of this layer varies. The coating displayed in this figure was made with the same laser process parameters as the coating shown in Fig. 22 (P_{avg} = 5.6 W, 90 mm/s). Annular dark field and high-resolution lattice images reveal additional details about TiO_2 capping layers. Figure 25(a) shows evidence for planar defects, which are most likely stacking faults. This particular coating was made using a P_{avg} = 7.6 W and a scan speed of 90 mm/s (F_{acc} = 844 J/cm^2). A high-resolution TEM image in Fig. 25(b) reveals a crystalline capping layer. The attached 2-dimensional Fourier transform was generated from a small area within the displayed field of view (identified with a dotted line, square box). The resultant pattern indexes to the [1-20] zone axis for TiO_2 rutile.

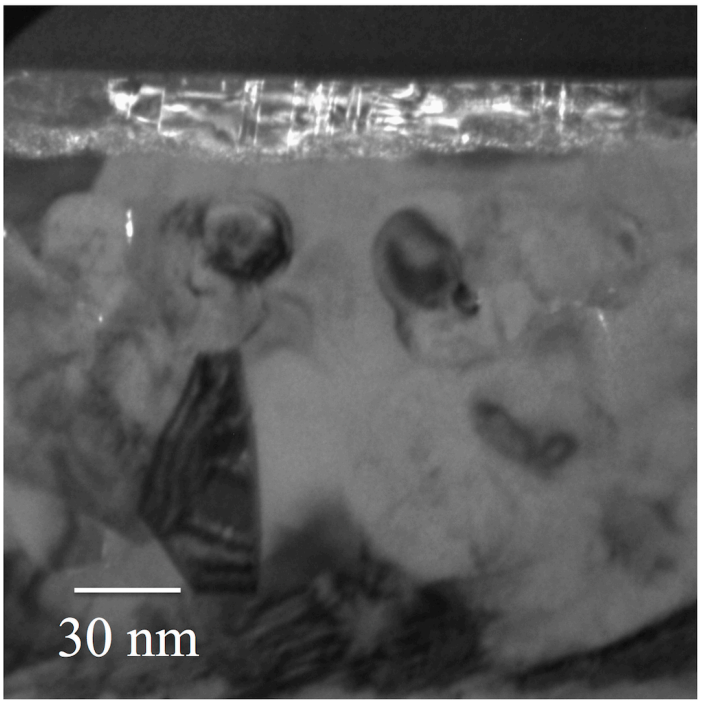

Figure 24. Systematic dark field image showing a continuous TiO_2 capping layer. middle image shows a map of the O concentration. The N concentration map of the same area is shown on the right.

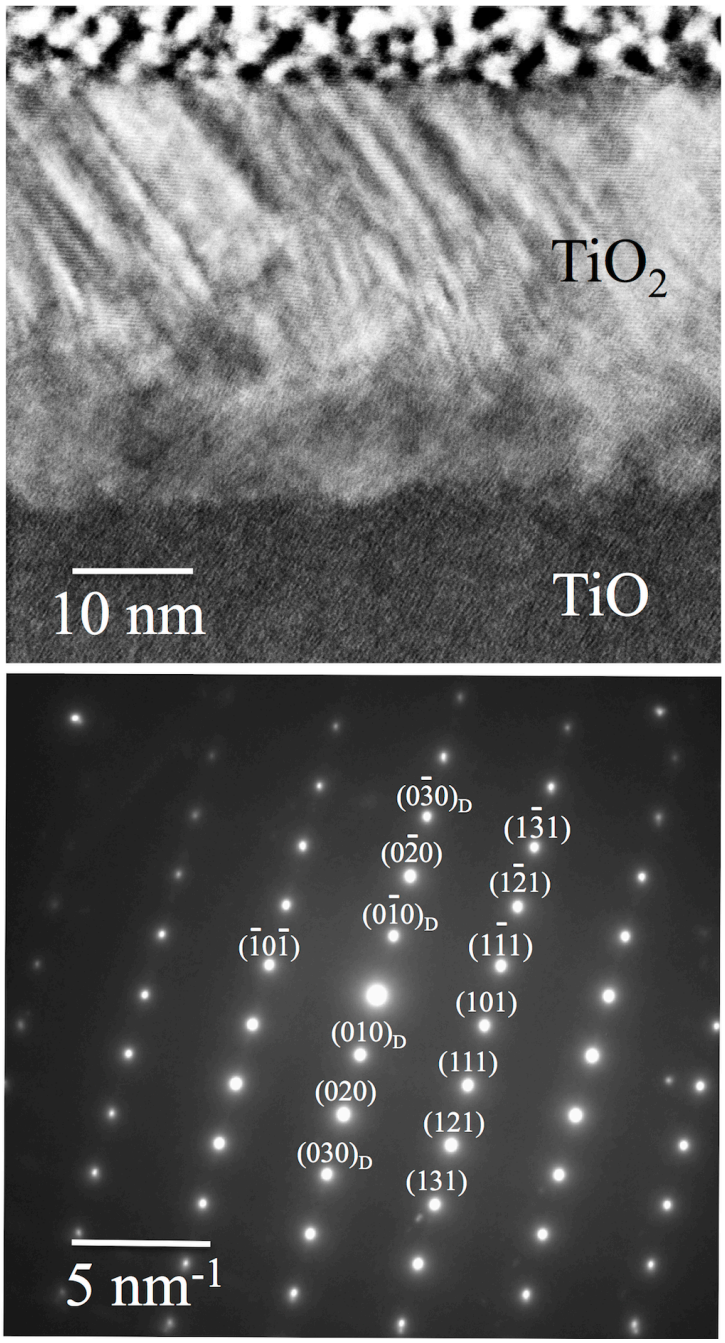

Figure 25. Annular dark field TEM image in (a) shows a TiO_2 rutile capping layer and underlying volume. High-resolution image in (b) shows a portion of the TiO_2 layer. (b) is a 2d Fourier transform generated from the 12 x 12 nm area marked with dotted outline.

Table 4. A list of measured lattice spacings obtained through diffraction analysis of titanium oxide capping layers. Also listed are the calculated lattice spacings for different, candidate phases. Italicized values correspond to the most intense reflections for a randomized polycrystalline sample. The analyzed specimen was made using an average laser power equal to 7.6 W and a laser scan speed of 90 mm/s.

Measured spacings (Å), cap layer	Calculated spacings (Å), cubic TiO (ref. 26)	Calculated spacings (Å), monocl. TiO (ref. 27)	Calculated spacings (Å), Ti_2O_3 (ref. 28)	Calculated spacings (Å), TiO_2 rutile (ref. 29)	Calculated spacings (Å), TiO_2 anatase (ref. 30)
3.19	2.427	5.587	3.761	*3.252*	*3.514*
2.50	*2.102*	4.452	*2.749*	2.491	2.430
2.28	1.486	4.144	2.578	2.300	2.378
2.19	1.268	3.754	2.326	2.190	2.331
2.03	1.214	3.318	2.255	2.057	1.891
1.61	1.051	3.061	2.126	1.689	1.699
1.59	0.965	2.948	1.881	1.626	1.665
1.45	0.940	2.793	1.727	1.481	1.492
1.45	0.858	2.772	1.675	1.454	1.480
1.42	0.809	2.443	1.640	1.426	1.364
		2.412	1.625	1.362	1.337
		2.392	1.519	1.348	1.279
		2.323	1.488	1.306	1.264

Electron diffraction analysis of the middle titanium oxide layer (i.e., the one lying below the TiO_2 cap layer) shows that cubic TiO has formed. Electron diffraction reveals that the crystalline phase formed in this volume is cubic and has a NaCl-type structure with a unit cell length of approximately 4.20 Å. Knowing that TiO and TiN both have a cubic structure and similar lattice parameters (a = 4.18 Å for TiO [26] and a = 4.24 Å for TiN [30]), it is difficult to determine which phase(s) have formed. However, this information combined with the compositional maps provided by EDX in Fig. 23 show that the middle layers are TiO. Only trace amounts of N are present in this middle layer. The formation of TiO is not surprising. Pérez del Pino reported the formation of this phase when using high laser power irradiation [31,32]. In other experiments, cubic TiO has

been made previously by quenching annealed titanium samples from above 952°C [33]. TiO is reported to be stable indefinitely at room temperature [33].

Investigating the phase of the bottom layer by selected area diffraction analysis and complimentary EDX compositional maps, one finds evidence for TiO_xN_{1-x}. Figure 23 shows that there are N-rich grains as well as O-rich grains. A similar structure is found in other samples made with different accumulated laser fluence. Due to the similar lattice parameters of TiO and TiN (and TiO_xN_{1-x}), the phase of individual grains was not examined further. These regions are not considered to be relevant to the optical appearance of coatings, because they reside below TiO, which is reported to be a metallic, reflective monoxide [34]. An oxygen composition gradient into the Ti is generally observed within the bottom layer of this and other samples. For the specimen included in Fig. 23, EDX maps show that oxygen and nitrogen have diffused into Ti to depths > 0.5 μm. The crystal structure below coatings (i.e., several microns below the surface) is hexagonal - consistent with Ti and several oxygen-intercalated phases such as Ti_6O. Oxygen-intercalated Ti phases have similar diffraction patterns as Ti, although the corresponding d-spacings are shifted slightly to larger values [35].

X-ray microbeam diffraction was used to investigate whether the phases composed within coatings change with increasing laser fluence. In Fig. 26, XRD patterns obtained from four coatings are displayed along with the pattern obtained from a bare Ti substrate. These particular coatings were made with different fluences using a fixed P_{avg} = 5.6 W.

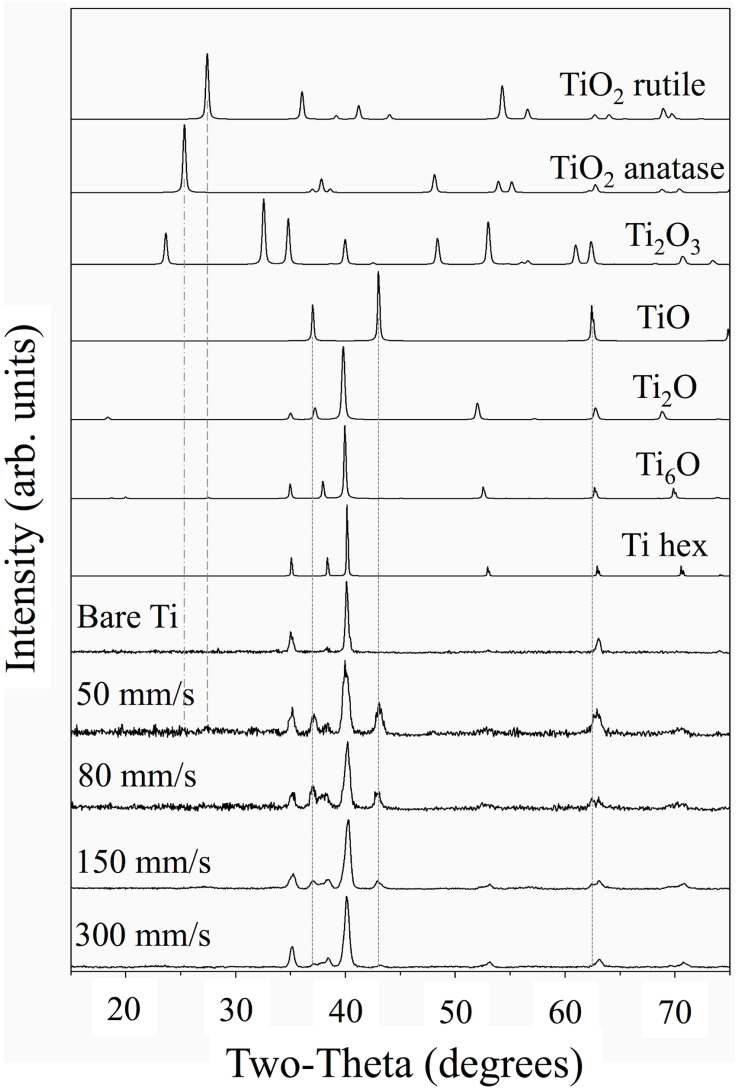

Figure 26. XRD patterns obtained from four oxide features grown on Ti using P_{avg} = 5.6 W and different scan speeds (noted above each pattern). A pattern obtained from bare Ti is also included. Archived diffraction patterns from candidate phases are included.

Comparing the different XRD patterns with the simulated diffraction patterns of candidate phases, one finds evidence for reaction of Ti with species contained initially in air. The diffraction peak at ~43 degrees two-theta is consistent with cubic TiO (as indicated with a dotted line in the plot) but could originate from TiO_xN_{1-x} or TiN. In addition, two other diffraction peaks at ~37 and 62.5 degrees two-theta are consistent with these three phases. However, these latter two peaks also

overlap with other candidate phases, including TiO_2 anatase and Ti_2O_3, and do not uniquely identify a single phase. It is expected that these three peaks originate from coatings grown on the surface of Ti. The intensity of these reflections increases with F_{acc} (i.e., decreased laser scan speed), yet the intensity of the Ti peaks remains unchanged or decreases slightly. Furthermore, XRD shows limited evidence for crystalline TiO_2 in these coatings made with low average power laser irradiation. It is likely that XRD does not detect the thin capping layer of TiO_2 in these samples, because of the small source size utilized for microbeam diffraction experiments. Also, the source and detector were not arranged in a grazing incidence geometry, which is preferred for obtaining diffraction data from thin surface layers. It is emphasized that XRD did not show evidence for Ti_2N [36].

XRD shows that the same phases form when using higher P_{avg} and reveals increased amounts of TiO_2. Figure 27 shows the XRD patterns obtained from several coatings made with P_{avg} = 7.6 W. The peaks at ~37, ~43 and 62.5 degrees attributed to TiO_xN_{1-x} are again observed, and these increase in intensity with added laser fluence. Comparing the data in Figs. 26 and 27, the intensity of these three peaks is greater for coatings made with 7.6 W, as expected when using a larger laser fluence. Also, coatings made with a scan speed of 50 and 80 mm/s show evidence of crystalline TiO_2. The low intensity diffraction peak at ~27.5 degrees is attributed to TiO_2 rutile, consistent with electron diffraction analysis. An additional, weak reflection is observed at ~25.2 degrees, which matches a known reflection of TiO_2 anatase. XRD shows evidence for oxygen- intercalated phases in samples made with 5.6 and 7.6 W. Evidence for these phases is recognized by the continued shift to smaller two theta with increasing F_{acc} (i.e., decreasing laser scan speed) for several reflections of hexagonal Ti. The patterns for two candidate oxygen-intercalated phases

(Ti_6O and Ti_2O) are included in Figs. 26 and 27 for comparison. It is possible that these phases are contained in the inhomogeneous bottom layer of coatings.

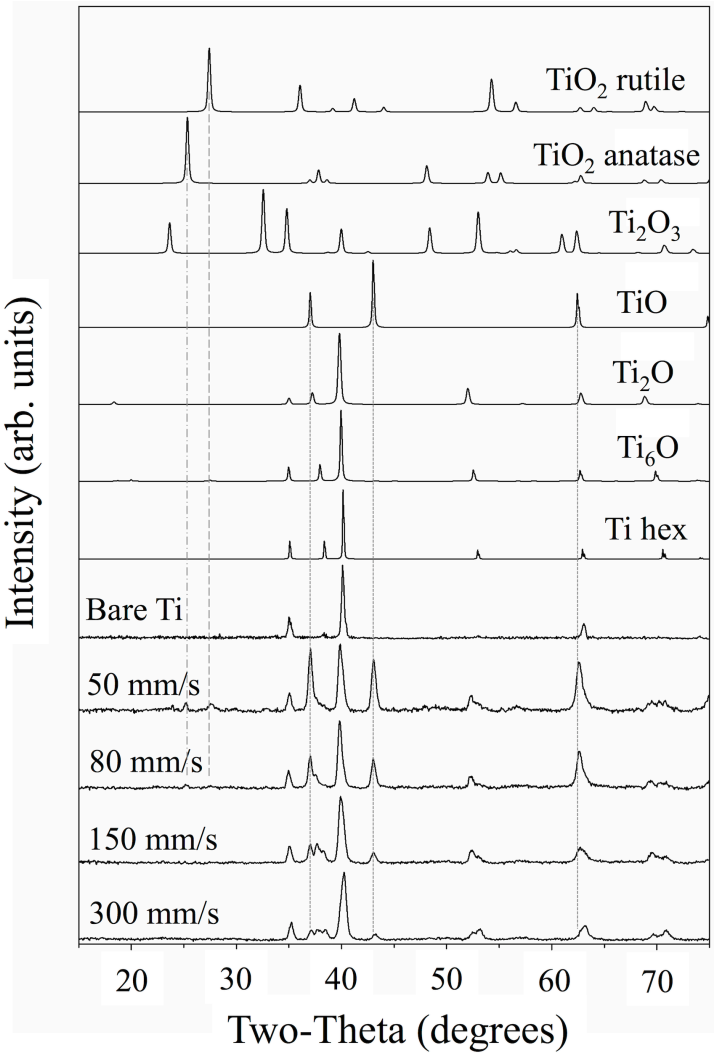

Figure 27. XRD patterns obtained from four oxide features grown on Ti using P_{avg} = 7.6 W and different scan speeds (noted above each pattern). A pattern obtained from bare Ti is also included. Archived diffraction patterns from candidate phases are included.

Having distinguished the presence and location of oxide layers via diffraction analysis, TEM images were used to examine the thickness of coatings. Specifically, the average thicknesses of several titanium oxide coatings along with standard deviations have been determined from dark field TEM images. The results shown in Fig. 28 for two different laser powers demonstrate that

continuous titanium oxide coatings vary from 10 nm at low fluences to 120 nm at high fluences. A reported oxide thickness is the combined thickness of the middle TiO layer and TiO_2 cap. The thickness of TiO_xN_{1-x} was not measured due to the poorly defined bottom interface of this layer.

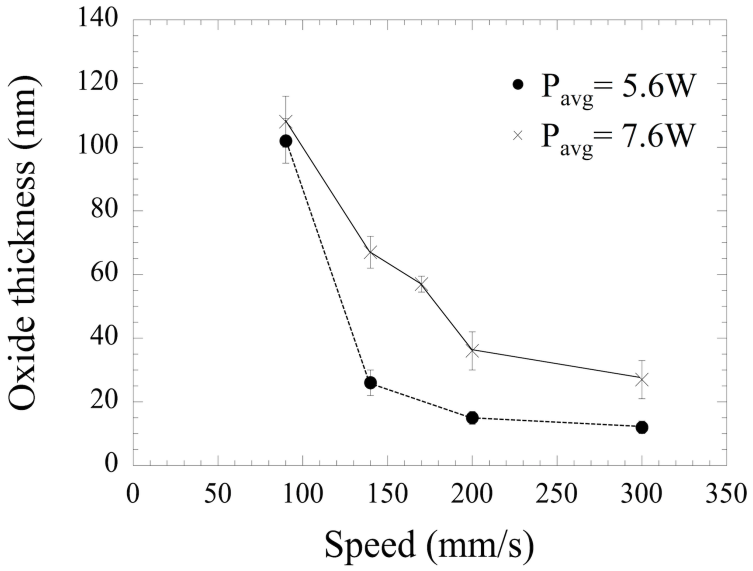

Figure 28. Plot of average oxide thicknesses measured by TEM. Oxide thicknesses are the combined thickness of TiO_2 capping layers and underlying TiO. Results are plotted versus laser scan speed for different average powers.

As expected, the oxide thickness tends to increase with accumulated laser fluence. Also, the oxide layer thickness is generally increased when using a larger P_{avg} with scan speed held constant. One exception is noteworthy. The sample made using 7.6 W and 90 mm/s scan speed has an oxide thickness that is comparable (within experimental uncertainty) to that made at 5.6 W. This is likely due to the onset of ablation for the 7.6 W experiment. Measurements of oxide layer surface height with respect to the height of surrounding, untreated areas of Ti substrates confirm that the 7.6 W, 90 mm/s coating is recessed whereas the other coatings described in Fig. 28 are not.

4.3.2.2 Optical Properties of Oxide Layers Fabricated on Ti

Oxide layers formed on a Ti surface exhibit a variety of different colors, shown in Fig. 29. These particular samples were irradiated with P_{avg} = 6.6 W, and the laser scan speed (marked on the specimen beside a given feature) was adjusted to attain a given fluence and color. Colors include different shades of gold, orange, red, purple, and blue with this particular sequence of colors formed with increasing fluence. The colors shown in Fig. 29, and the order in which they form, are similar to those created using P_{avg} = 5.6 and 7.6 W.

The spectral reflectance of all color features produced on Ti have been measured. A portion of the data obtained from coatings made using P_{avg} = 5.6 W is included in Fig. 30. In Fig. 30(a), the reflectance of three thin colored oxides is shown along with the spectra obtained from bare Ti. Compared with bare Ti, oxide coatings exhibit a decreased reflectance for all specified wavelengths. It is also apparent with these coatings that the reflectance generally decreases with increasing oxide thickness. To recall, the thin oxide layers made with 200 and 300 mm/s have thicknesses of 15 and 12.5 nm, respectively. The oxide made at 600 mm/s should be even thinner. The thinnest oxide coatings displayed in Fig. 30(a) exhibit a gold appearance, consistent with cubic TiO [36,37].

The optical appearance of thicker coatings is attributed to effects of interference wherein incident light reflected from the upper and lower boundaries of a transparent capping layer interfere, leading to color formation. Thicker oxide coatings exhibit a varying spectral reflectance characterized by broad maxima and minima. As shown in Fig. 30, the reflectance minima shifts to larger wavelengths as coatings are made thicker consistent with interference effects [38]. Further, the thicker coatings described by plot 30(b) exhibit several maxima and minima, consistent with

higher order interference effects [38]. With cubic TiO being a reflective metal, interference with the TiO_2 capping layers revealed by TEM are likely responsible for interference in the visible part of the spectrum. Previous reports show that TiO_2 films exhibit a variety of colors that are attributed to interference [39]. In fact, a similar sequence of colors is observed with vapor-deposited TiO_2 films when their thickness is increased within the range reported here.

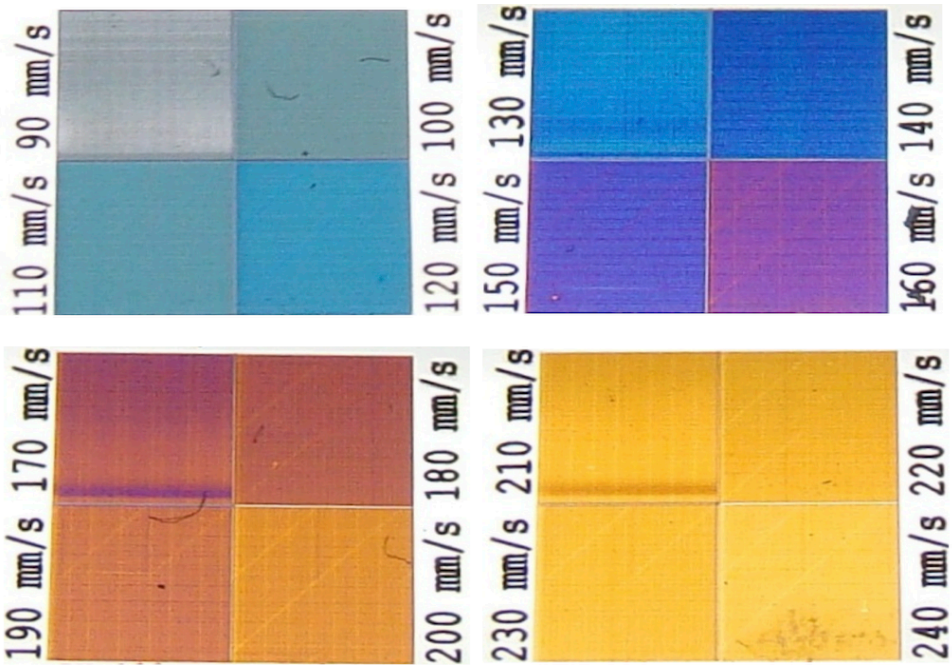

Figure 29. Photographs of sixteen different colored oxide layers on Ti. All were made using P_{avg} = 6.6 W with the labeled scan speeds.

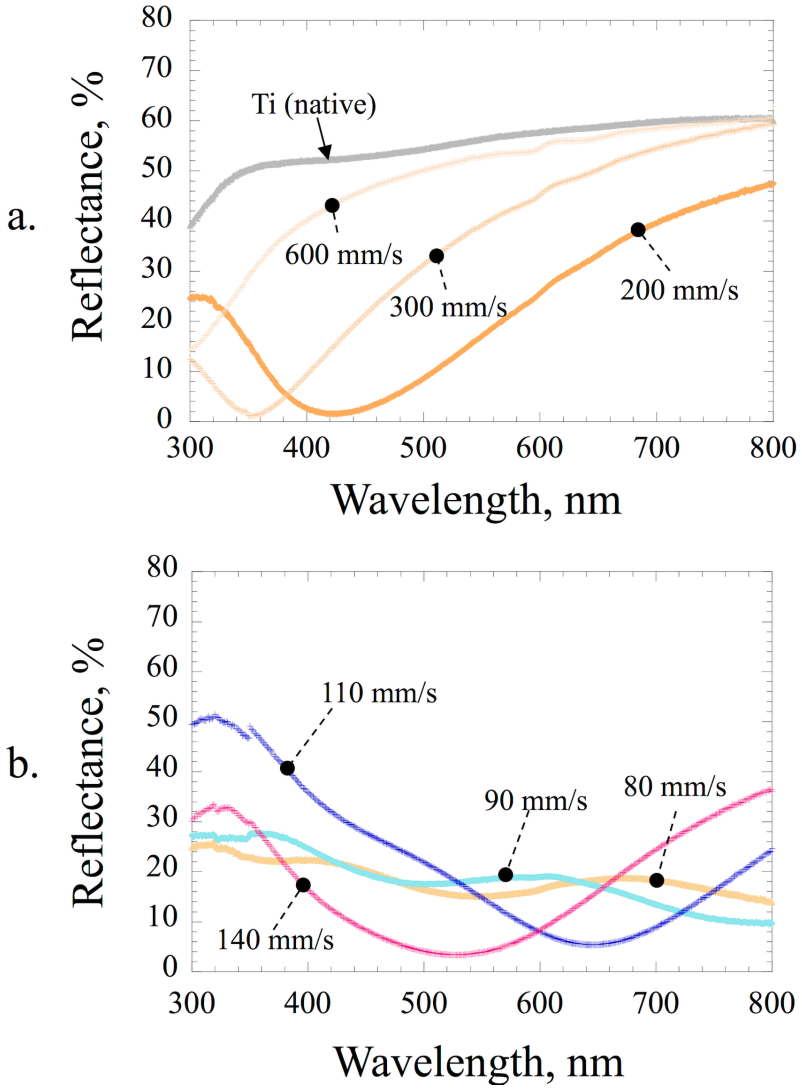

Figure 30. Plot (a) includes reflectance spectra from bare titanium and three thin metal oxide coatings made using P_{avg} = 5.6 W and scan speeds of 600, 300 and 200 mm/s. Plot (b) shows the reflectance spectra of four oxide coatings made using the same average power and scan speeds of 140,110, 90 and 80 mm/s.

The chromaticity of coatings has been derived from measured reflectance spectra and compared with previous reports of TiO_2 optical properties. Shown in Fig. 31 on the CIE 1931 color map, the measured chromaticity of laser-fabricated coatings spans a large range of x, y values. Colors are vibrant but not saturated which would otherwise correspond to chromaticity at the boundary of the diagram [40]. The colors evolve with increasing fluence in the order cited

earlier (golden, orange, red, purple, blue) tracing a clockwise rotation around the depicted ellipse. In general, we find that the sequence of x, y chromaticity are similar whether using P_{avg} = 5.6, 6.6 or 7.6 W. It is interesting that as colors evolve with increased fluence, the chromaticity tracks back to values that are similar to bare Ti (having x = 0.323, y = 0.338) and some of the thinnest oxide layers. This behavior has been observed with vapor-deposited TiO_2 thin films. TiO_2 films deposited on Si exhibited several repeat cycles with increased film thickness [41].

The color formed during laser irradiation is tailored by the accumulated fluence. In Fig. 31, three data points are circled to demonstrate this effect. The three samples represented by these symbols were made with different powers, but used the same F_{acc} (~350 J/cm^2). This was accomplished by selecting the requisite laser scan speeds as described earlier. The chromaticities are similar for these three samples, which demonstrates the important effect of energy input (in J/cm^2) when establishing a given color. Note: oxide coatings made with different powers and identical scan speeds are characterized by different fluences and dissimilar resulting colors. For example, with the scan speed set to 150 mm/s, the x-y chromaticity of samples made with 5.6, 6.6 and 7.6 W were 0.433, 0.318; 0.227, 0.181; and 0.216, 0.247, respectively.

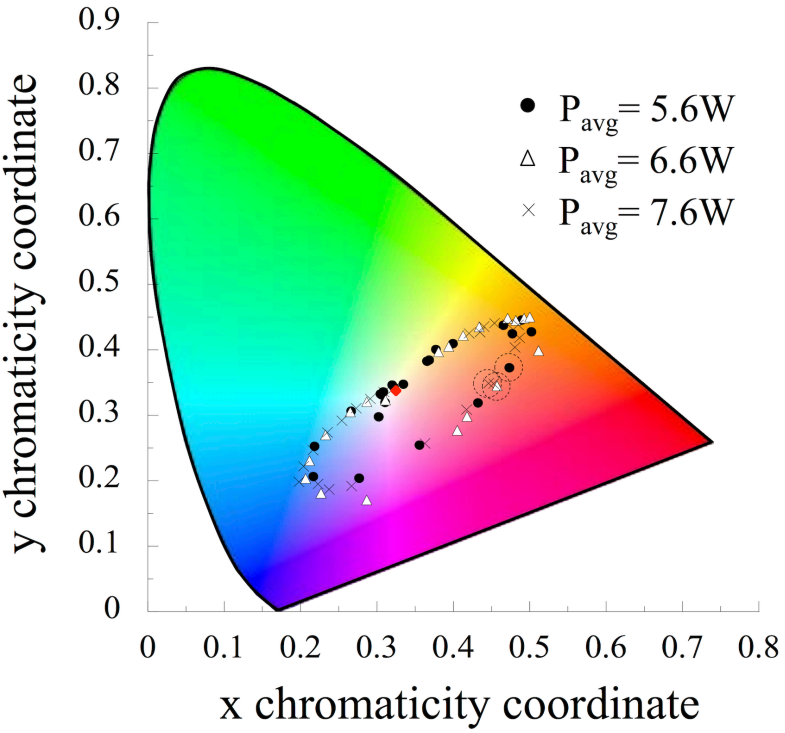

Figure 31. Chromaticity of various titanium oxide coatings made using 5.6, 6.6 and 7.6 W power plotted over the CIE 1931 color space. Dotted circles highlight the chromaticity of three features made using different P_{avg} but speeds that affix F_{acc} = ~350 J/cm^2. The chromaticity of a bare Ti sample is indicated with a red diamond symbol.

4.3.2.3 Microstructure of Underlying Ti

Scanning electron microscopy provides a larger area view of the complex structure that is formed below oxide layers as a result of laser heating. Consistent with the report by Pérez del Pino [31,32], our samples exhibit a grain structure that varies through the thickness of a specimen with fine grains found just below the oxide coating and larger grains beneath these. Below this refined grain structure, SEM reveals a relatively large volume of modified Ti. Cross-section SEM images of two samples treated with 7.6 W, 200 mm/s are displayed in Fig. 32. In (a) one sees the effects of laser irradiation after a single linescan and in (b) the structure resulting from multiple linescans is revealed. The modified structure is identified as α' martensite based on comparisons to

published Ti microstructures [35]. Grade 2 Titanium is known to undergo a transformation from an hexagonal close packed α phase to a body centered cubic β phase at 915^{o}C [35]. Upon cooling through the β transus temperature, Ti is reported to form athermal martensite. The most prevalent form of martensite for commercially pure Ti is hexagonal α' having a massive or lath martensite structure [35], and these martensite structures have a similar appearance to that shown in Fig. 32. Thus, it is suggested that the depth of transformation correlates with the extent of heating to the aforementioned β transus temperature. The measured depths of α' martensite resulting from pulsed laser irradiation are included in a plot (Fig. 33). Results are shown for two different powers where transformed depth generally increases with accumulated laser fluence. Transformed depths are as large as ~25 μm. SEM analysis has also revealed that cracks form in several oxidized samples. Channel cracks form to depths greater than the combined thickness of the TiO_2 and TiO layers, typically penetrating into regions of hexagonal Ti containing detectable amounts of O. This may be relevant to investigators that implement fracture as a method to section samples for thickness measurement and structural characterization.

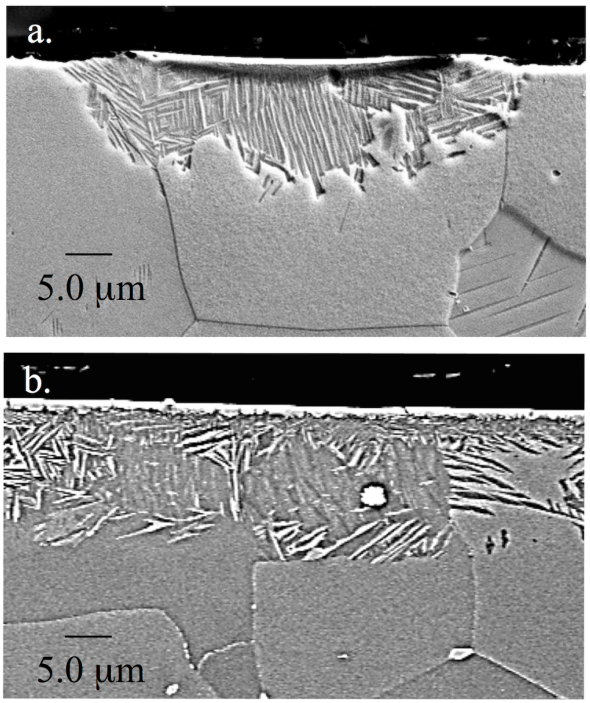

Figure 32. Cross-sectional scanning electron micrographs of an oxide coating and underlying substrate after laser irradiation of (a) a single line and (b) multiple, neighboring lines. Irradiation involved P_{avg} = 7.6 W and a scan speed = 200 mm/s. The sections were made transverse to the direction of laser travel.

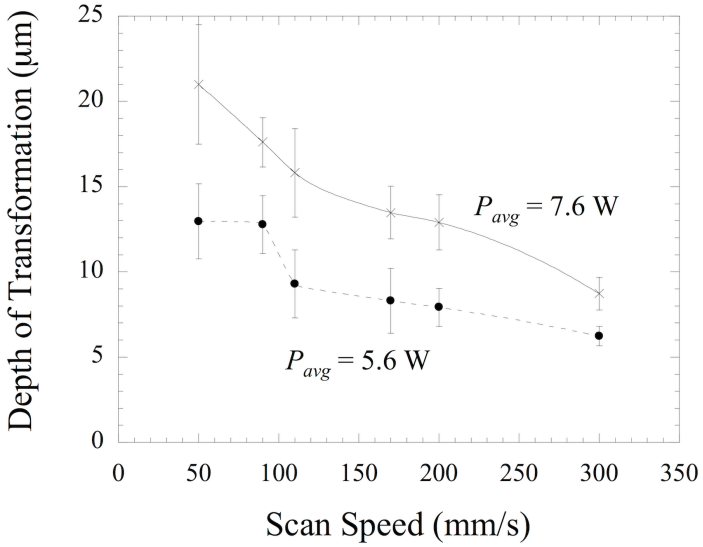

Figure 33. Plot of transformation depth versus laser scan speed. Transformation depth is defined as the depth at which alpha prime martensite formed via laser heating and cooling. Results are shown for P_{avg} = 5.6 and 7.6 W. Lines are guides to the eye.

4.4. Laser Coloring Thin Film Coatings

Thin films were also irradiated with nanosecond pulsed laser light to produce color markings. Approximately 1 μm thick metal coatings grown by vapor deposition were irradiated to generate a variety of colors. Metals were chosen based on their propensity to oxidize according to published thermodynamic properties.

Color markings were made without delaminating metal films from substrates or damaging films other ways. Metal films remained adhered as the near-surface region of the metal was oxidized. The thicknesses, phase, and microstructure of produced oxide layers have been characterized and correlated with the observed colors. Detailed ellipsometric studies of these oxide layers are described in Section 4.5. The same general experimental setup

Example color markings produced on a sputter-deposited Ti thin film are shown in Figure 34.

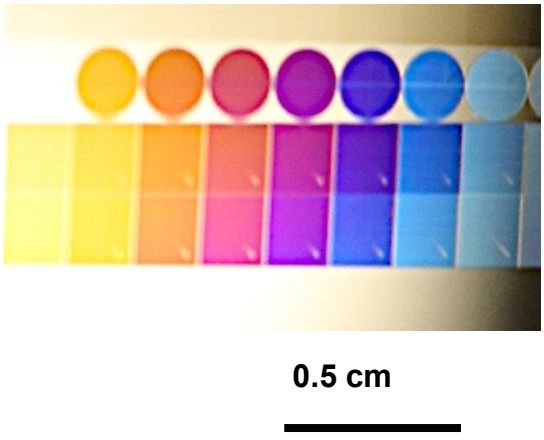

Figure 34. Variety of colors formed by laser stimulated oxide growth on Ti thin films.

4.4.1. Vapor deposition of metal thin films for laser color marking

Direct current magnetron sputter deposition was used to deposit various metal films for subsequent laser coloring/surface oxidation. Metal films were deposited using a Unifilm Co. system having a base pressure of 2 e-7 Torr. The vacuum system was cryopumped and samples were not intentionally heated during deposition. The substrate temperature rose to ~50C during film grown as a result of deposition. Table 5 summarizes the metal films and their thicknesses used for experiments. Film purity is generally in excess of 99.9% with some Ar incorporation into films. The Ar arises from its use as the sputter beam. A thin native oxide is present on the surface of metal films once these are removed from the vacuum vessel into air. Substrates were ~450 μm thick Si wafers.

Table 5. List of thin film materials colored using nanosecond pulsed lasers.

Film Material	Film Thickness, Reflectance	Measured Film Reflectance at 1064 nm
Titanium	2 μm	0.57
Chromium	1 μm	0.62
Vanadium	2 μm	0.54

4.4.2. Laser color marking of Ti metal films

Diced samples were then placed in the focus of an SPI, Inc. laser with a 1064 nm wavelength, 120 ns pulse length, focused $\frac{1}{e^2}$ diameter of ~ 80 μm, average power = 1.79 W, and a repetition rate = 400 kHz. The Gaussian, focused laser beam was rastered across the samples using galvanometric mirrors with a hatch spacing = 10 μm and a scan speed ranging from 140 to 10 mm/s. The accumulated fluence is calculated as $F_{acc} = \frac{P_{avg}N_p}{A*v}$ where P_{avg} is the average power, N_p is the total number of pulses over a given area A, and v is the repetition rate. The calculated accumulated fluences for given scan speeds are: 128 J/cm^2 (140 mm/s), 149 J/cm^2 (120 mm/s), 179 J/cm^2 (100 mm/s), 199 J/cm^2 (90 mm/s), 224 J/cm^2 (80 mm/s), 256 J/cm^2 (70 mm/s), 298 J/cm^2 (60 mm/s), 358 J/cm^2 (50 mm/s), 448 J/cm^2 (40 mm/s), 597 J/cm^2 (30 mm/s), 895 J/cm^2 (20 mm/s), and 1.79 kJ/cm^2 (10 mm/s). Ellipsometric measurements were obtained from a J.A. Woollam Co., Inc. rotating-analyzer spectroscopic ellipsometer at angles of 65°, 70°, and 75° for each sample over a wavelength range from 300.24 nm (4.13 eV) to 1653.3 nm (0.75 eV) at 0.02 eV step sizes. Modeling and mean squared error (MSE) analyses were performed using the standard J.A. Woollam WVASE32® software. Models were fit to the measured quantities Ψ and Δ, where $\frac{R_p}{R_s} = \tan\psi\, e^{i\Delta}$ and R_p and R_s are the complex Fresnel reflection coefficients for p- and s-polarized light respectively. Estimated oxide thicknesses have 90% confidence limits of ± 3 nm. The reflectance of coatings was evaluated using a Varian Inc. Cary 5000 UV-Visible-IR spectrophotometer and are presented5in Table 5. Reflected light was collected by an internal diffuse reflectance accessory (integrating sphere) such that the specular beam was included in detection. Grazing incidence XRD data were collected using a Siemens D500 diffractometer. XRD utilized CuKα radiation (λ = 0.15418 nm). Cross-section TEM samples were prepared using

an ex-situ, focused ion beam lift-out method. High-angle annular dark-field (HAADF) imaging, energy-dispersive x-ray spectroscopy (EDS), and electron energy loss spectroscopy (EELS) were performed using a FEI Co. Titan G2 80-200 probe aberration-corrected transmission electron microscope.

4.4.2.1 Phase, microstructure and reflectance of oxides produced on Ti films

Bright-field optical images of laser-irradiated Ti films are shown in Figure 35(a)-(d). For increasing accumulated fluence (decreasing scan speed), the color of the Ti-oxide system progresses from gold/yellow, orange, blue, and to a mixture of colors. While it is not obvious in the image in Figure 34(d), there is a mixture of colors visible by eye. The scan lines of the laser are also visible in all samples, and these cause slight variations in the color over each scan area. The combined specular and diffuse reflectance spectra obtained from these and other irradiated samples are shown in Figure 35 (e) and (f).

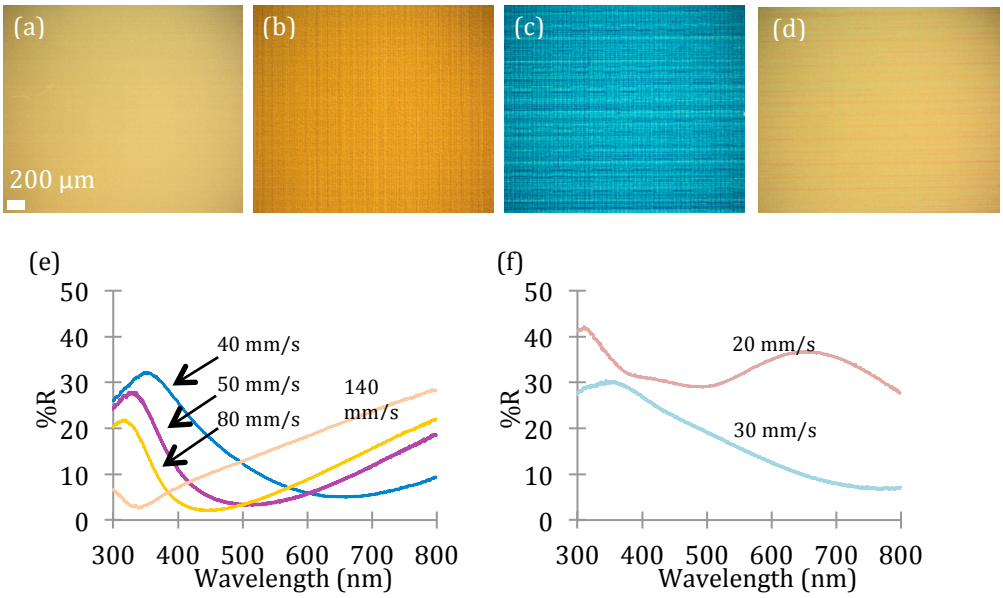

Figure 35. Bright field optical images of laser-irradiated areas of a 2 µm thick Ti film. The laser scan speeds were (a) 140, (b) 80, (c) 40 and (d) 20 mm/s. (e) Reflectance spectra of laser-irradiated areas for the same scan speeds. (f) Reflectance spectra of laser-irradiated areas when using 30 and 20 mm/s.

The tested ranges of accumulated fluences that produce a given color are as follows: 128 - 199 J/cm^2 (yellow), 224 - 358 J/cm^2 (orange), 448 – 597 J/cm^2 (blue), 895 J/cm^2 (mixture), and 1.79 kJ/cm^2 (mixture). In our previous publication describing laser-oxidation of bulk Ti[2], we found similar colors were produced with the following accumulated fluences: 279 – 319 J/cm^2 (yellow), 335 – 394 J/cm^2 (orange), 418 – 446 J/cm^2 (purple), 478 – 558 J/cm^2 (blue), 609 – 744 J/cm^2 (mixture). The peak laser intensity used in the current study was 7.4*10^5 W/cm^2. Throughout the remaining paragraphs of this section, scan speeds will be presented with their respective observed colors labeled in parentheses.

Grazing incidence XRD patterns obtained from samples made at 90 mm/s (yellow) and 10 mm/s (mixture) are shown in Figures 36(a) and 36(b) respectively.

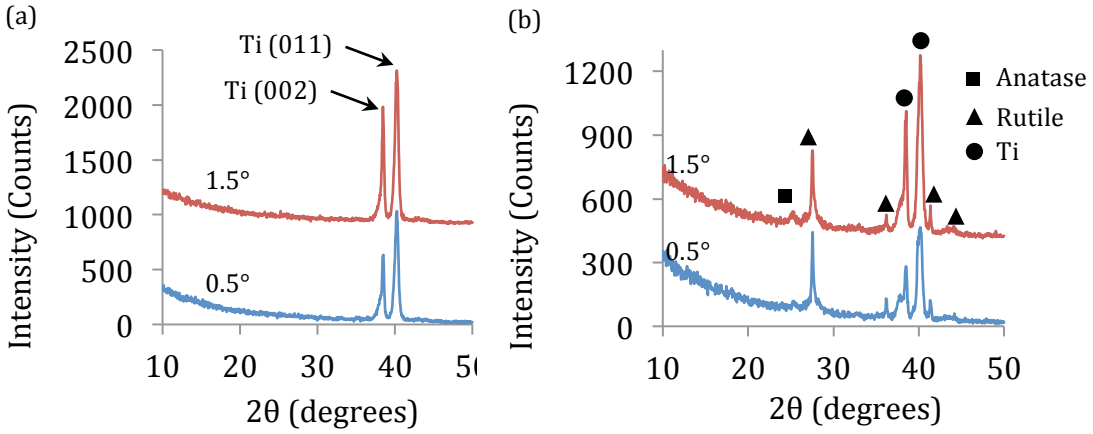

Figure 36. XRD patterns obtained at grazing incidence angles of 0.5 and 1.5 degrees for (a) a yellow oxide film made using v = 90 mm/s and a mixed color samples made using v = 10 mm/s.

For low and high fluence samples, the suppression of the Ti (100) peak shows a preferred out-of-plane [002] Ti film orientation (similar to Ti prior to irradiation). For samples made with low fluences, the oxide layer is too thin to be detected with our XRD approach. Grazing incidence

XRD spectra for the high fluence samples, such as the 10 mm/s (mixture) sample, suggest oxygen-intercalated phases of Ti_3O and Ti_6O are present, along with TiO_2. The dioxide layer is now thick enough to be detected and is mostly rutile TiO_2 with some anatase present.

The Ti_6O and Ti_3O phases present in the 10 mm/s sample both have a similar lattice structure to that of Ti metal, although strained. These structures are solid solutions of O incorporating into the hexagonal Ti lattice. A solid solution phase is evidenced in the diffraction pattern by a shoulder peaked at 37.8° for a 0.5° grazing incidence angle, present near the expected Ti metal peaks in Figure 36(b). The hexagonal unit cell is expanded and the diffraction peaks shift to lower 2θ values as more oxygen is incorporated into the lattice. It is difficult to assign these extra peaks to specific Ti_xO ($x \geq 2$) phases, as the phases appear to have relatively small crystallite sizes which, results in broadened peaks, ultimately driving the small peaks into the background level. Also, residual stress can shift peak positions into registry with the 2θ positions of other (unstrained) candidate phases. Therefore, the diffraction data associated with these volumes does not uniquely determine stoichiometry.

A HAADF TEM cross-section shows a discrete oxide layer at the top of a 2 μm-thick Ti film in Figure 37(a). This sample was made using a laser fluence of 895 J/cm^2. High-resolution TEM showed that all capping layers were polycrystalline. Electron diffraction patterns obtained with the transmission electron microscope were consistent with TiO_2 rutile. The corresponding EDS map for the HAADF image is shown in Figure 37(b). Red (top-half of the map) represents signal from both Ti and O, and green (bottom-half of the map) represents mostly signal from Ti. Near the Ti/TiO_2 interface there is a gradient in the composition, and this volume is likely a Ti/TiO_2 mixture. Since we do not know the exact composition of the bottom-half of the map, we refer to this intermixed region as a Ti_xO layer present underneath the TiO_2 layer. The volume

shown in the bottom half of Figure 37(a) exhibits an electron diffraction pattern that is consistent with Ti, and the inset shows a Fourier transform (FT) of a high-resolution image of the TiO_2 layer. The FT pattern is consistent with the rutile [1-10] zone axis.

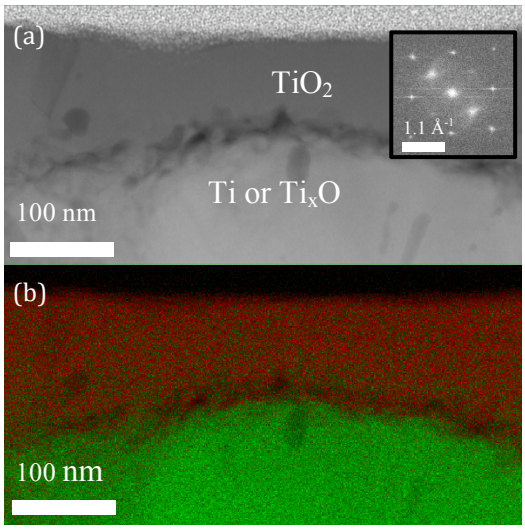

Figure 37. (a) HAADF TEM cross section image of an oxide layer made on Ti film using a v = 20 mm/s. The inset in (a) shows a Fourier transform of a high resolution TEM image of the TiO_2 capping layer. (b) is a corresponding EDS map of the same sample. Red represents signal obtained from both Ti and O and green represents Ti only.

The TiO_2 layer was also identified using EELS analysis, where an interface is visible between a mixed Ti/O capping region and the underlying Ti. The composition of the TiO_2 rutile was confirmed using EDS and no deviation of the Ti:O ratio was detected. The thickness of the TiO_2 capping layer increases with fluence, and variations in the thickness are a result of inhomogeneous laser irradiation and the initial roughness of the as-deposited Ti film.

4.4.2.2 Detailed optical properties revealed by ellipsometry

In order to find the n and k of the initial Ti films (i.e., prior to laser irradiation), ellipsometry was completed and point-by-point fits of Ψ and Δ, starting from the longest

wavelength, were performed using bulk Ti values as a starting point. A 2 nm-thick native TiO_2 oxide was assumed to be present on the surface [42,43]; the literature n and k values for the ordinary axis of the TiO_2 rutile phase [44] were used for this calculation. The literature values for bulk, polycrystalline Ti are plotted in Figure 4(a) along with the modeled n and k of 2 μm-thick sputter deposited Ti films (having a 2 nm oxide cap). The literature Ti n and k are plotted from the J.A. Woollam WVASE32® software and are similar to those found in the literature [45]. It can be seen from the figure that the n and k for the sputtered Ti film differ significantly from bulk Ti reported in the literature. This difference is expected based on prior works. Of note, the sputtered Ti film n and k are similar to the c-axis optical constants of electron-beam deposited Ti films [45].

Assumptions when modeling laser-fabricated oxides

Our first assumption that is included in models is that after laser irradiation, when ellipsometric measurements are conducted, we have air/TiO_2/Ti interfaces. This is consistent with observations made by electron microscopy that layers are well adhered with no delamination. We also allow for the optical properties of TiO_2 layers and underlying Ti film (base layer) to be modified from literature values. X-ray diffraction showed evidence for the formation of a rutile phase with some anatase. Attempts to use an effective medium approximation (EMA) to account for the secondary oxide phase (anatase) within the TiO_2 layer models did not improve the fits to Ψ and Δ, so throughout the paper the TiO_2 layer is assumed to consist of one oxide phase, i.e. rutile.

Surface and interfacial roughness can potentially affect ellipsometric results [46], but the roughness of our samples is not expected to impact our modeled results. To confirm this, a surface and/or interfacial roughness of 5 - 10 nm was assumed for each sample, rather than modeled due to

parameter correlations, in separate evaluations. It was found that roughness did not make significant improvements or changes to estimated quantities. For these reasons surface roughness was set to zero (ideally flat) for further modeling of ellipsometric data.

It was expected, based on the directional heating of the oxide growth method, that the optical constants (n,k) of a TiO_2 layer may not be uniform or isotropic throughout its thickness [47]. Attempts to include a gradient n in the model did not make significant improvements in the MSE of the fits to Ψ and Δ. Therefore, n was not graded in depth for the final analysis.

Lower Laser Fluence Results (< 448 J/cm^2)

We use a Cauchy model in transparent regions (λ > 400 nm) for estimating the thickness and n of TiO_2 for different samples. Specifically, the dispersion-limited Cauchy approximation, $n(\lambda) = A + \frac{B}{\lambda^2} + \frac{C}{\lambda^4}$ where A, B, and C are constants, is used for estimation. The n(λ) and thickness from the Cauchy fit were then used as initial values in a point-by-point fit (longest λ to shortest λ) to modify the TiO_2 layer in the absorbing regions, where a Cauchy layer approximation cannot be used. The thickness was fixed and the n and k values were allowed to float. To be clear, models of low fluence samples used the n and k of sputter-deposited Ti films determined by ellipsometry (presented in Figure 38(a)) for base layers.

In Figure 38(b), we show the experimental Ψ (dashed lines) and modeled Ψ (solid lines) in the transparent region for a 140 mm/s sample (the lines are overlapping in this example). Excellent matching is shown for each of the ellipsometer angles used for characterization. In this case, MSE = 2.7 and thickness = 8 nm. The resulting n(λ) derived from the Cauchy model and

k(λ) are plotted, along with literature rutile values [48], in Figure 38(c). These results show the n and k of our laser-grown TiO_2 are not the same as literature TiO_2.

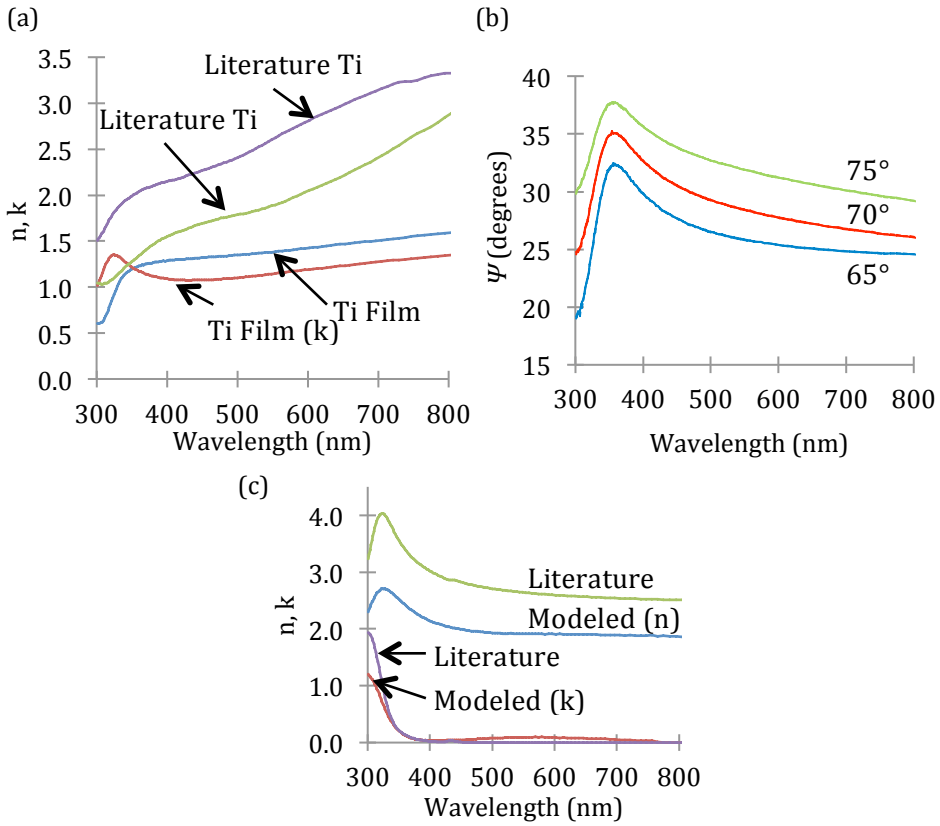

Figure 38. (a) Literature n and k values for bulk Ti and modeled n and k for a 2 micron thick Ti film (bare). (b) Experimental (dashed lines) and modeled (solid lines) Ψ from point – by – point fits starting with the longest wavelength and initial values from the Cauchy fit for the 140 mm/s sample. (c) Modeled n and k for the 140 mm/s sample obtained from the point – by – point fitting and values for bulk, literature dioxide n and k.

Using Cauchy fits, we estimate TiO_2 thicknesses for low fluence samples as follows: 140 mm/s = 8 nm, 90 mm/s = 15 nm, 80 mm/s = 22 nm, 60 mm/s = 24 nm. These are in excellent agreement with dimensions measured by TEM (included in Figure 39).

Higher Laser Fluence Results (≥ 448 J/cm^2)

For samples made with an accumulated fluence of 448 J/cm^2 or greater, a Cauchy model no longer provides a satisfactory fit in the near-IR when using the original Ti film n and k as the base layer. We expect that the oxygen-intercalated phases (Ti_xO), shown by XRD and TEM, significantly modify the Ti base layer n and k underneath the TiO_2 layer, compared with underlying Ti base layers in the lower fluence samples. In general, it was found that both the underlying Ti_xO and capping TiO_2 layer n and k need to change in order to improve the MSE and maintain physical n and k values.

For simplicity, we chose to manually adjust the Ti_xO layer n and k by preserving the shapes of the original 2 μm-thick Ti film n(λ) and k(λ) while increasing or decreasing their magnitudes. The manually adjusted Ti_xO base layers were then used for Cauchy and point-by-point fitting of the TiO_2 layer. Due to increased absorption in the TiO_2 layer in the near-IR, this modeling was restricted to the 900 nm to 1600 nm range to avoid any absorption edges.

The manually adjusted Ti_xO base layer n and k, shown in Figure 39(a), were first varied by changing the Kramers-Kronig (K-K) oscillators of the Ti_xO layer. One Drude, 2 Lorentz, and 1 Gaussian oscillator were found to accurately reproduce the real and imaginary parts of the relative permittivity of the underlying volumes. For decreasing scan speed (increasing laser fluence), the k decreased. It is seen that the modeled TiO_2 thickness is highly dependent on the assumed base Ti_xO layer n; therefore, the underlying n must be modeled with previous knowledge of the thickness of the TiO_2 film.

In a different approach, it was found that using a void:Ti EMA model for the Ti_xO base layer (rather than varying oscillators) also produced equally satisfying Cauchy fits, but the modeled TiO_2 thicknesses began to decrease with increasing fluence, in disagreement with TEM

measurements. In Figure 39(b), diamonds indicate the predicted TiO_2 layer thicknesses for an increasing void % (decreasing n and k), squares indicate the predicted thicknesses for an increasing pole magnitude (previous model description), and triangles indicate average measured layer thicknesses from HAADF TEM images. The measured TiO_2 layer thicknesses from HAADF cross-section TEM images increase with F_{acc} for all scan speeds, shown in Figure 39(b).

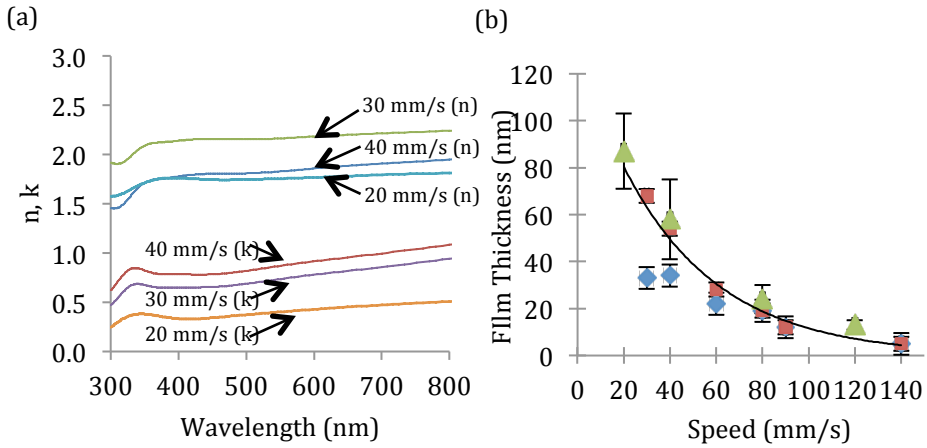

Figure 39. (a) Modeled Ti_xO base layer n and k for samples fabricated at different laser scan speeds. (b) Estimated dioxide layer thicknesses from Cauchy fitting and measured values from TEM data. Diamonds in (b) are the predicted TiO_2 layer thicknesses for an increasing void % in the base layer, squares indicate the predicted thickness for a varying oscillator modeling approach and triangles are measured value from TEM.

The results from the point-by-point (varying oscillators approach) fitting of the TiO_2 layer n and k for select scan speeds are shown in Figure 40. This includes two samples made with high fluence (scan speeds were 40 mm/s and 30 mm/s). For comparison, we include the modeled n and k of two low fluence samples (scan speeds 90 mm/s and 60 mm/s). These latter two samples used the original 2 µm-thick Ti base layer as described in the previous section.

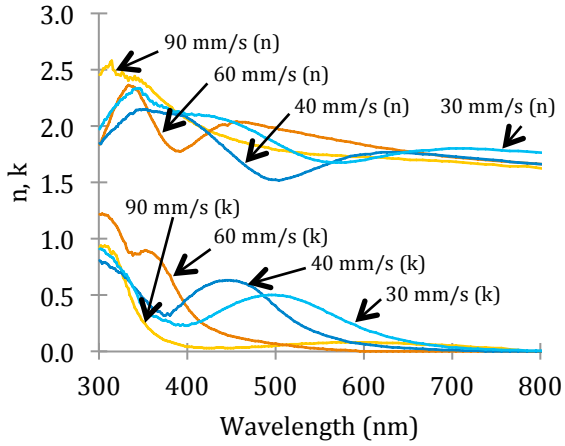

Figure 40. Modeled n and k for the TiO_2 layers formed using different laser scan speeds. Results were obtained from point-by-point and Cauchy fitting using the bare Ti as the base layer for scan speeds ≥ 60 mm/s and the modified Ti_xO base layer for speeds < 60 mm/s.

As seen by other groups [44], the results in this figure show a shifting band-edge with increasing laser fluence. Despite clear trends in k, and taking into account fluence-dependent changes to the underlying Ti_xO layer, we do not see trends in the modeled TiO_2 n with thickness or fluence. Furthermore, it was found that the TiO_2 n and k curves are not entirely K-K consistent. The lack of K-K consistency in absorbing regions is the result of working with an unknown Ti_xO base layer and making assumptions about its optical constants.

For comparison, Figure 41 shows the closest K-K consistent solutions for the modeled TiO_2 layers, constructed using Gaussian oscillators to closely match the tabulated, point-by-point fit TiO_2 layer k. Again, one finds a shifting band-edge with increasing laser fluence. Several samples described by Figure 41 exhibit a band edge that is well above 400 nm, with a few high fluence samples having a band edge well into the near IR. Of note, this approach worked well for all but the 20 and 10 mm/s samples, wherein no absorption was found for $\lambda < 400$ nm. It is possible that laser-induced defects have significantly changed the band structure of the TiO_2 layer, as compared to samples made at > 20 mm/s, complicating the model.

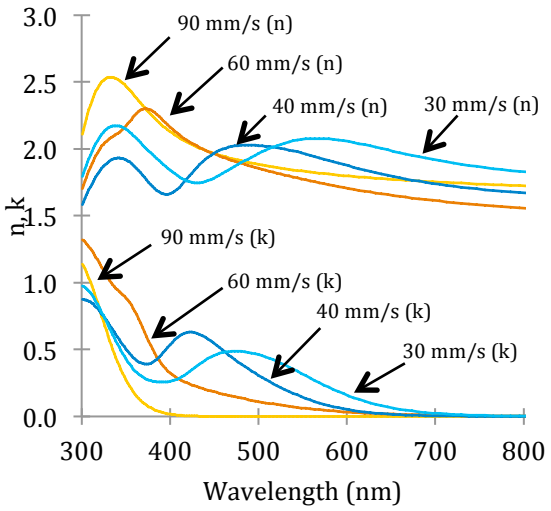

Figure 41. Kramers-Kronig consistent solutions of n and k for oxide layers made at different scan speeds. The solutions were modeled using Gaussian oscillators to reproduce the fitted k values.

The modeled n and k from ellipsometry were used to predict the reflectance (%R) for high fluence samples. A comparison with measured %R is shown in Figures 42(a) and (b). It can be seen the positions of the minima and maxima are in well agreement, but their magnitudes are different. This could be due to the differences in the detectors of the ellipsometer and the spectrophotometer, but could also be affected by the model overestimating the magnitude of the TiO_2 layer k.

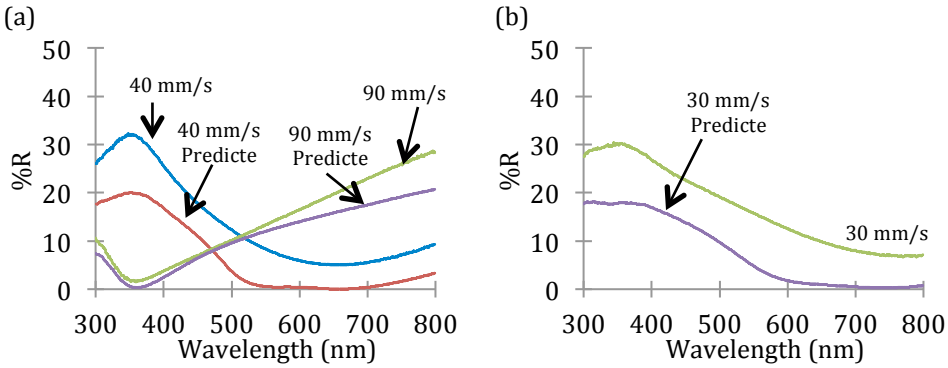

Figure 42. Measured and modeled %R for Ti oxide samples made using scan speeds of (a) 90 and 40 mm/s and (b) 30 mm/s.

With increasing laser fluence, the most significant changes to the Ti-oxide system are TiO_2 growth, increased absorption in the TiO_2 layer, and changes to the underlying Ti_xO layer n and k. We depict the lower and higher fluence regimes in Figure 43, and for the top two layers, the elements listed are those which are optically active in the system. The "modified Ti" layer represents defects in the sputtered Ti film formed by laser irradiation, visible in the TEM cross-section images.

For lower fluences (< 448 J/cm^2) in Figure 43(a), a TiO_2 layer is formed on Ti. TEM indicates that there is some modification to the underlying Ti in this regime, but the relative contributions to optical properties are not significant.

As depicted in Figure 43(b), higher fluences (≥ 448 J/cm^2) have measurable effects on the TiO_2 layer k and produce a Ti_xO ($x \geq 2$) base layer. In addition to interference effects, changes to the TiO_2 layer k change the intrinsic optical properties of the film [38] and, hence, influence the perceived color of the Ti-oxide system. There is no evidence for nitrogen incorporation or formation of titanium nitride, as sometimes seen by other groups [49]. Therefore, for higher laser fluences, it is expected that Ti and O defects, and possible O vacancies [50,51], have the largest effects on the TiO_2 layer optical properties. It is speculated that these narrow the band gap of the dioxide or introduce new absorption states [52], represented as a defective oxide (TiO_2^{def}) layer in Figure 43(b). Ti and/or O point defects, vacancies, or Frenkel defects [53] may be present in the TiO_2^{def} layer but these were not distinguished by XRD or TEM analysis.

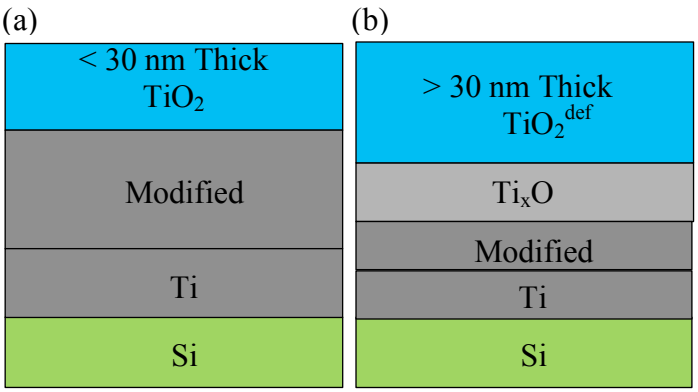

Figure 43. (a) Illustration of the Ti-oxide system for lower laser fluences. The main contributor to color is an increased stoichiometric TiO_2 layer thickness. (b) Illustration of the Ti oxide system created by higher laser fluences.

The shape of the index of refraction is not the same as literature rutile and may be an artifact of using an assumed Ti_xO base layer. The decrease in the absorption peak for the modeled k for 20 mm/s and 10 mm/s samples may be a shortcoming of the model when we assume the underlying base layer n and k for higher laser fluences, since TiO_2 is typically absorbing in these regions. Therefore, our model best describes the edge of the TiO_2^{def} k vs. λ curves, rather than the actual shape of the TiO_2^{def} k vs. λ curves.

By correlating ellipsometric models with TEM measurements of the TiO_2^{def} layer thickness, we found the Ti_xO layer is affected by oxidation by a decrease of the Ti_xO k. The model generally predicts the k for the underlying Ti_xO layer, but fails to predict the Ti_xO layer n or TiO_2^{def} layer thickness. This is a consequence of the Cauchy fitting not being very sensitive to the Ti_xO layer n, and the TiO_2^{def} layer thickness must be measured and used in the model to find the best fit Ti_xO layer n.

Since the underlying Ti_xO layer n increases and the k decreases with increasing laser fluence, the oxygen concentration in the Ti_xO layer is likely increasing with laser fluence [20]. Oxygen diffusion will be temperature driven and a higher temperature gradient with increasing laser fluence will allow for more O diffusion into the Ti_xO layer before thermal quenching.

Oxidation of layers below the TiO_2 layer in bulk samples has been observed using x-ray photoelectron spectroscopy [54], and we show here that this affects the n and k of the underlying reflective layer, and the modeling results of the TiO_2^{def} layer.

The peak laser intensity used in the current study was 7.4 x 10^5 W/cm^2, and for studies of bulk Ti the peak intensity ranged from 4 x 10^6 W/cm^2 to 5.6 x 10^6 W/cm^2.[55] Ti films require lower laser intensities to grow oxide layers (as compared to bulk) since they may stay hot longer than bulk Ti, due to poor thermal conductivity at the Si-Ti interface. Larger TiO_2^{def} layer thicknesses can then grow with higher defect concentrations. This is demonstrated by absorption in the near-IR for the 20 mm/s sample, which was not achievable for bulk Ti. Before such states are accessed in bulk Ti, the material either thermally quenches or molten Ti is formed and removed. Observed changes to the TiO_2^{def} n and k should be viewed as being close to the actual values and are a convolution of fluence-dependent variations in the TiO_2^{def} layer's thickness, n, and k with variations in the underlying Ti_xO n and k.

4.4.3. Laser color marking of Cr metal films

Diced samples of Cr films on oxidized Si substrates were placed in the focus of the SPI, Inc. laser operated with a 1064 nm wavelength (λ), 120 ns pulse length, focused $\frac{1}{e^2}$ diameter of ~ 80 μm, average power = 4.0 W, and a repetition rate = 400 kHz. The Gaussian, focused laser beam was rastered across the film samples with galvanometric mirrors utilizing a hatch spacing = 10 μm and scan speeds of 140, 70, 50, and 30 mm/s to grow chromium oxide. The accumulated fluence is calculated as $F_{acc} = \frac{P_{avg}N_p}{A*v}$ where P_{avg} is the average power, N_p is the total number of pulses over a given area A, and v is the repetition rate. The accumulated laser fluences used for

laser coloring of Cr films were 290 J/cm^2, 570 J/cm^2, 800 J/cm^2, and 1.3 kJ/cm^2. All films are irradiated in air.

Ellipsometric measurements of oxidized Cr films were obtained from a J.A. Woollam Co., Inc. rotating-analyzer spectroscopic ellipsometer at angles of 65°, 70°, and 75° for each sample over a wavelength range from 300.2 nm (4.13 eV) to 1000.0 nm (1.24 eV) at 0.02 eV step sizes. Modeling and mean squared error (MSE) analyses were performed using the standard J.A. Woollam WVASE32® software. Models were fit to the measured quantities Ψ and Δ, where $\frac{R_p}{R_s} = \tan\psi\, e^{i\Delta}$ and R_p and R_s are the complex Fresnel reflection coefficients for p- and s-polarized light respectively. All ellipsometric models were considered planar, with no surface roughness effects. Effective medium approximation (EMA) layers were constructed using the Bruggeman effective medium models in the J.A. Woollam WVASE32® software.

Grazing incidence X-ray diffraction (XRD) data were collected using a Siemens D500 diffractometer. XRD utilized CuKα radiation (λ = 0.15418 nm). Cross-section transmission electron microscopy (TEM) samples were prepared using an ex-situ, focused ion beam lift-out method. High-angle annular dark-field (HAADF) imaging, and energy-dispersive X-ray spectroscopy (EDS), were performed using a FEI Co. Titan G2 80-200 probe aberration-corrected TEM operated at 200 kV. Auger electron spectroscopy (AES) was performed to examine the elemental distributions at different depths. The AES instrument was a Physical Electronics Auger 690 system with a base pressure less than 2 x 10^{-9} Torr A Physical Electronics 06-350 floating column ion gun, with extractor pressure in the ionization feedback controlled to 25 x 10^{-3} Pa, was employed. Xenon was used as the sputter gas, and Auger data were acquired with a 10 kV, 10 nA electron beam.

The spectral reflectance of oxide coatings was measured using a Varian Inc. Cary 5000 UV-Visible-IR spectrophotometer. An integrating sphere, internal diffuse reflectance accessory collected both the specular and diffuse reflectance.

4.4.3.1 Phase, microstructure and reflectance of oxides produced on Cr films

Figure 44(a)-(d) show bright-field optical images of Cr films after irradiation with laser light made using scan speeds of 140, 70, 50, and 30 mm/s respectively, and Figure 44(e) shows representative grazing incidence XRD patterns obtained from a 140 mm/s sample. The XRD patterns do not significantly differ between samples. The color of the films progresses from gold to darker gold to a mixture of colors for decreasing scan speed (increasing laser fluence). Oxide layers and underlying Cr remain well adhered after all laser processes; there is no evidence for delamination. The peaks in the XRD patterns indicate Cr_2O_3 has formed. Peak positions are slightly shifted to higher 2θ (which means a contracted unit cell) compared with published patterns for Cr_2O_3 [56]. This indicates that the Cr_2O_3 layer may be sub-stoichiometric or that the layers are subjected to a moderate in plane, compressive stress.

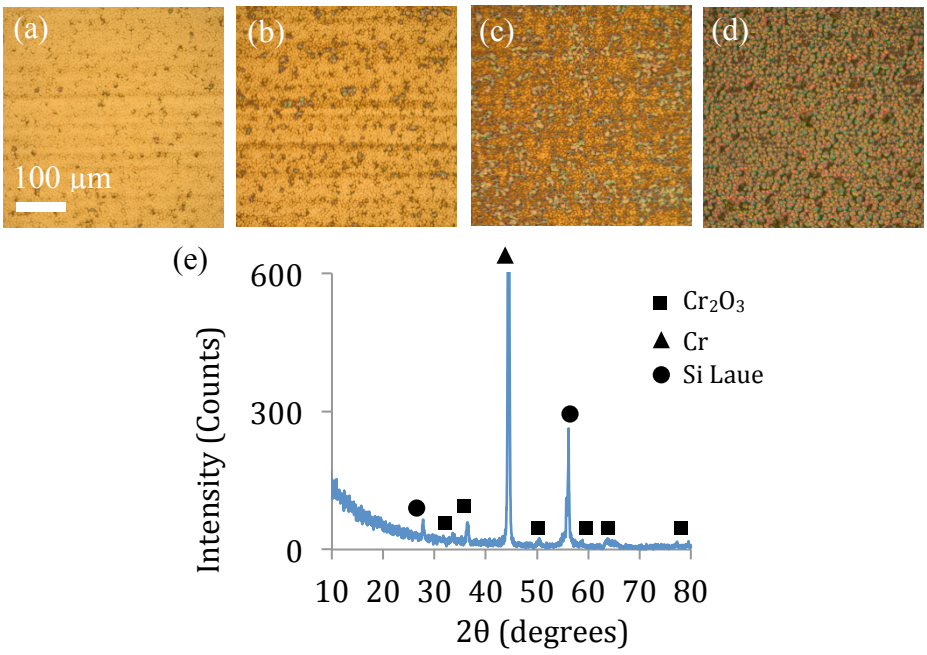

Figure 44. Bright field optical, plan view images of Cr oxide layers on Cr thin films after nanosecond laser irradiation in air using scan speeds of (a) 140, (b) 70, (c) 50 and (d) 30 mm/s. (e) shows a grazing incidence XRD pattern for a sample made using a scan speed of 140 mm/s demonstrating Cr_2O_3.

For an improved understanding of the structure of underlying volumes, we turn to cross section TEM and EDS compositional mapping of the various samples. HAADF images and accompanying maps included in Figs. 45(a)-(d) show the presence of continuous Cr_2O_3 layers at the surface of films. In all cases, it is apparent that an oxide capping layer forms but the original Cr film is no fully oxidized. Alternating Cr and Cr_2O_3 volumes are present underneath each Cr_2O_3 layer. It is apparent that a columnar Cr microstructure[57] formed during sputter deposition, and this is modified during laser treatment. Specifically, the images in Figs. 45(c) and 45(d) show evidence of significant oxidation between Cr grains and some oxidation within individual crystals. Preferred oxidation along boundaries and interfaces can be expected, due to the enhanced diffusion rates of ionic species along grain boundaries and interfaces [58].

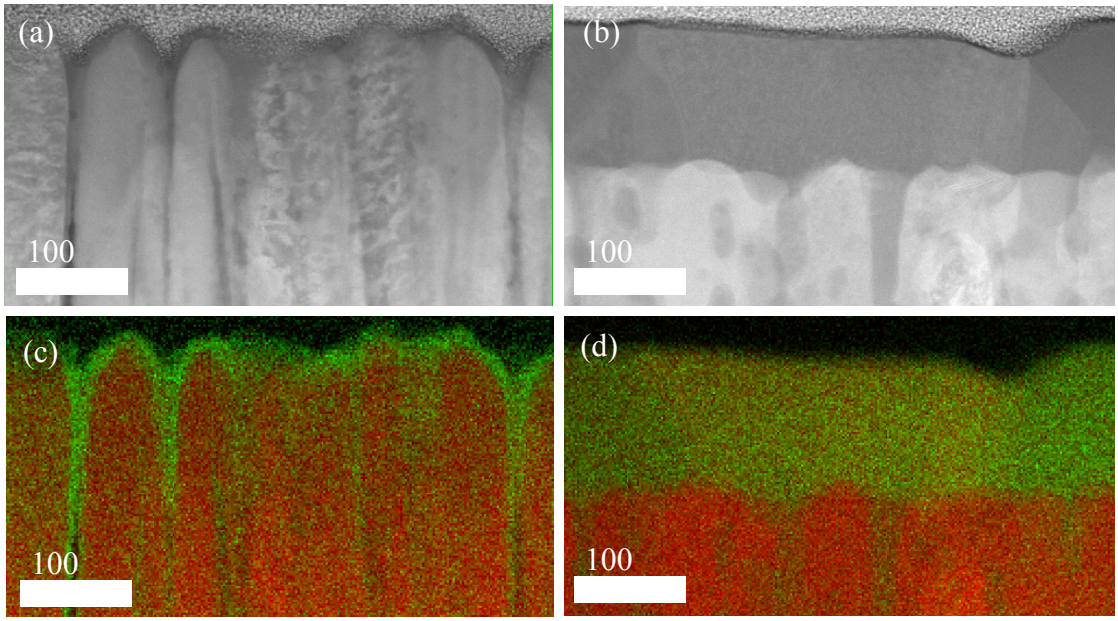

Figure 45. Cross section TEM images of Cr films after laser irradiation in air using scan speeds of (a) 140 and (b) 30 mm/s. EDS maps of the same sample areas are included in (c) and (d), respectively. Green represents Cr-O and red represents pure Cr.

High-resolution TEM images for the 140 mm/s and 30 mm/s samples are shown in Figures 45(a) and (b) respectively to demonstrate the nature of produced oxide layers. Lattice fringes are apparent in both images, indicating polycrystalline Cr_2O_3 layers are formed. TEM does not reveal embedded amorphous volumes. Detailed inspection of the Cr_2O_3 layer shown in Fig. 45(b) reveals that it is filled with pores. The top two optically active layers visible in TEM are illustrated in Figures 45(c) and 45(d), with the pores illustrated as dark features in Figure 45(d). Furthermore, EDS shows no evidence of nitrogen in samples. This includes capping oxide layers as well as underlying, reflective base layers. These observations are consistent with depth-profiling AES studies which penetrate to compositionally pure portions of the Cr films.

4.4.2.1 Detailed optical properties revealed by ellipsometry

Figure 45(a) shows the optical constants of bulk Cr from the J.A. Woollam WVASE32® software (similar to those reported in the *literature* [59]), those determined from a *bulk* Cr specimen (99.9% purity) using ellipsometry, and those determined from a 1 μm-thick Cr *film* using ellipsometry. In the last two cases, a 2 nm-thick Cr_2O_3 film is assumed present on the surface of the Cr [60]. The bulk Cr n and k are similar to literature values and verify our methods and assumptions. Large differences are found for the n and k of deposited 1 μm-thick Cr films versus bulk Cr, for the range of specified wavelengths (300 to 1000 nm). The n and k of the modeled Cr film closely resemble the n and k of electron-beam deposited, columnar Cr films [61].

Fig. 46(b) and Fig. 46(c) include the measured Ψ for a sample made using a laser scan speed of 140 mm/s. Measured Ψ are shown with dotted lines in both of these plots. Also included in Fig. 46(b) and 46(c) are results from different model predictions. In Fig. 46(b) the Ψ shown with solid lines are generated from models of a 5 nm Cr_2O_3 (utilizing bulk optical constants) adhered to thick Cr (using its bulk optical constants). Model predictions are shown for each angle (i.e., 65°, 70°, and 75°) using solid blue, red and green lines, respectively. In Fig. 46(c), the Ψ generated from a different model are included. Model predictions included in the latter plot 46(c) utilized a slightly larger oxide thickness (6.8 nm). Importantly, this additional model used the n and k determined for our sputter-deposited Cr films, shown in Fig. 46(a).

Comparing the plots in Fig. 46(b) and (c), it is apparent that the latter model, which includes measured Cr films as an underlying material, is much better than a model that incorporates bulk Cr. In the near-IR, the predicted values are nearly identical to the measured Ψ. This means that, after laser heating for lower accumulated fluences, the underlying Cr is similar, in

large respect, to the original film. For wavelengths < 600 nm, the fit is poor. One can expect that the n(λ) and k(λ) of this Cr_2O_3 layer are different than values cited in the literature for bulk Cr_2O_3, and this particular underlying Cr base layer has possibly been modified by laser irradiation.

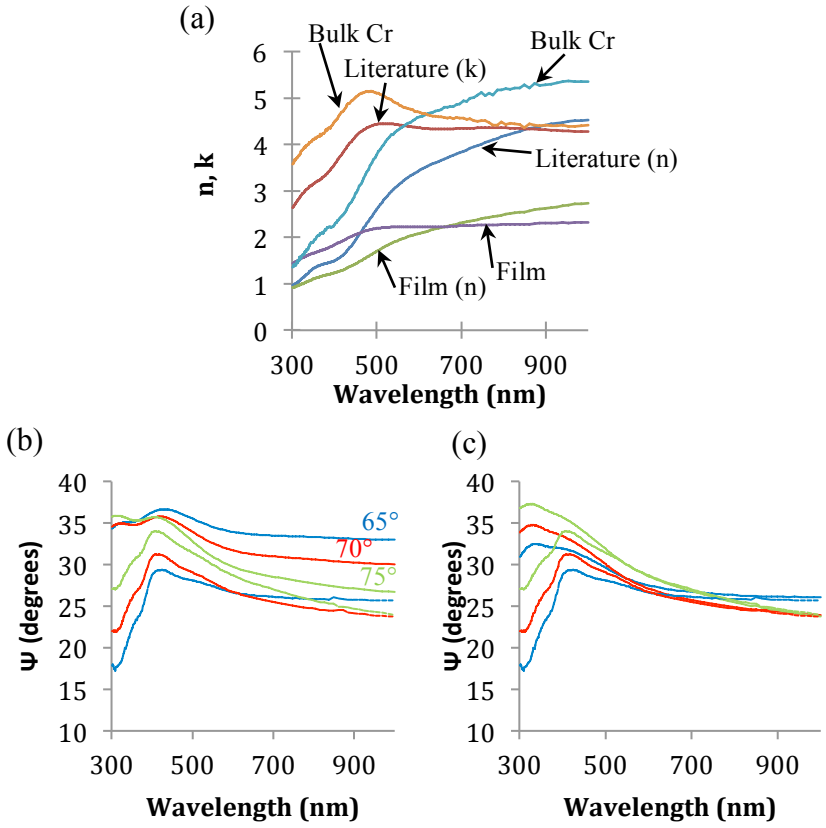

Figure 46. Optical constants (n, k) for bulk Cr as reported in the literature, a bulk Cr specimen used in this study and 1 μm thick sputter deposited Cr film. (b) Experimental Ψ (dashed lines) are shown for an oxide made using a fluence of 290 J/cm^2, along with predicted Ψ (solid lines) assuming 5 nm of Cr_2O_3 on Cr. In this model, the optical constants of the oxide are taken from the literature. The optical constants of sputter deposited Cr are taken from (a).

To improve the fit of the thickness, the n and the k of the Cr_2O_3 layer are allowed to change. First, we perform a Cauchy fit in transparent regions (λ > 700 nm) to obtain approximate thicknesses of the Cr_2O_3 layers. Then we fix the Cr_2O_3 thickness and perform a point-by-point fit of the Cr_2O_3 n and k for all λ, starting with the longest λ. The resulting Ψ from fitting are shown in

Fig. 46(a) for a sample made with a scan speed of 140 mm/s, and included are results for each of the three angles used in experiment. The resulting n(λ) and k(λ) for the Cr_2O_3 layers made using scan speeds of 140, 70, and 50 mm/s are included in Fig. 47(b).

In general, the n and k of modeled oxide layers are larger than values cited in the literature for bulk Cr_2O_3 for most wavelengths. In addition, the k of all laser-grown samples extended further into the visible region than bulk Cr_2O_3. We speculate that this is due to defect formation in the Cr_2O_3 layers. It is noted that this model demonstrates increased k for samples treated at higher laser fluence.

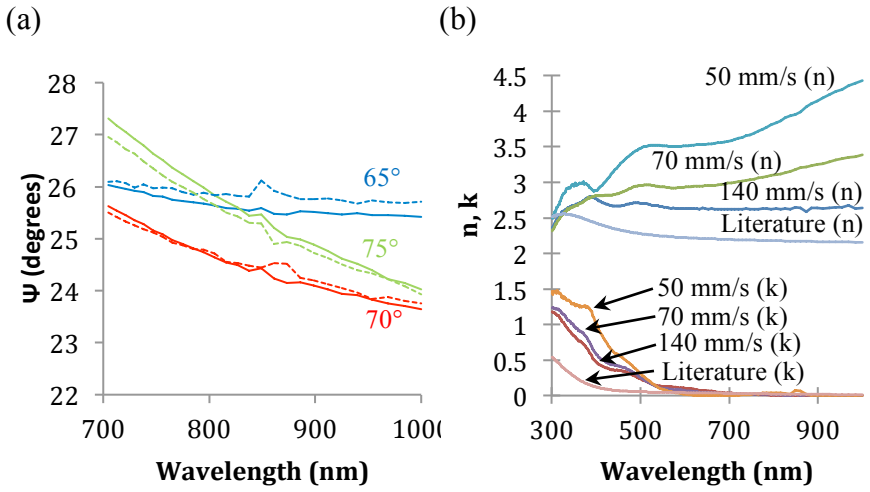

Figure 47. (a) Experimental Ψ (dashed lines) and modeled Ψ (solid lines) from fitting the thickness and fit constants for a sample made using a scan speed of 140 mm/s. In this model a Cauchy layer is used to represent the Cr_2O_3 and the underlying Cr is assumed to be identical to unmodified, sputter deposited Cr films. (b) Optical constants for bulk Cr_2O_3 described in the literature and resulting n and k for samples made at 140, 70, and 50 mm/s after point-by-point fitting n and k.

Although improved, this model is not satisfactory for any sample. The data shown for the samples in Fig. 47(b) reveals nonphysical n for Cr_2O_3 in non-absorbing regions (k = 0), where n increases with increasing λ. This means that for all samples we are using the incorrect base layer

for fitting and that additional adjustments are required. It is expected that laser irradiation has significantly changed the underlying Cr film.

Reflecting the structure found using TEM, additional refined models treat the underlying columns as a two-phase Cr:Cr_2O_3 EMA base layer. An EMA is justified since the optical penetration depths of the underlying Cr columns and Cr_2O_3 boundaries are much smaller than the wavelength of light [62]. The thickness of this EMA layer is correlated in the models, so we must assume an EMA layer thickness. The EMA layer assumes that the constituent oxide is Cr_2O_3 and its optical properties are like that of bulk oxide. Evidence for crystalline Cr_2O_3 underlying base volumes come from high resolution TEM (and diffraction analysis) conducted near the top portion of columnar grain boundaries of laser-irradiated samples.

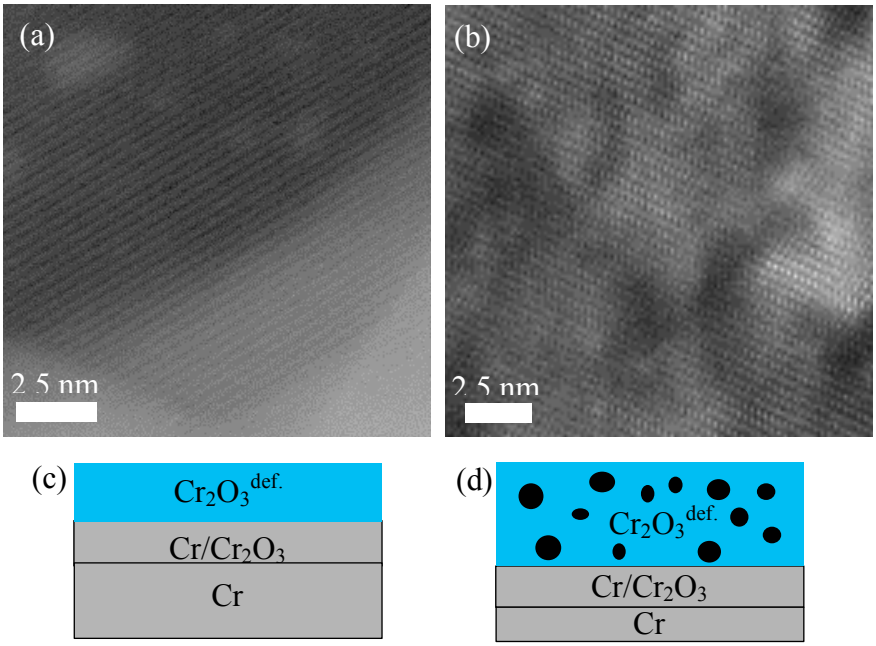

Figure 48. (a) High resolution TEM image of the Cr oxide layer after laser irradiation using a scan speed of 140 mm/s. The bright feature in the bottom, right corner is underlying Cr metal. (b) High resolution TEM image of a thicker Cr oxide layer made using v = 30 mm/s. The contrast indicates a significant number of pores and other defects have formed in this layer. (c) An illustration for lower laser fluence samples of a defective Cr oxide layer. (d) An illustration for higher laser fluence samples.

The structures depicted in Figures 48(c) and (d) were used in these refined models to recalculate the n(λ) and k(λ) of the Cr_2O_3 layers. Again, we implement Cauchy and point-by-point fitting. For each sample, the volume % of Cr_2O_3 in the Cr:Cr_2O_3 base layer EMA structure was increased by 1% until the modeling returned physical overlying Cr_2O_3 layer n(λ) curves. The models predict that the 140 mm/s sample formed an oxide layer thickness of 8.9 nm (MSE = 6.8), and its underlying base layer was 2% Cr_2O_3 by volume; and the 70 mm/s sample formed an oxide layer thickness of 18 nm (MSE = 2.7) with the underlying mixed base layer composed of 24% Cr_2O_3. For the 50 mm/s sample, the Cr_2O_3 layer n was found to be physical only if the underlying reflective layer is further modified using a more complex Cr:Cr_2O_3:void EMA layer. In this sample, the Cr_2O_3 thickness was estimated to be 22 nm (MSE = 4.7), and the underlying base layer was 24% Cr_2O_3 by volume and 30% voided.

Fig. 49(a) plots the n and k of the Cr_2O_3 layers, and the n and k for the underlying Cr:Cr_2O_3 base layers are included in Fig. 49(b). Different than the previous models, the n of Cr_2O_3layers does not increase in non-absorbing regions (k = 0) giving credence to the predicted results. Fig. 49(a) again demonstrates nonzero k for the Cr_2O_3 layers over a broader range of λ, toward the near IR, suggesting a significant role of defects produced by laser oxidation. In addition, it can be seen in Fig. 49(b) that the n(λ) and k(λ) of the EMA Cr:Cr_2O_3 layer have similar shapes to the as-deposited Cr film n and k (also included for reference, labeled "original"), but have shifted.

Figure 49(c) shows the measured and predicted Cr_2O_3 layer thicknesses. The ellipsometric estimates of Cr_2O_3 layer thicknesses agree well with TEM measurements as predicted values are within a standard deviation of the measured values. TEM and model predictions show that Cr_2O_3 thickness increased with accumulated fluence (decreasing scan speed). This can be expected since more heat is provided to a given surface area.

For the oxide sample made using a scan speed of 30 mm/s, laser irradiation changed the Cr and overlying Cr_2O_3 layer enough that a satisfactory ellipsometric model could not be found to predict the same thickness as measured by TEM. However, various tested conditions, such as different underlying Cr substrates with oxide and void models, all predicted that the 30 mm/s sample was only absorbing in the visible region.

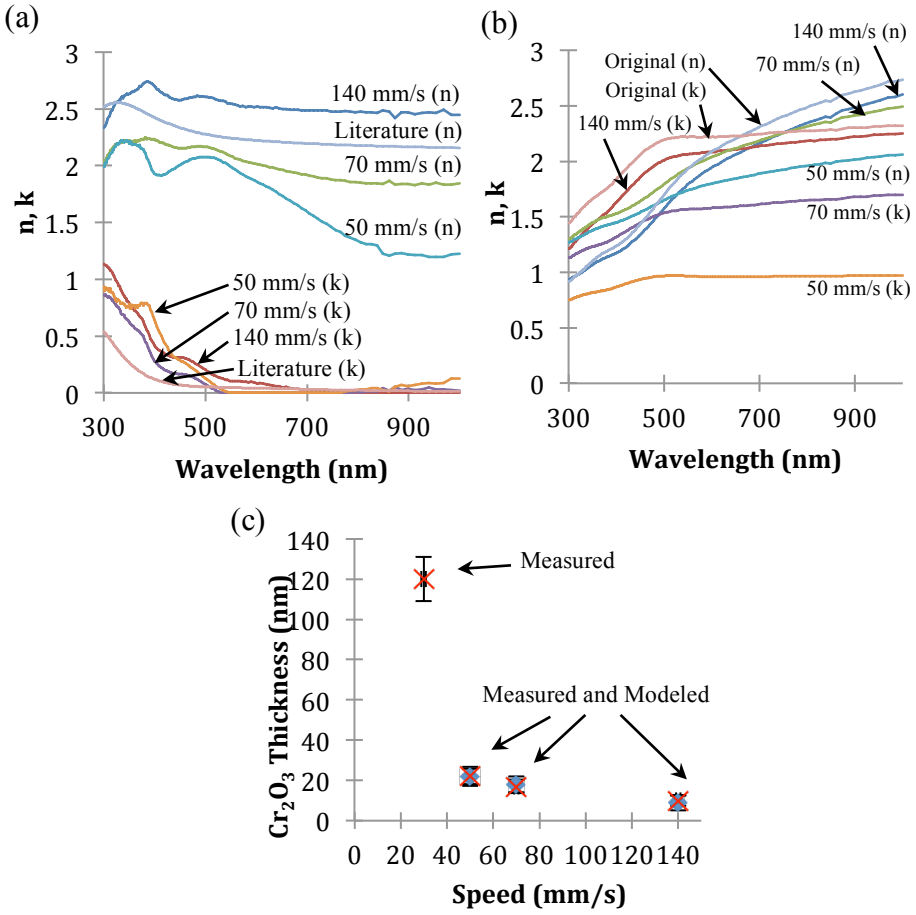

Figure 49. (a) Modeled n and k vs. wavelength for samples made using scan speeds of 140, 70 and 50 mm/s. These models assumed a Cr:Cr_2O_3 base layer and the volume fraction of the oxide in this layer increased with decreasing laser scan speed. (b) The n and k of bare 1 micron thick Cr and the Cr: Cr_2O_3 EMA layers for oxides made at various speeds. (c) Measured (X) and modeled (◆) Cr: Cr_2O_3 layer thicknesses for the 140, 70, 50 and 30 mm/s samples.

The predicted k vs. λ for samples 140 mm/s, 70 mm/s, and 50 mm/s do not significantly change with increasing fluence, but each sample has an absorption coefficient which is larger than literature Cr_2O_3 and extends further into the visible range. This suggests that laser-induced growth of Cr_2O_3 introduces defects into the Cr_2O_3 layer, which increases the k, but the number of defects is not significantly changing with increasing fluence, with the exception of the 30 mm/s sample. By slightly adjusting the Cr_2O_3 percentage in the underlying Cr, we can find various n vs. λ curves for the Cr_2O_3 layer with the same MSE.

Further confirmation of accurate models is made by comparing the measured and modeled reflectance (%R) for each sample. The measured reflectance for the 140 mm/s, 70 mm/s, and 50 mm/s samples are shown in Figure 50(a) – 7(c). It can be seen that the 140 mm/s and 70 mm/s samples have similar R(λ), and hence colors, while the curve for the 50 mm/s sample differs significantly in qualitative agreement with the color variations shown earlier. The predicted R(λ) of the 140 mm/s, 70 mm/s, and 50 mm/s samples are also shown in Figures 50(a) – (c). While the absolute magnitude of the predicted %R is significantly lower than the measured samples, the curves are in good agreement. The lower %R values of the modeled samples are likely due to the different areas of ellipsometer and spectrometer detectors. The spherical detector collects both the specular light and diffuse light scattered by rough surfaces, resulting in a greater %R magnitude. A lower predicted %R could also be due to over estimations of the Cr_2O_3 layer k in the ellipsometric models.

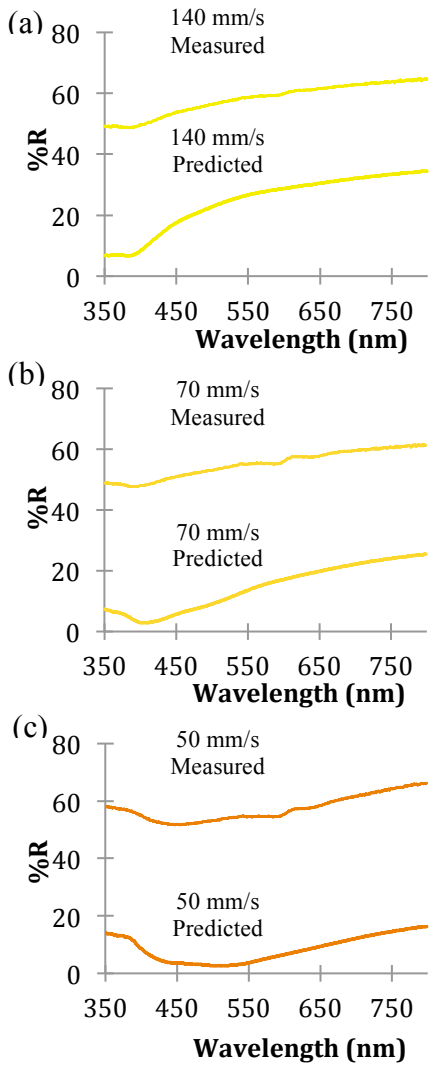

Figure 50. Measured and modeled R(λ) of laser-fabricated Cr_2O_3 layers made using scan speeds of (a) 140 mm/s, (b) 70 mm/s and (c) 50 mm/s. The curve colors resemble those observed.

Comparing all three plots in Figure 50, we find a trend with increased accumulated laser fluence (with decreasing scan speed). The measured R(λ) curves exhibit broad maxima and minima consistent with constructive and destructive interference effects. As the laser fluence is steadily increased, the minima shift to higher wavelength consistent with a larger oxide thickness. Near-identical shifts of reflectance minima are revealed in the predicted R(λ) derived from the refined ellipsometric models.

4.6. Effects of Environment on Laser-defined Oxide Coatings

4.6.1. Mechanical Response

Nanoindentation is a viable method for studying the mechanical behavior of films such as those grown in this work[63]. Nanoindentation is traditionally used to obtain mechanical properties of small volumes, but can be applied in innovative ways to evaluate film fracture behavior and residual film stresses *ex situ* or electromechanical behavior *in situ*. Sudden excursions in depth (pop-ins) at low loads during load-controlled nanoindentation in substrate-film systems are often ascribed to oxide film fracture. Indentation experiments using a conductive stage/tip system allow for the investigation of the combined electrical and mechanical response of bulk and film/substrate materials systems.

Most thin film nanoindentation studies involve films grown by physical vapor deposition, chemical vapor deposition, or electroplating. The mechanical properties of oxides fabricated by pulsed laser irradiation have not been studied in detail. Our study investigates classical thin-film properties of coatings made using a different far-from-equilibrium growth technique as well as develops novel test techniques. This study focuses on linking the mechanical properties of oxides produced on SS 304L to the microstructure and phase produced by pulsed laser irradiation.

4.6.1.1. Mechanical Behaviors of Oxides produced on Stainless Steel

Fifteen oxide color samples were fabricated on polished austenitic stainless steel 304L substrates by rastering a 120 ns pulsed laser beam across surfaces in ambient atmospheric conditions. All oxides were created with the aforementioned Er-doped, glass-fiber laser from SPI

Lasers, Inc. operated at 5.6 W average power and pulse frequency of 225 kHz with scan speeds ranging between 30-600 mm/s. The focused laser beam was approximately Gaussian with a $1/e^2$ width of 59 mm. Multiple overlapped laser scans with a centroid-to-centroid (hatch) spacing of 10 μm created 4 x 4 mm areas for testing. Faster laser scan rates correspond with lower laser fluence (energy density).

The resulting oxide thickness, microstructure, phase, and composition of these films has been reported previously [64,65]. Nanoindentation measurements to determine mechanical properties were conducted with a Nanoindenter XP with a dynamic contact module (DCM) for low load testing, using both the quasistatic mode (QS) for load-controlled testing and the continuous stiffness module (CSM), with tests performed at a frequency target of 75 Hz and a depth target of 1 nm with a 350 nm depth limit, producing stiffness, modulus, and hardness, values. A Berkovich probe with a radius of approximately 150 nm was used for mechanical property testing. Fracture behavior of the oxides was also examined with nanoindentation; a 90° conical indenter tip with a nominal radius of 1 μm was pressed in to a surface using the XP module with peak loads of 20 mN, 35 mN, 50 mN, and 80 mN. Indents were then imaged with FEI Sirion and JEOL JSM7600F scanning electron microscopes (SEM) and image-processing software was used to determine crack circumferences. Finally, electrically-conducting nanoindentation was employed to evaluate the electromechanical properties of certain films, including the conductance and polarization (I-V) characteristics using a Hysitron Triboindenter 950 with electrical contact resistance (ECR) measurement capability and a boron-doped diamond Berkovich indenter. Electrical data was collected in voltage-source mode during the 10 mN hold segment of the loading cycle. Sweeps were 2 s long and were directed from -10 V to +10 V.

The oxides grown in this study range in thickness between < 20 nm to 490 nm and have a topography consisting of a series of ridges and valleys. Laser fluence dictates film thickness; oxides grown at faster scan rates (lower fluence) are thinner than those fabricated at slower scan rates. Figure 51a presents an SEM micrograph of the typical surface topography; the inset is an atomic force microscopy (AFM) reconstruction highlighting a single ridge and valley period. The rippled topography is a result of overlapping laser passes and is thus less obvious as oxide thickness decreases.

Surface channel cracking is observed as oxide thickness increases (Fig. 51b). Pervasive, interconnecting, through-thickness cracks typically develop in a strained film as a means to relieve residual film stresses resulting from differences in coefficients of thermal expansion between the substrate and the film [66,67]. It is therefore likely that residual stress increases as oxide thickness increases. Below an oxide thickness of ~100 nm (corresponding to a laser scan rate of ~400 mm/s) channel cracking is not observed. Away from indents, Figure 52(a)-(e) shows the reduction in the quantity of channel cracks with decreasing film thickness.

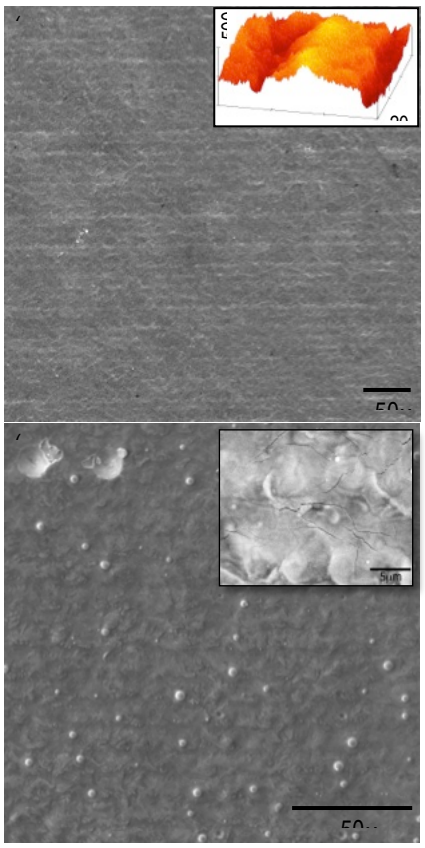

Figure 51. SEM image showing rippled surface topography. Right inset is an AFM reconstruction of a single ridge-valley period. This oxide layer was made using an average power of 5.6 W and a scan speed of 30 mm/s. (b) SEM micrograph showing pervasive surface cracks formed post-processing to relieve residual stress. This particular layer was made with the same P_{avg} and v = 47 mm/s.

Transmission electron microscopy (TEM) and energy dispersive spectroscopy (EDS) indicate that the oxide phase structure changes at thicknesses less than 200 nm (corresponding to a scan rate of > 250 mm/s). As shown in earlier oxides with thicknesses greater than ~200 nm develop a two-phase structure consisting of a Cr-rich interfacial layer containing Mn (likely $MnCr_2O_{4)}$ and an Fe-rich overlayer (Fe_3O_4). Conversely, at thicknesses less than ~200 nm, the films are a single Cr-rich layer containing some Mn and Fe with no Fe-rich oxide cap.

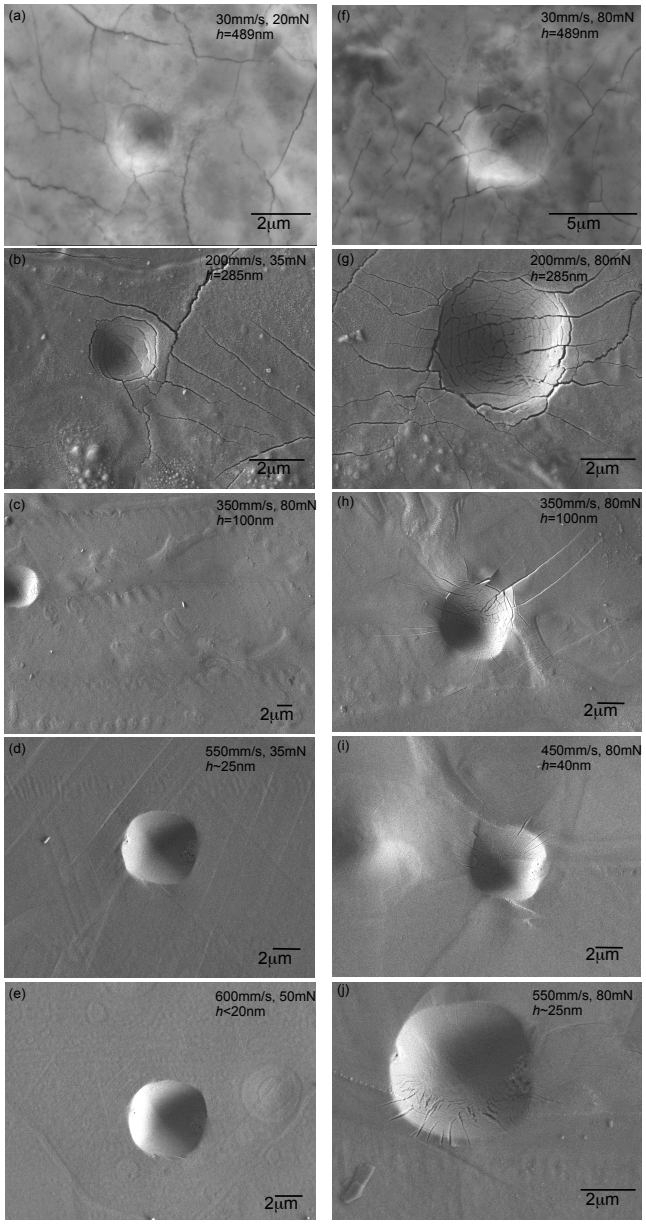

Figure 52. SEM images showing high load nanoindents. These demonstrate the reduction in surface cracking with decreased oxide layer thickness, h. In (a) - (e) laser scan rate is increased and the oxide thickness is reduced. There is a shift from circumferential cracking to radial cracking as thickness decreases further from (f) to (j).

Mechanical behavior of laser-fabricated oxides was probed using both dynamic and quasi-static nanoindentation methods. Dynamic nanoindentation was performed using the CSM technique, producing modulus, hardness, and stiffness values at every point throughout the test. Modulus and hardness data were evaluated in an a_c/h range of 0.5-1.0 to minimize the effects of

surface asperities and substrate properties which can otherwise skew mechanical behavior measurements during indentation [68,69]. In this analysis, a_c is the contact radius and h is the film thickness. Within this range, the indentation depth is sufficient to overcome surface asperity effects, but shallow enough to avoid the influence of the more compliant substrate. Table 6 summarizes the average hardness and modulus values obtained in the range of $0.5 < a_c/h < 1.0$. Contact radius is calculated using:

$$a_c = \sqrt{\frac{A}{\pi}}, \quad \text{Eq. 4}$$

where A is the contact area, determined via [70]:

$$A = \frac{\pi}{4}\frac{S^2}{(\beta E_r)^2}. \quad \text{Eq. 5}$$

In the prior equation, β has a value of 1.034, and has traditionally been used to account for stiffness deviations as a result of axial asymmetries of pyramidal indenters, S, the harmonic contact stiffness is measured at each point during the indentation test and the reduced modulus, E_r, is computed with:

$$\frac{1}{E_r} = \frac{(1-\nu^2)}{E} + \frac{(1-\nu_i^2)}{E_i}, \quad \text{Eq. 6}$$

where ν is Poisson's ratio of the sample (0.3), ν_i is Poisson's ratio of the indenter (0.07), E is the modulus of the sample, taken directly from continuous stiffness measurement, and E_i, is the modulus of the indenter (1141 GPa). The moduli reported in Table 6 are sample modulus values. Interestingly, the hardness of the films begins to decrease as thickness drops below 200 nm, with the greatest decrease in hardness occurring as thickness decreases below 84 nm. This thickness range corresponds with the disappearance of oxide channel cracking.

Oxide films that could be used as authenticity markers would need to be robust and resist wear and fracture. While high hardness is emphasized as a classical determinant of wear resistance [71], researchers have shown that the ratio of hardness to elastic modulus (H/E) is often a better measure of wear resistance than hardness alone [72–74]. The calculated H/E ratios for the oxides in this study are included in Table 6. Again a sharp decrease in H/E occurs below thicknesses of 84 nm, as hardness drops. While high hardness is often desirable for wear resistance, superhard or ultrahard films are also often brittle; in many cases a protective coating which is both reasonably tough and wear resistant is required. A high H/E ratio is typically an indicator of high wear resistance; in this study thicker films are likely less susceptible to wear than thin oxides.

High-load, quasi-static indentation tests can be used to obtain a semi-quantitative understanding of both oxide fracture behavior and film toughness. The spherical loading of a hard elastic plate on a soft, yielding substrate, approximates the indentation of a thick, hard film on a deformable substrate. When loaded, the plate (film) undergoes elastic deformation until brittle fracture, while the substrate is displaced plastically at relatively high loads [75]. Typically, large, circumferential cracks will occur at the plastic zone radius [66]. In contrast, spherical loading of a thin hard film on a compliant substrate results in plastic deformation of the film-substrate system; the majority of the energy is dissipated by the substrate and the film conforms to the plastic

deformation of the substrate. The film may undergo radial cracking. The stress tensor beneath the indent dictates the type of cracking initiated; radial tensile stresses are responsible for initiating circumferential cracks, while circumferential tensile stresses are responsible for radial cracks [76].

As evident in Figure 52(f)-(j), thicker oxides display concentric circumferential cracking. The corresponding load depth curves for these indents exhibit pop-ins, or a sudden increase in depth with no corresponding increase in load. These discrete events have been linked to oxide fracture events; a schematic of such an event is shown in Figure 53. Image processing software was used to measure the fracture area. In general, the outermost circumferential cracks correspond with the calculated contact area; for inner circumferential cracks, fracture contact areas correlate directly with calculated pop-in contact areas. Figure 54 exemplifies the correlation between pop-ins and observed fracture for indents in a 30 mm/s oxide and a 80 mm/s oxide. This analysis suggests load excursions recorded beyond the elastic zone are most likely film fracture events [77]. Furthermore, no spallation of the oxide is observed even when nested, concentric cracking occurs at the highest indentation loads, indicating that the film is well adhered to the steel substrate and interfacial fracture does not occur. This is substantiated by the limited delaminations observed by FIB sectioning and SEM imaging.

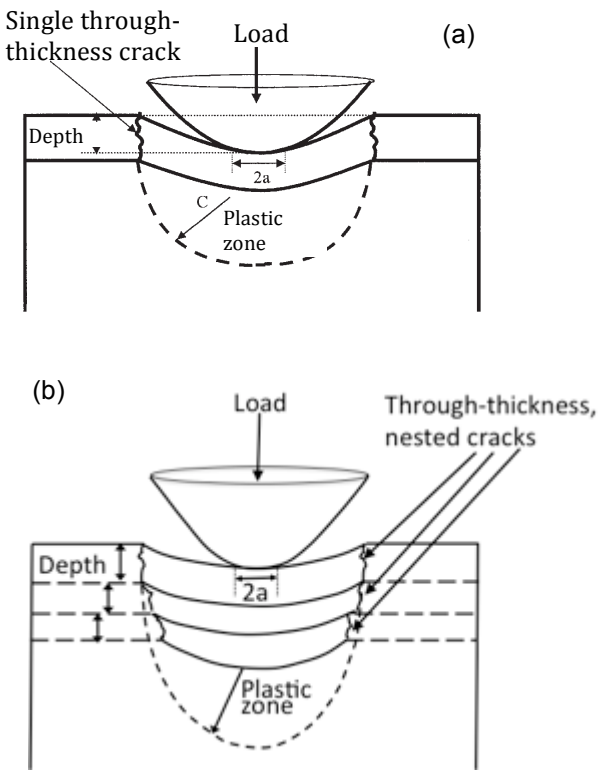

Figure 53. Schematic showing fracture of a hard film on a soft substrate at low maximum loads (a) where a single through-thickness fracture event occurs, and at maximum loads (b) where nested cracking can occur.

A clear shift in fracture mechanisms occurs at a thickness of ~100 nm, below which circumferential cracking is eliminated. It is likely that the controlling stress for initiation of fracture shifts from radial tensile to circumferential tensile as the oxide thickness decreases, resulting in the preferential development of radial, as opposed to circumferential cracks. Michler and Blank [76] investigated the stress fields required to proceed from initiation of circumferential cracks to initiation of solely radial cracks as the film thickness, h, to indenter radius, R, ratio decreased for thin hard films on compliant substrates, finding small h/R ratios led to a network of radial and circumferential cracks. In the current study, the continual decrease of thickness leads to the (1) total disappearance circumferential cracks and formation of radial cracks followed by (2), a sharp decrease in radial crack length until no cracking is observed for the thinnest oxides

(fabricated at scan rates > 550 mm/s). The critical thickness for changing fracture mechanism is the same as that at which surface channel cracking ceases to develop, suggesting that the lower residual stress experienced by well-adhered thinner oxides may impact their toughness.

Table 6. Modulus, hardness, ad H/E ratio of oxides tabulated as a function of laser scan rate and oxide thickness. Values reported for contact radius to film thickness ratios between 0.5 and 1.0.

Laser Scan Rate	*Thickness*	*Average Hardness*	*Average Modulus*	*H/E*
30	489	9.2±1.0	155±7	0.059
47	405	10.7±1.9	155±9	0.069
80	403	9.8±1.3	159±9	0.062
175	302	10.4±1.1	157±5	0.066
200	285	9.9±1.2	157±9	0.063
225	196	10.3±0.9	157±7	0.066
250	150	10.8±1.8	155±10	0.069
300	147	7.3±0.9	146±15	0.050
350	100	8.3±2.0	159±16	0.052
400	84	6.3±1.2	150±17	0.042
450	65	4.9±0.6	141±12	0.035
500	40	4.7±1.4	148±18	0.022
*550	~25			
#600	<20	N/A	N/A	N/A

*thickness extrapolated from thicker oxide measurements; values are an estimate

thickness not measured

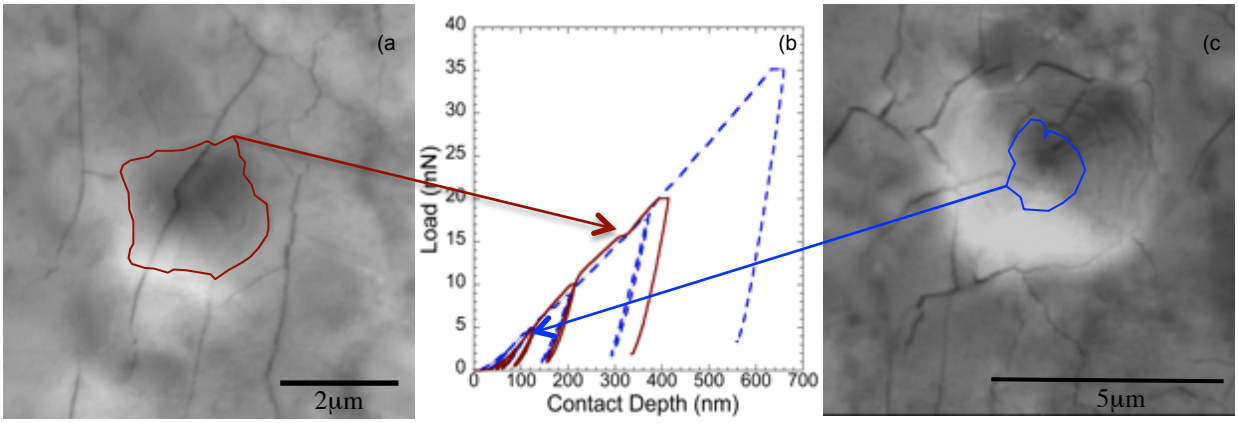

Figure 54. Circumferential cracks at contact radius correspond to load-depth excursions at higher loads (a), while inner, nested cracks in high-load indents correlate with excursions at low loads (c).

The previously shown XRD indicates that within the identified critical thickness range the oxide phase may cease to be a duplex $MnCr_2O_4$ / Fe_3O_4 layered structure as observed for thick oxides, and instead consist of a single Mn-rich layer (possibly $MnCr_2O_4$). Magnetite and chromite phases are predicted to have slightly different fracture toughness values [78], which may further impact the observed increase in plastic deformation without fracture of thin oxides.

4.6.1.2. Mechanical Behaviors of Oxides produced on Titanium

Multiple oxide coatings were fabricated on commercial purity Grade II titanium (henceforth Ti) substrates by rastering a 120 ns pulsed laser beam across polished surfaces in ambient atmospheric conditions. This involved the aforementioned Er-doped, glass-fiber laser from SPI Lasers, Inc. operated at 5.6 W average power. A laser pulse frequency of 225 kHz was employed, and the focused laser beam was approximately Gaussian shaped with a $1/e^2$ width of 59 μm. Multiple overlapped laser scans created 4 x 4 mm areas for testing. Four laser scan rates, 130 mm/s 140 mm/s, 150 mm/s, and 160 mm/s, were chosen and hatch (centroid-to-centroid spacing)

was 10 μm. Faster laser scan rates correspond with lower laser fluences. First order estimates of power dissipation suggest the sample temperature does rise above the β-transus.

The resulting oxide phase was determined using grazing incidence X-ray diffraction (GIXRD) in a PanAnalytical Empyrean diffractometer with a Cu Kα source having a wavelength of 0.15418 nm. The microstructure and morphology of the laser oxides were then characterized using scanning electron microscopy (SEM), performed with a JEOL JSM-840A scanning electron microscope, transmission electron microscopy (TEM) using a FEI Titan G2 8200 aberration-corrected transmission electron microscope and AFM using a Bruker Multimode.

Nanoindentation measurements to determine mechanical properties were carried out with a Nanoindenter XP with a dynamic contact module (DCM) for low load testing, using both the quasistatic mode (QS) and the continuous stiffness module (CSM). A Berkovich probe with a radius of approximately 150 nm was used for mechanical property testing. Fracture behavior of the oxides was also examined with nanoindentation; a 90^{o} conical indenter tip with a nominal radius of 1μm was pressed in to the surface using the XP module with peak loads of 20 mN, 35 mN, 50 mN, and 80 mN. Indents were then imaged with a FEI Sirion FEG/SFEG scanning electron microscope and image-processing software was used to determine crack circumferences. Additionally, electrically conducting nanoindentation was employed to evaluate the electro-mechanical properties of the films, including the conductance and current-voltage (I-V) characteristics using a Hysitron Triboindenter 950 with electrical contact resistance (ECR) measurement capability and a boron-doped diamond Berkovich indenter. Electrical data was collected in voltage-source mode during the 10 mN hold segment of the loading cycle. Sweeps were 2s long and were directed from -10 V to +10 V.

The oxide layers fabricated in this study were on ~ 200 nm thick. In comparison, the thickness of a typical native oxide film on Ti is generally on the order of 2-3 nm [79] while electrochemically grown oxides range from 10s to 100s of nm [80]. Though the oxides produced by laser irradiation are relatively thick, in comparison to the bulk substrate thickness they make up only a small fraction of the total sample. Therefore, GIXRD was used for film analysis, revealing that the oxides include TiO and Ti_6O (Fig. 55a).

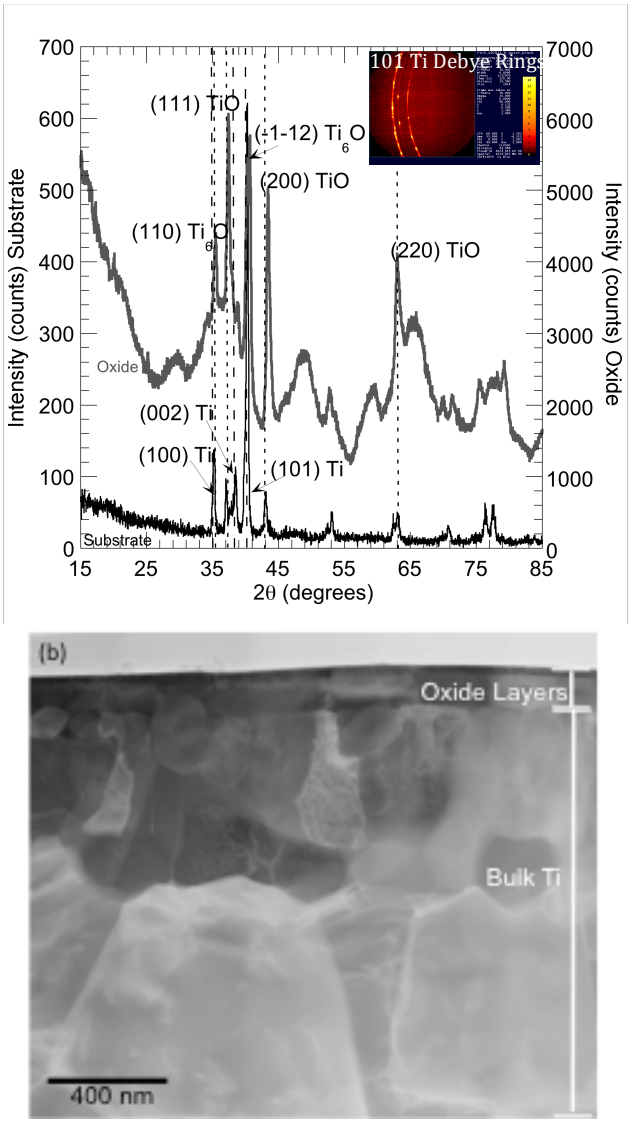

Figure 55. (a) GIXRD pattern of a representative Ti oxide produced using 225 kHz and a pattern obtained from a bare Ti substrate. Peak identification indicates the predominant oxides in the laser treated sample are TiO and Ti_6O. (b) Cross section TEM image showing oxide layers (TiO over Ti_6O) atop bulk Ti.

TiO has a face centered cubic structure and a lattice parameter of approximately 0.417 nm. GIXRD and TEM analysis also identified the presence of a Ti_6O interfacial layer, which is essentially intercalated oxygen in the HCP α-Ti substrate. Discontinuous Debye rings observed in an area detector image imply that the Ti substrate has a coarse grained microstructure. This structure was verified by TEM (Fig. 55b). Conversely, the oxide film has a very fine grained structure; the oxide grain size, *D,* can be estimated using the Scherrer equation [81.82]:

$$D = \frac{0.9\lambda}{(\delta 2\theta)cos\theta}\ , \qquad \text{Eq. 7}$$

where λ is the incident wavelength in nm, $\delta 2\theta$ is the full-width at half-maximum (FWHM) of the diffraction peak, and θ is the Bragg angle. The values are corrected for instrumental broadening by comparison with a standard cubic-TiO powder diffraction pattern. The true peak broadening is obtained from the following equation:

$$c = (b^2 - a^2)^{1/2}, \qquad \text{Eq. 8}$$

where *c* is the true peak broadening, *b* is FWHM of experimental spectra, and *a* is the FWHM for a profile from the same reflection from a standard TiO powder sample [83]. Realizing that Eq. (7) does not take in to account microstrain effects, and may thus underestimate the grain size, the grain size of the oxide is on the order of 5-11 nm. The calculation supports the proposition that the fabricated oxides are nanocrystalline.

The oxides have a topography consisting of a series of ridges and valleys. Fig. 56 shows an AFM image and section analysis (a) and an SEM micrograph (b) of the surface of an oxide. A collection of interconnected cracks, resulting in the formation of islands of oxide, covers the surface. The pervasive mudflat cracking indicates the oxides are stress-relieved; residual stresses that developed during fabrication, likely due to differences in thermal expansion coefficients between oxide and substrate, have been relieved through cracking. The average island diameter, or crack spacing, determined from line averages of SEM images similar to that shown in Fig. 56b, for all four oxides is 5.6 ± 0.48 μm.

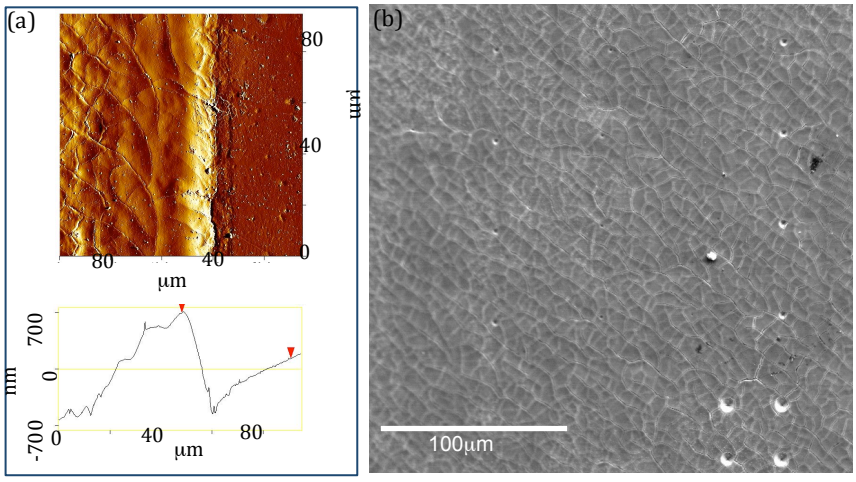

Figure 56. (a) AFM image showing edge of oxide pattern with bare substrate on right. (b) SEM micrograph showing pervasive mudflate cracking in an oxide layer made on Ti.

Dynamic nanoindentation was performed using the CSM technique. For this experiment, the CSM tests were performed at a frequency target of 75Hz and a depth target of 1 nm with a 350nm limit, producing modulus, hardness, and stiffness values. Table 7 summarizes the average modulus and hardness values obtained in the range of $0.5 < a_c/h < 1.0$ where a_c is the contact radius and h is the film thickness. Contact radius is calculated as listed before in Equation 4 where A is the contact area, determined Equation 5 and E_r, is computed with Equation 6.

In this, v is Poisson's ratio of the sample (0.3), v_i is Poisson's ratio of the indenter (0.07), E is the modulus of the sample, taken directly from continuous stiffness measurement, and E_i, is the modulus of the indenter (1141 GPa). In the chosen a_c/t range, the indentation depth is sufficient to overcome surface asperity effects, but shallow enough to avoid the influence of the more compliant substrate. The moduli reported in Table 7 are sample modulus values.

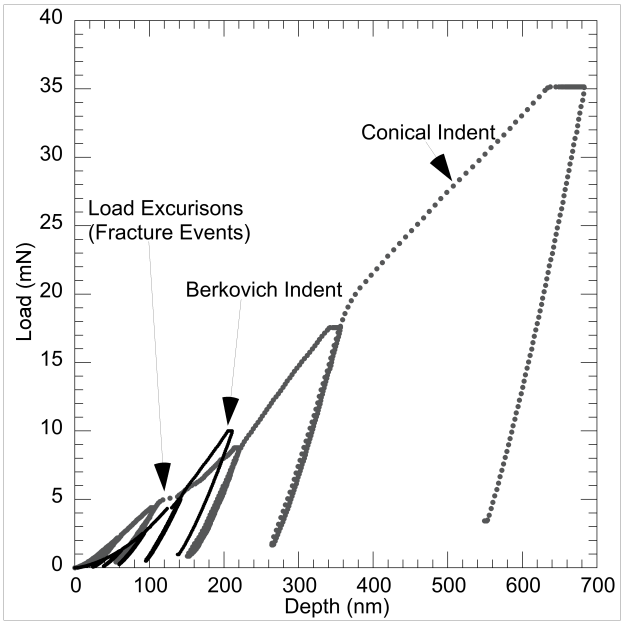

Figure 57. Example load-depth curves generated from Berkovich indentation (for mechanical property characterization) and conical indentation (for fracture behavior study).

Load-displacement data from quasi-static indentation are shown in Fig. 57, performed in load control with a Berkovich indenter. Load excursion events, that is, a sudden increase in depth with no increase in load, which are a result of oxide fracture, were evaluated to gain an understanding of the relative strengths of the oxides. The excursion load increases with increasing laser scan rate (Fig. 58). The minimum critical load to initiate fracture is highly dependent on scan

rate, while the maximum excursion load is less dependent on processing. The observation of excursion events at relatively low loads indicated that a fracture study could be successfully performed at higher loads with a tip of self-similar geometry.

The presence of mudflat cracking and the observation of fracture-related excursion events indicate that direct calculation of film fracture toughness and residual stress, which caused the mudflat cracking, is viable. Pervasive mudflat cracking denotes that the oxide film was once under a significant stress, which has been dissipated via cracking, thus the film as-tested is assumed to be in a stress relieved state. Then, if it is possible to calculate the fracture toughness from the stress-relieved film, that value can be combined with measured mechanical properties to calculate the stress required to initiate and propagate the observed fracture pattern, that is, the residual film stress that was present during growth and processing. This implicitly assumes that the fracture behavior measured at room temperature is similar to that when the films undergo mudflat cracking, which may be at an elevated temperature.

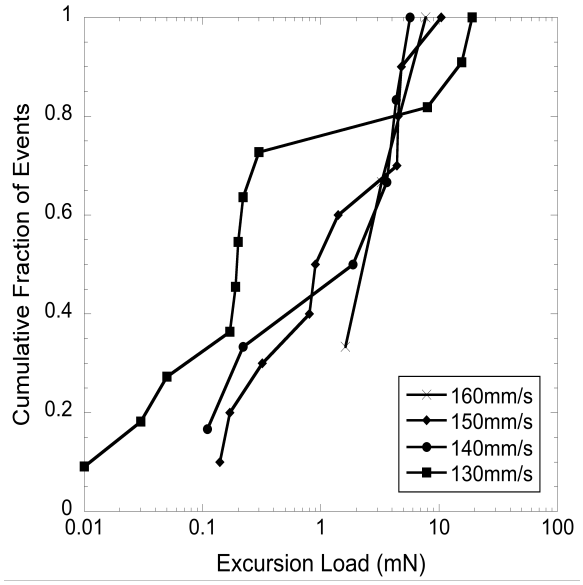

Figure 58. Cumulative distribution of load at discrete events, resulting from Berkovich indentation. Laser scan speeds used during oxide growth are listed in the legend.

Table 7. Modulus and hardness of titanium oxides tabulated as a function of laser scan rate.

Scan Rate (mm/s)	*Modulus (GPa)*	*Hardness (GPa)*
130	217±12	16.4±0.50
140	215±25	15.4±0.95
150	214±10	15.1±2.2
160	213±9	19.0±1.9

In order to investigate the fracture behavior of pulsed laser oxides, the films were indented with a conical tip of radius ~1 μm to maximum loads of 20 mN, 35 mN, 50 mN, and 80 mN. Load excursions in the load-displacement data indicated the initiation of an oxide fracture event. Cracked areas were measured using image analysis software and compared with contact areas calculated from load-displacement data. The outermost circumferential cracks correspond with the circumference of the calculated plastic zone for indents at all four loads. The plastic zone is calculated as [84]:

$$c = \sqrt{\frac{3P_c}{2\pi\sigma_y}}, \qquad \text{Eq. 9}$$

where P_c is the critical fracture load, that is, the load at the initiation of an excursion event, and σ_y is the yield strength of the oxide, which is estimated from hardness, *H,* using Tabor's relation [85]:

$$\sigma_y = \frac{H}{3} \quad .$$ Eq. 10

Figure 59 shows a series of SEM micrographs of indents at various loads with obvious circumferential cracking. The contact areas at pop in are typically much smaller than the outermost circumferential crack contact area. However, when inner circumferential cracks are observed, the contact areas measured for these cracks correlate well with pop-in contact areas.

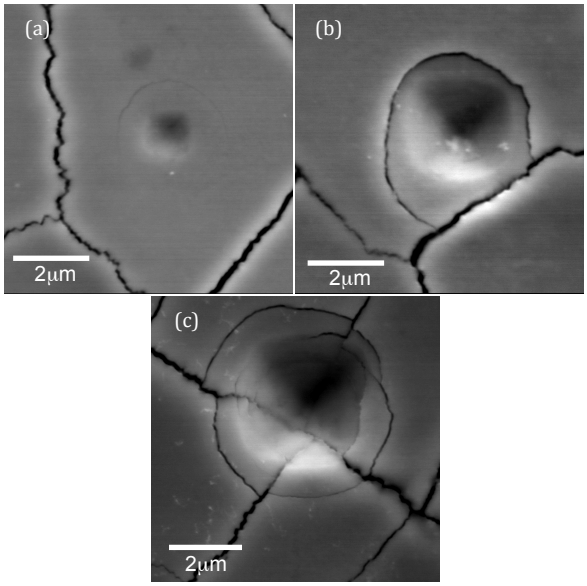

Figure 59. Micrographs showing typical oxide fracture morphology and circumferential cracking at the plastic zone radius of the indent. (a) shows a complete circumferential crack surrounding a 20 mN indent. (b) shows a crack with a 50 mN indent. Area in (c) involved a 80 mN indent.

The cumulative distribution of fracture loads with the conical indenter tip is shown in Fig. 60. The critical load required to cause fracture is a function of processing parameters: faster laser scan rates require a higher applied load to cause through-thickness fracture. Similarly, faster laser scan rates have higher maximum fracture loads than their slower counterparts. A comparison on

the previous figures gives insight into the mechanisms responsible for initiating fracture. If the observed indentation fracture initiated at the pre-existing mudflat cracks then low loads would be more similar for the conical indents, which have a much larger sampling volume than Berkovich indents. However, conical indentation produced pristine indents, regardless of proximity to a mudflat crack; indentation fracture is not determined by the existence of mudflat cracks. Variation in fracture load, then, is likely tied to the existence of another kind of defect.

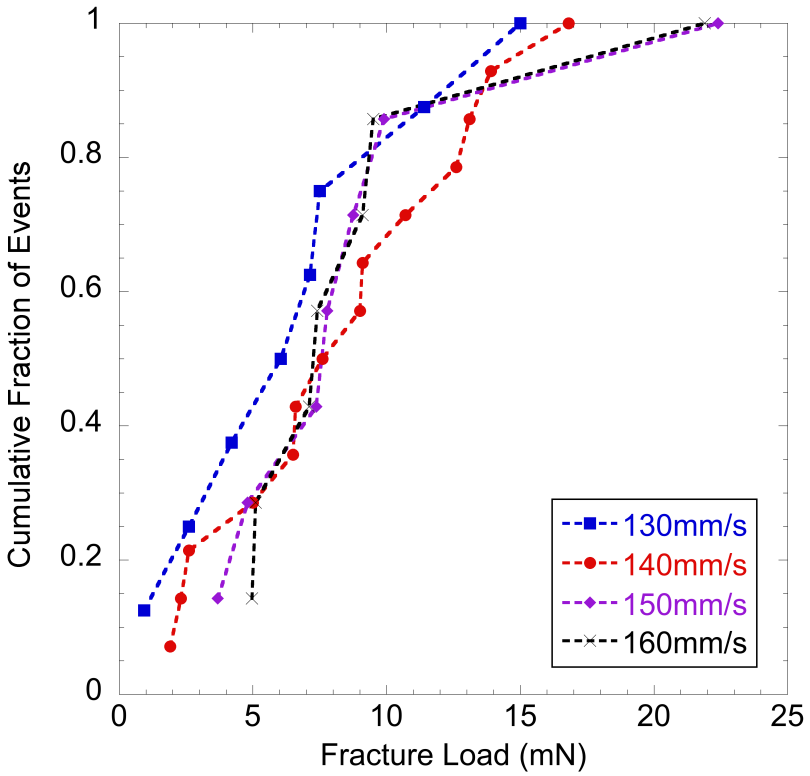

Figure 60. Cumulative distribution plot of fracture load, determined from excursions in conical tip load-depth data. Rates listed in the legend are the scan speeds used during laser-stimulated oxidation.

Since load at fracture can be used to calculate fracture toughness, Fig. 60 indicates there should be a correlation between processing parameters and fracture toughness. An energy method [86] was employed to quantify the fracture toughness of the oxides. Through-thickness cracks likely occur at the elastic-plastic boundary of the substrate [87], thus the film shrouding the plastic

zone must deform to accommodate the indentation. Fig. 61 is a schematic of the development of a through-thickness crack during indentation using a sphero-conical tip.

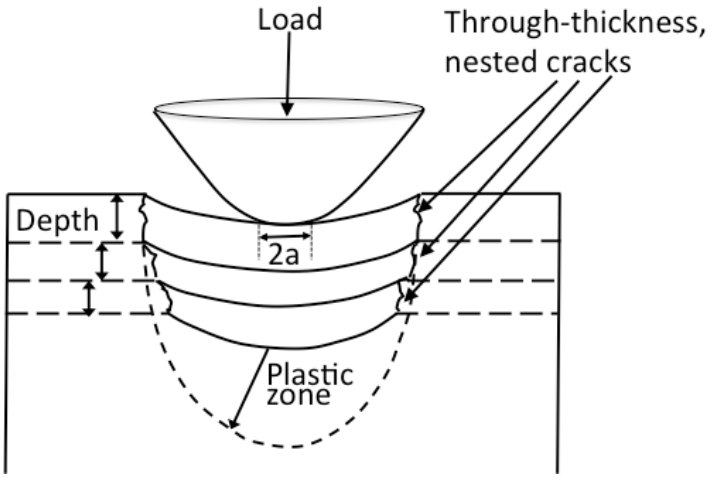

Figure 61. Schematic of through-thickness, nested cracks generated from high load nanoindentation

In addition to the size of the plastic zone, the energy required for deformation and film fracture is necessary to compute fracture toughness. Integration of the experimental load-displacement curves produced during indentation of the oxide film, until the onset of an excursion event, yield the total system energy, U_{system}:

$$U = \int_0^{\delta} P d\delta \quad . \qquad \text{Eq. 10}$$

The total energy of the system is the superposition of the energy required to both fracture the film as well as plastically deform the substrate. Integrating the load-displacement curves produced during conical indentation of the substrate alone result in the energy required to deform the

substrate, $U_{substrate}$. The integration is performed only up to the same depth as the critical fracture depth of the oxide to account for plasticity in the substrate during indentation of the oxide-substrate system, and is not the entire work of indentation for the entire load-depth curves shown in Figure 57 or the resulting indentation impressions in Figure 59. The amount of energy needed to fracture the film, U_{film}, can then be determined by subtracting the energy to plastically deform the substrate from the total system energy at the same depth:

$$U_{film} = U_{system} - U_{substrate}. \quad \text{Eq. 11}$$

The calculated film fracture energies are given in Table 8. The energy is dependent on the area produced from the initiation and propagation of a crack. It takes a critical amount of energy to produce the surface area of a new crack, which is the circumference of the crack multiplied by the film thickness. Assuming the majority of the energy goes into propagating the crack, and normalizing energy by the crack area results in the crack extension force, G:

$$G = \frac{U_{film}}{4\pi ch}, \quad \text{Eq. 12}$$

where c is the plastic zone radius and h is the oxide film thickness. The crack extension force is modeled for a constant load fracture condition, assuming all strain energy is released during fracture. The denominator is doubled because two new surfaces are created during crack extension. Calculated crack extension forces are shown in Table 8.

Table 8. Oxide thickness, h, fracture energy of the film, U_{film}, crack extension force, G, stress intensity parameter, K, and residual stress, σ_o, of oxide films grown using different laser scan rates. Calculated values are averages of multiple indents. Film thickness is combined TiO_2 + TiO.

Scan Rate (mm/s)	*h (nm)*	*U_{film} (pJ)*	*G (J/m^2)*	*K (MPa√m)*	*σ_o (GPa)*
130	153	255	35.8	3.57	10.3±1.9
140	140	204	35.7	2.77	8.88±1.6
150	135	94	33.7	2.58	6.73±1.1
160	125	153	33.5	2.49	7.46±2.2

Fracture criteria can be grouped in to two categories: energy methods and stress intensity methods. The two methods can be correlated by assuming the thin film is in a state of a plane strain; thus:

$$K = \sqrt{GE} \qquad \text{Eq. 13}$$

where E is the plain strain elastic modulus of the film and K is the stress intensity factor. Calculated values of K are collected in Table 8 as a function of scan rate. Contrary to the qualitative graphical analysis of fracture load, in general, the critical stress intensity decreases with increasing laser scan rate (decreasing laser fluence) and the calculated extension force and toughness values are similar to those calculated for titanium oxides in other studies [86,88,89]. This energy based fracture criterion analysis indicates that indentation induced film fracture can be evaluated successfully for a system with an extensively pre-cracked film on a more compliant substrate. Additionally, while the statistics of load at fracture may be used to qualify the strength

of a film, it may not be a good indication of the quantitative fracture toughness trend, thus a fracture mechanics calculation should be performed.

The energy-based analysis of thin film fracture is then used as an element in determining the residual stress of the oxide. Thouless [90] presented a comprehensive evaluation of the development and relaxation of stresses in thin films and through evaluating cracking as a method of stress relief developed a model relating film thickness, strain, and crack spacing. In the current study, the film thickness, h, and crack spacing, S, are measured, while the fracture toughness, K, is calculated. The strain in the film which results in mudflat or other regular cracking arrays, ε_o, is:

$$\varepsilon_0 = \sqrt{\frac{K_f\left(1-\nu_f\right)}{\left(1+\nu_f\right)E_f h\left(\frac{S}{5.6h}\right)^2}} \qquad \text{Eq. 14}$$

where E_f is the elastic modulus of the film and ν_f is Poisson's ratio of the film, in this case assumed to be 0.3. There are stress and strain discontinuities across the interface from the extrinsic film stress. We assume the coefficients of thermal expansion mismatch and modulus of the substrate and film are isotropic so that biaxial stress conditions apply. In this case, the residual stress, σ_o, can be determined from:

$$\sigma_0 = \frac{E_f \varepsilon_0}{1-\nu_f} \quad . \qquad \text{Eq. 15}$$

Residual stresses formed during growth for each film are compiled in table 2. In general, residual stress decreases with increasing laser scan rate (decreasing laser fluence). Oxides produced at

faster laser scan rates likely have a higher concentration of point defects created from fast growth rates, which may decrease the residual stresses imparted during formation. The residual stresses are somewhat larger than values reported for thin films deposited with other techniques, many of which result in compressive stresses [91,92]. In this technique, tensile stresses were generated, which are relieved via mudflat cracking, suggesting this growth method differs from others reported, resulting in variations in residual stresses. However, oxide films can withstand very high residual stress and due to the film thickness, mismatch between thermal expansion coefficients and the speed of fabrication, the values are not unreasonable. Similarly high values have been observed with TiN films deposited via pulsed laser deposition [93]. It is important to note that this technique for calculating residual stress was chosen because of the unique processing conditions as well as the singular films that are produced. The harsh fabrication environment and thick substrate preclude the use of wafer curvature methods for determining residual stress. Another common procedure for ascertaining residual film stress involves XRD; however this routine is not straightforward in this case because the films have a complex, non-stoichiometric phase. As residual stresses in other systems can impact film reliability, a method that allows quantifying residual stress in these types of systems should be useful in future processing-structure-properties relationships for this class of materials.

Conducting nanoindentation involves pressing a conductive (boron-doped) diamond Berkovich indenter into a sample at a constant load/unload rate while applying a voltage and monitoring the resulting current flow through the sample/indenter to determine current-voltage characteristics [94]. Current-voltage measurements are obtained from the hold segment of a 10 mN indent. Figure 62 presents the I-V data normalized by oxide thickness As shown in Fig. 62 faster

laser scan rates create more conductive oxides. Conductance is not dependent on oxide thickness, therefore another aspect of oxide structure must control the observed electrical response.

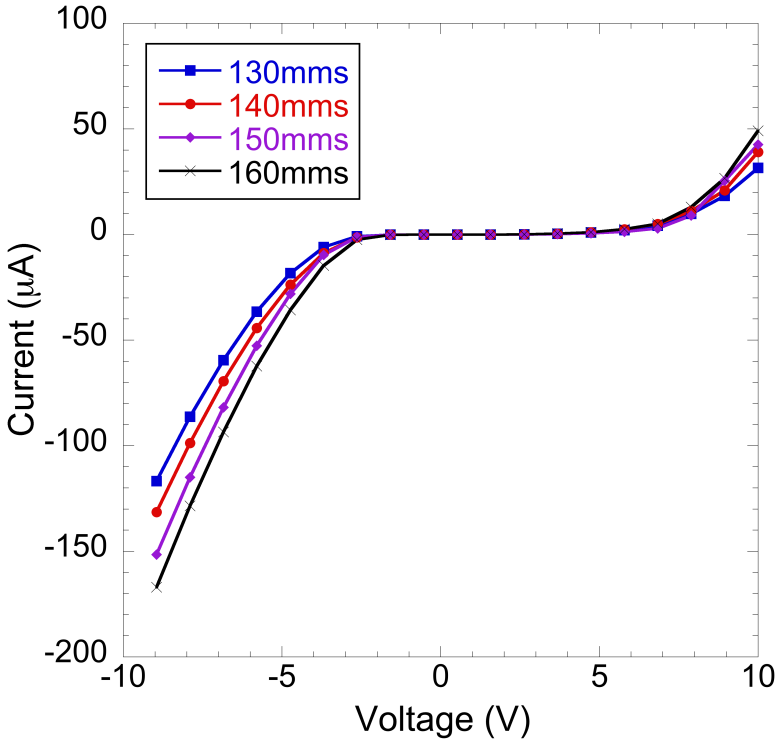

Figure 62. I-V sweeps normalized by oxide thickness produced with conducting indentation, at constant load, demonstrate that oxides produced with reduced F_{acc} maintain higher conductance.

Furthermore, the asymmetry of the I-V sweeps about zero suggest the formation of Schottky barrier due to unequal amounts of holes and electrons (the charge carriers) in the oxide. This correlation may indicate that defects, such as vacancies, in the oxide are the source of the increased conductance. The pure FCC phase of TiO is metastable and non-stoichiometric with a distorted NaCl structure resulting in vacancies in both the cation and anion partial lattices. Up to 15% of both Ti and O sites are vacant [95]. Based on mechanical properties and fracture behavior,

faster laser scan rates are predicted to contain a higher concentration of defects. Increased current flow may also result from a higher vacancy concentration, which increases with increasing O:Ti ratios, or other defects associated with fast deposition rates. Conductivity, σ_i, is related to concentration of carriers by [96]:

$$\sigma_i = \frac{c_i z_i^2 e^2}{kT} D_r, \qquad \text{Eq. 16}$$

where c_i is the concentration of carriers, in this case vacancies, z_i is the valence, e is the charge on an electron, k is Boltzman's constant, T is the absolute temperature, and D_r is the random diffusion coefficient. By assuming z_i, e, k, T, and D_r remain constant for all four oxides, a qualitative comparison can be made between concentration and conductivity. Concentration is proportional to conductivity, thus, as conductivity, or in the case of this study, conductance, increases, the concentration of vacancies increases. Unlike previous experiments with laser-fabricated oxides on stainless steel substrates [97], there is no distinct correlation between oxide fracture load or stress intensity parameter and measured maximum current. Since conductance is related to carrier concentration, this analysis indicates that the defect structure of an oxide, in particular the vacancy concentration, which is dependent on laser processing parameters, may play an important role in the electromechanical properties of the film.

4.6.2. Electrochemical Response

Various laser-fabricated oxide layers have been evaluated for their corrosion resistance. This includes oxide layers produced on stainless 304L. Tests include extreme corrosion environments involving continual immersion in concentrated salt water. Immersion testing in a simulated seawater solution and salt spray testing were selected to qualitatively capture the performance of the oxide-tagged stainless steel under marine-type conditions. Although these markings are not likely to be used in salt water environment applications, this first test was completed to take a first look at corrosive behavior and can be considered a worst case test.

In addition, samples were subjected to less harsh corrosion environments involving salt spray / salt fog in accordance with the ASTM B117 standard. The effects of corrosion in these tests were evaluated by mass change and changes to surface color, phase, and chemistry. Anodic polarization was further employed to gain quantitative insight into the localized corrosion behavior of the oxide-substrate system in a chloride-rich environment. Degradation of the system under the exposure conditions will be interpreted in terms of previous studies of the phase, structure, deformation, and fracture of these film systems.

Salt Water Immersion Tests

The first oxide samples, used for immersion testing, were fabricated on to a single SS 304L substrate; a schematic of this sample configuration is shown in Figure 63. Average laser power (5.6 W) and pulse frequency (225 kHz) remained constant, while laser scan speed varied for each oxide square. Each oxide square had an area 4 mm x 4 mm. Scan rates were 30, 47, 80 and 175 mm/s. See Table 9 for details.

Immersion testing was conducted by submerging the quad-oxide sample in a simulated seawater solution (pH 6) per the ASTM G31 standard for 25 days. Exposed SS 304L substrate was enameled prior to immersion to ensure that only the laser modified oxide surfaces were exposed to the environment. At the conclusion of the exposure period, the sample was removed, rinsed with deionized water, and dried for 24 hours prior to microscopy.

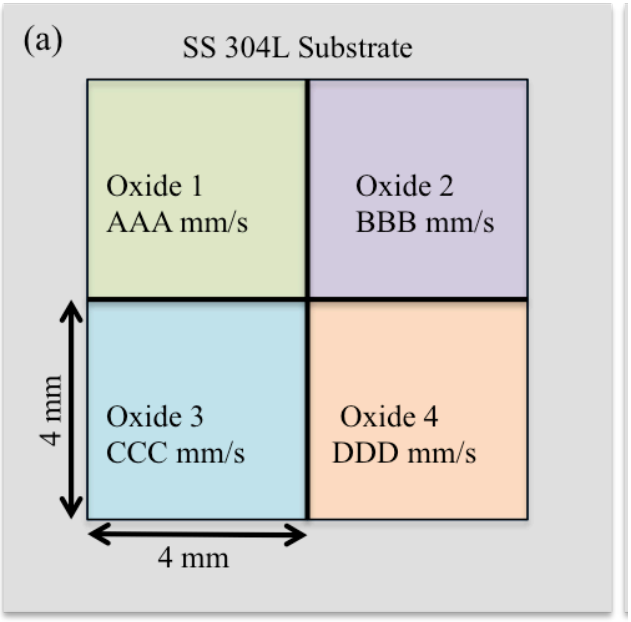

Figure 63. Schematic illustration of laser-fabricated oxide sample configuration for immersion testing.

Table 9. Processing conditions and resulting film thicknesses for salt water immersion tests. All oxides fabricated at an average laser power of 5.6 W.

Immersion Test Samples	
Laser Scan Rate (mm/s)	*Thickness (nm)*
30	489
47	405
80	403
175	302

After 25 days exposure in 5% NaCl solution (simulated salt water), a thick corrosion product covered all oxide areas. Optical micrographs obtained before and after exposure are presented in Figure 64. The corrosion product deposited on top of the laser-oxide areas; the laser-fabricated oxide is clearly visible in the SEM image of a post-exposure FIB cross-section (Figure 65a). The corrosion product was not well adhered to the oxide tag, flaking off easily when imaged with a high energy electron beam or after cleaning with oxalic acid, revealing the laser-fabricated oxide still present on the metal surface. These results suggest that the corrosion product develops primarily from corrosion of the underlying steel substrate, rather than severe dissolution of the laser-oxide coating.

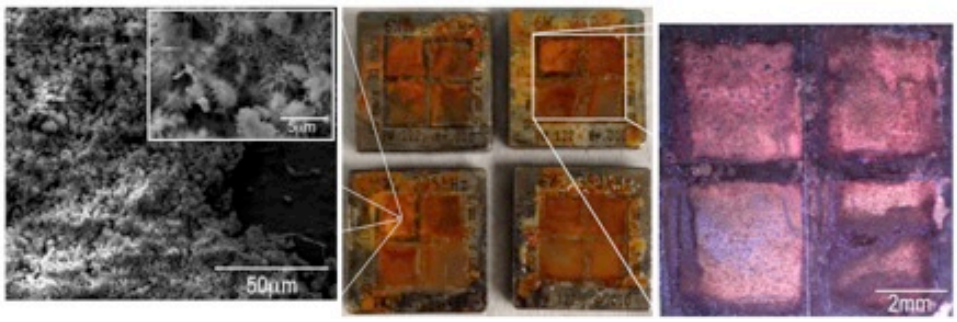

Figure 64. Post immersion SEM image (left) and optical image (middle) of corrosion product. Additional image on right is an optical micrograph that shows corrosion product partially detached from substrate.

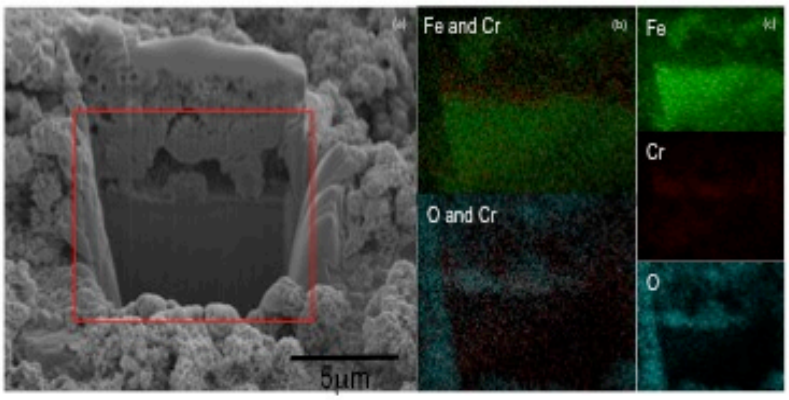

Figure 65. FIB cross sectioned area on left (a) and EDS mapped regions on right (b) showing location of Fe, Cr, and O.

Subsequent post-mortem cross-sectional EDS provides a qualitative description of composition as a function of depth. EDS mapping (Figure 65b) detects a difference in Cr, Fe, and O content throughout the substrate and into the laser-oxide and corrosion product; linear point profiling of an as-received oxide mounted in cross-section confirms EDS mapping and shows a decreasing Cr concentration moving from the bulk substrate towards the oxide interface. The results are in agreement with previous characterization which revealed that Cr is depleted from the substrate to a maximum depth of ~2 μm for the case of a 5.6 W, 225 kHz oxide (depletion depth varies with oxide thickness). Because stainless steel derives its corrosion resistance from the formation of a continuous Cr_2O_3 layer when Cr is dispersed throughout the matrix at a concentration of greater than approximately 12%, depletion of solute Cr below this critical concentration leads to decreased corrosion resistance [98,99]. Thus, the deposition of a corrosion product on top of the laser-oxides suggests that enough Cr is depleted from the substrate melt-zone during laser processing to reduce the Cr concentration below ~12 wt. % making the SS 304L susceptible to chloride attack [100].

The observed extensive corrosion of the laser-modified stainless steel system is consistent with observations that oxides fabricated on SS 304L via certain laser irradiation parameters are non-protective. Heterogeneities, such as cracks formed as a means to relax residual tensile stress in the oxide films hinder the ability of the oxide to function as a barrier for the underlying substrate metal. Because all visible substrate is enameled prior to immersion, the pre-existing surface cracks that pervade the oxide area provide the only path for exposure of the Cr-depleted substrate to the aggressive environment. As described earlier, the degree of oxide channel cracking depends on coating thickness, thus it is likely that susceptibility to corrosive attack also depends on oxide thickness and Cr-depletion depth in the substrate.

Characterization of these samples and others subjected to salt spray conditions demonstrated that oxides with thicknesses greater than ~200 nm suffer from pervasive through-thickness cracking, which develops as a means to relieve residual stresses in the film resulting from high temperature laser processing and thermal expansion coefficient differences between the substrate and coating. However, oxides with smaller layer thickness exhibit improved electrochemical resistance.

Salt Spray Testing

Salt spray testing was then conducted on 12 individual oxide samples made using the laser process parameters specified in Table 10. A polished blank SS 304L specimen was included in the test matrix as a control sample. All stainless steel substrates were enameled to ensure that only oxide areas were exposed to the salt fog environment. Salt spray exposure was performed in accordance with the ASTM B117 standard for 168 hours. Samples were rinsed and dried for at least 24 hours prior to microscopy.

Table 10. Processing conditions and resulting film thicknesses for salt spray/fog tests. All oxides fabricated at an average laser power of 5.6 W.

Laser Scan Rate (mm/s)	*Measured Coating Thickness (nm)*
30	489
47	405
80	403
175	302
200	285
225	196
250	150
300	147
350	100
400	84
450	65
500	40

An assessment of the severity of corrosion as a function of oxide thickness reveals that thick coatings (> 200 nm) are susceptible to chlorine attack while oxides of < 200 nm thickness are protective. Micrographs for four of the twelve oxides are presented in Fig. 65.

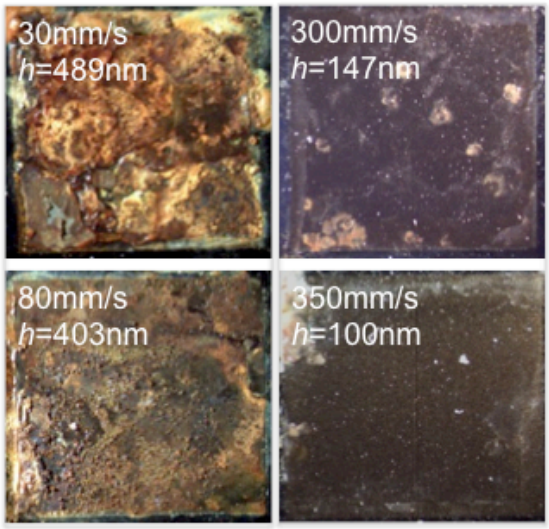

Figure 66. Optical micrographs of four oxide coatings subjected to 168 hours of salt spray exposure. Surface characterization indicates that oxides having a thickness (h) greater than approximately 200 nm are corroded. Coatings with thickness < 200 nm remain intact, to a large degree. This is evidenced with the two samples shown on the right by their original color and lack of corrosion product.

Characterization of these samples and others subjected to salt spray conditions demonstrated that oxides with thicknesses greater than ~200 nm suffer from pervasive through-thickness cracking, which develops as a means to relieve residual stresses in the film resulting from high temperature laser processing and thermal expansion coefficient differences between the substrate and coating. Through-thickness cracks provide a path for exposure of the substrate immediately beneath the oxide to the aggressive environment. The Cr-depleted SS 304L substrate is susceptible to chloride attack and thus a thick, uniform corrosion product deposits on top of the exposed area. Conversely, oxides with thickness less than ~200 nm have no visible surface channel cracking after laser fabrication, suggesting the films are thin enough to avoid significant residual stresses and thus deform in union with the stainless steel substrate. These thin oxides, with a likely mixture of $MnCr_2O_4$ and Fe_2O_3, serve as a protective barrier preventing corrosion of the Cr-depleted substrate near interfacial volume.

Anodic Polarization Test Results

Additional anodic polarization tests showed that multi-layered oxide coatings are susceptible to corrosion, but are still improved when compared to oxides made using a single laser pass process. In Figure 67 below, optical micrographs of samples subjected to anodic polarization tests are shown. These particular layers were made with our traditional single-pass approach and act as a baseline for comparison to oxides made with new processes. Images a-e show initial sample surfaces prior to testing, and images d-j show degradation of the same samples after testing, in which pitting has occurred. The oxide thickness (h) is specified in the figures along with the laser scan speed used to fabricate a given feature. The images on the right show degradation of the surface. Anodic polarization causes pitting and dissolution of the oxide film

and localized corrosion of the substrate. Stainless steel is known to be susceptible to pitting at low potentials in chloride containing solutions; thus there is some pitting even when using raw material. More extensive pitting is exhibited in these laser-treated (oxidized) samples.

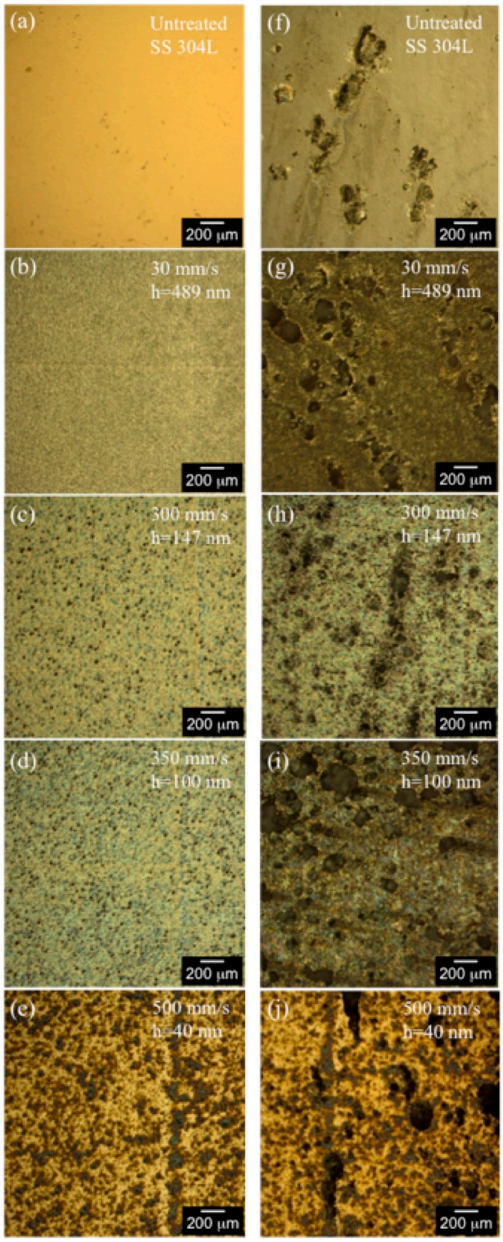

Figure 67. Optical micrographs showing samples subjected to anodic polarization tests. Images a-e show samples prior to testing. Images d-j show degradation after testing. The top two images are a control SS304L samples that was not laser color marked. Within the images (b-e, g-j), an oxide layer thickness is specified along with the associated laser scan speed where appropriate. All color layers shown here were made by a single laser pass process.

With Figure 68, we include the measured corrosion potential of two oxide samples along with the base metal (not treated by laser irradiation). These tests demonstrate that corrosion potential varies directly with oxide thickness; thicker oxides are the most susceptible to pitting corrosion. In light of post-mortem microscopy, the propensity to crack tracks with the prevalence of channel cracks. With the plot

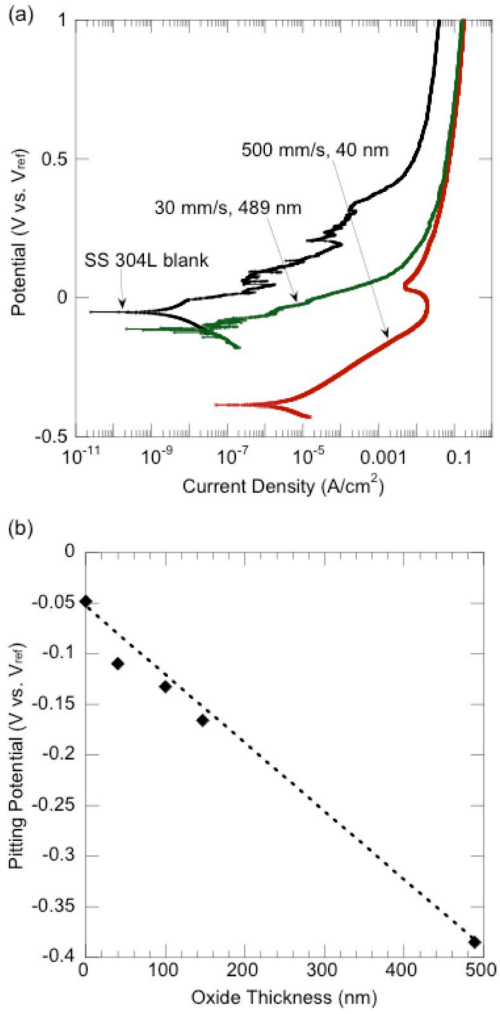

Figure 68. (a) Anodic polarization curves obtained from testing a SS304L control sample (not treated by laser irradiation) as well as two samples having laser grown oxide layers. Oxide layer thicknesses (489, 40 nm) and scan speeds are specified for the two laser color marked oxide layers. (b) Plot of corrosion potential as a function of measured oxide layer thickness.

in Figure 68(a), one sees that the 489 nm – thick oxide layer shows no passivation behavior, but instead begins to dissolve immediately after the corrosion potential is reached. The corrosion potential for this oxide shifts to a more cathodic value than that exhibited by the thinner oxides, consistent with a higher corrosion rate. It is likely that this particular sample has a larger Cr-denuded zone and channel cracks in the oxide all the electrolyte to penetrate exposing the Cr-depleted portions of the substrate.

Finally, it is found that oxide layers made with multiple, low energy laser passes are generally superior to those made with single passes. Examples of potentiodynamic-tested oxide films made by multi-pass laser scanning are shown in Figure 69. Images capture the films before and after testing; for brevity, only oxide layers grown using scan speeds of 475 mm/s and 550 m/s are included. In general, these oxides show no improvement in localized corrosion resistance compared with the untreated steel, as the corrosion potentials for all laser-treated samples are more cathodic than for bare SS304L. However,

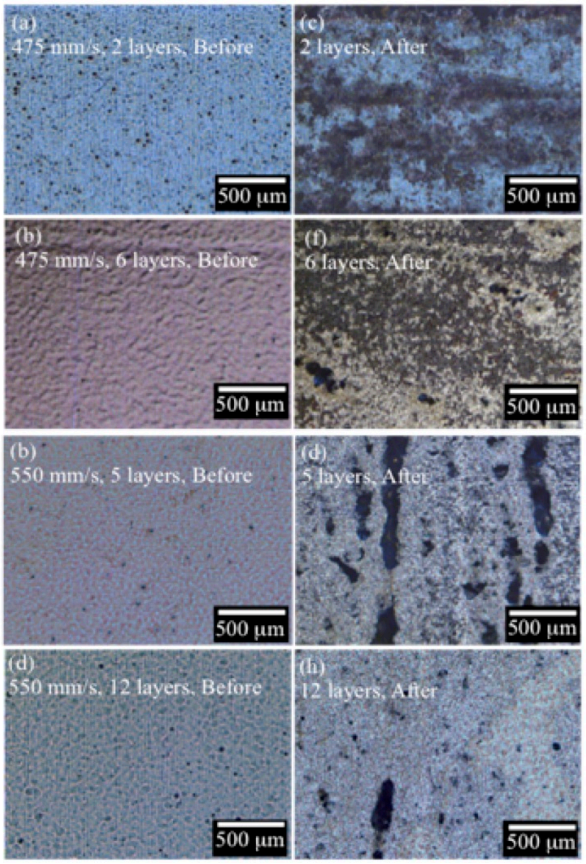

Figure 69. Optical micrographs subjected to anodic polarization tests. Images a-d show samples prior to tests. Images e-h show degradation after testing. Within images, the number of laser scans used to grow the feature and the scan speed are specified. Color oxides shown were made using multi-scan processes.

these particular laser-treated samples are less susceptible to localized corrosion attack compared with oxide layers made using a single-pas approach. Evidence for this is found in comparing the micrographs of Figs. 67 and 69. There are less number of pits per unit area in the oxide layers made with multiple passes.

Additionally, a more quantitative difference in susceptibility to localized corrosion comes from measured corrosion potentials. Compared to the corrosion potentials shown for single – pass fabricated oxide layers, the oxide layers constructed using multiple laser scan passes exhibit a

much smaller cathodic shift in potential. For example, the 100 nm oxide films made using multiple laser scan passes were measured to have a corrosion potential of -0.07 V vs. V_{ref}.

4.6.3. Aging

Markings created by nanosecond pulsed laser irradiation have been aged normally and through accelerated tests. 'Normal' aging refers to room temperature storage at low humidity levels (~15%) over several years time. Accelerated aging refers to short duration, elevated temperature exposures.

The specific objectives involved determining whether the chromaticity and hemispherical spectral reflectance of different oxide layers created on commercially pure Ti, stainless steel 304L and Ti alloy (Ti6Al4V) changed over time. Test samples included oxide layers created using a variety of different powers, laser scan speeds or, in other words, different accumulated laser fluence.

Room temperature aging of oxide layers made on stainless steel 304L, Ti, and Ti alloy over the course of two years did not result in a significant change in spectral reflectance. Samples have been re-characterized with the same, calibrated instrument (Cary 5000 UV-Vis-IR spectro-photomer) used to baseline samples. A plot of spectral reflectance for one sample is included in Fig. 70. The reflectances measured within one week of fabrication are shown in blue. These are compared with the reflectances measured from this same color layer after two years of normal aging. Within the visible, photopic part of the spectrum, there is minimal change in reflectance. To the eye of an observer, there is no detectable change.

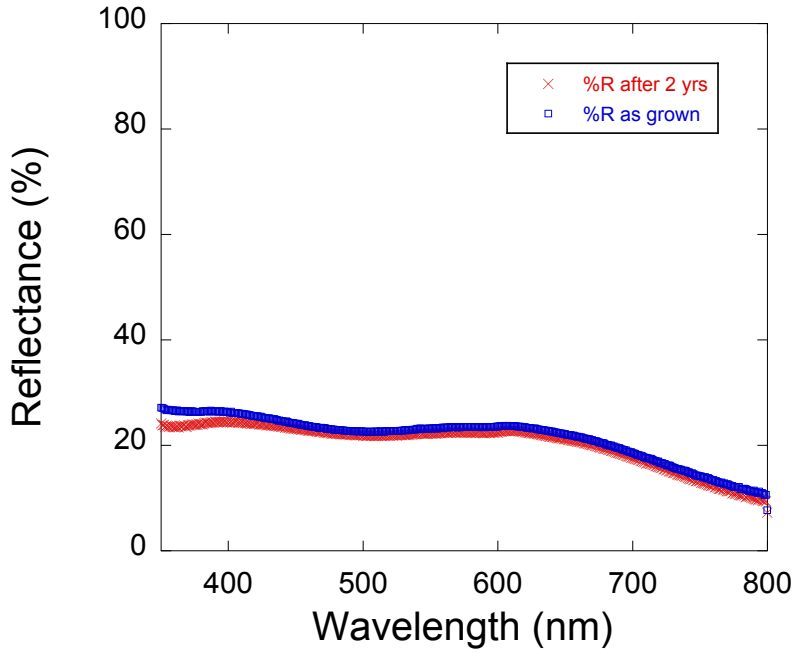

Figure 70. Plot of spectral reflectance for a single titanium oxide coating soon after its fabrication and two years post fabrication wherein it was aged at room temperature. Similar spectral reflectances are observed demonstrating excellent room temperature aging characteristics.

Detailed comparisons of chromaticity in normally aged samples have been made for a variety of oxide layers. As summarized in Table 11, there is no detectable change in chromaticity over the course of two years. This table summarizes the optical appearance of various oxide layers made on Ti samples. The net change in chromaticity (x, y) over this period of time is included in the last column of Table 11. These 'offsets' are mostly within the experimental uncertainty of the spectrophotometer determined to be $\pm$ 0.015. The same lack of change is highlighted in a chromaticity diagram (Fig. 71).

Table 11. Results from room temperature aging study of oxide layers made on Ti samples. Chromaticities (x and y) are included for 12 oxide layers demonstrating no detectable change after 2 years.

Sample ID	Power, Speed	Chromaticity as grown (x,y)	Chromaticity after aging 2 yrs (x,y)	Offset Δx, Δy
S070111-1	6.6 W, 90 mm/s	0.311, 0.323	0.311, 0.323	0.000, 0.000
S070111-1	6.6 W, 100 mm/s	0.287, 0.321	0.287, 0.319	0.000, -0.003
S070111-1	6.6 W, 110 mm/s	0.233, 0.27	0.26, 0.299	+0.027, -0.002
S070111-1	6.6 W, 120 mm/s	0.265, 0.305	0.259, 0,289	-0.006, -0.016
S070111-2	6.6 W, 130 mm/s	0.212, 0.231	0.211, 0.232	-0.001, -0.001
S070111-2	6.6 W, 140 mm/s	0.207, 0.203	0.201, 0198	-0.006, -0.005
S070111-2	6.6 W, 150 mm/s	0.227, 0.181	0.219, 0.176	-0.008, -0.005
S070111-2	6.6 W, 160 mm/s	0.287, 0.171	0.277, 0.181	-0.010, +0.010
S070111-3	6.6 W, 170 mm/s	0.405, 0.277	0.388, 0.256	-0.017, -0.019
S070111-3	6.6 W, 180 mm/s	0.418, 0.298	0.401, 0.275	-0.017, -0.022
S070111-3	6.6 W, 190 mm/s	0.457, 0.345	0.441, 0.322	-0.016, -0.023
S070111-3	6.6 W, 200 mm/s	0.502, 0.399	0.486, 0.381	-0.016, -0.018

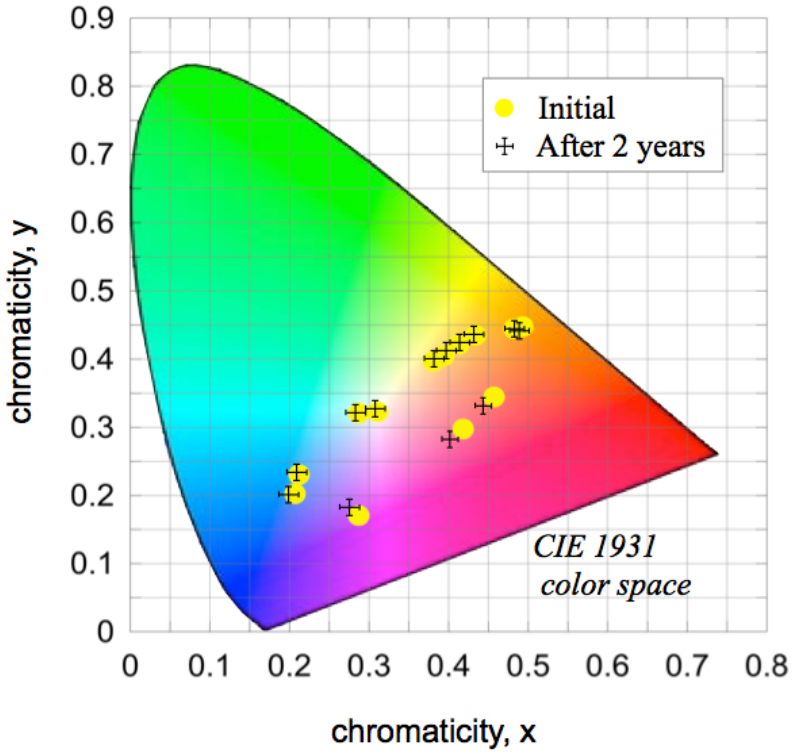

Figure 71. Chromaticity diagram showing minimal changes in optical properties of oxide layers made on Ti. Results are shown for chromaticity measured just after laser treatment and 2 years after fabrication.

Elevated temperature tests have been completed to gauge an onset reaction temperature for oxide layers made on stainless steel and those made on Ti alloy. Different oxide layers on Ti alloy were aged at 50, 100, 150, 200, 250, 300, 350, and 400 degrees C for 1 hr per temperature. Chromaticity was evaluated after cooling back down to room temperature.

The samples shown in Figure 72 were oxide layers used for high temperature testing. Four different oxide layers were made on each for redundancy. Tests show that the oxide layers on Ti alloy are stable up to temperatures ~ 250^{o}C, meaning there is no change in chromaticity until annealed at that temperature. An onset reaction temperature of 250^{o}C was consistently found for each of the color layers, as evidenced by a change in the general optical appearance and the chromaticity evaluated by the spectrophotometer (analysis at room temperature). This is indicated in Figure 73.

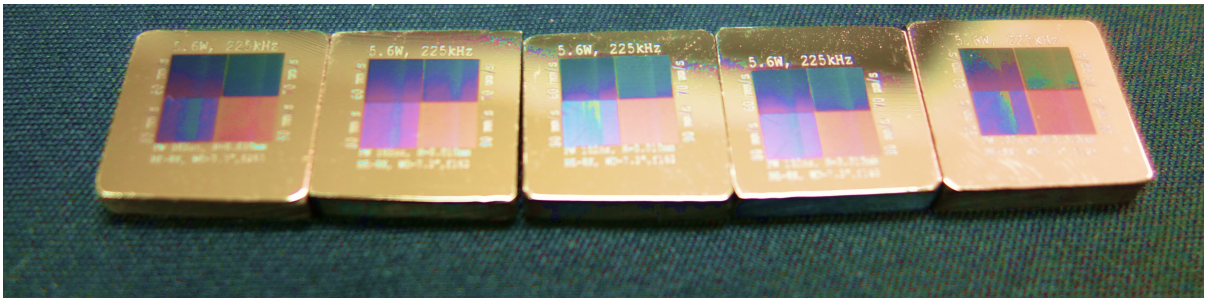

Figure 72. Samples used in accelerated aging studies. Oxide layers are adhered to Ti alloy substrates.

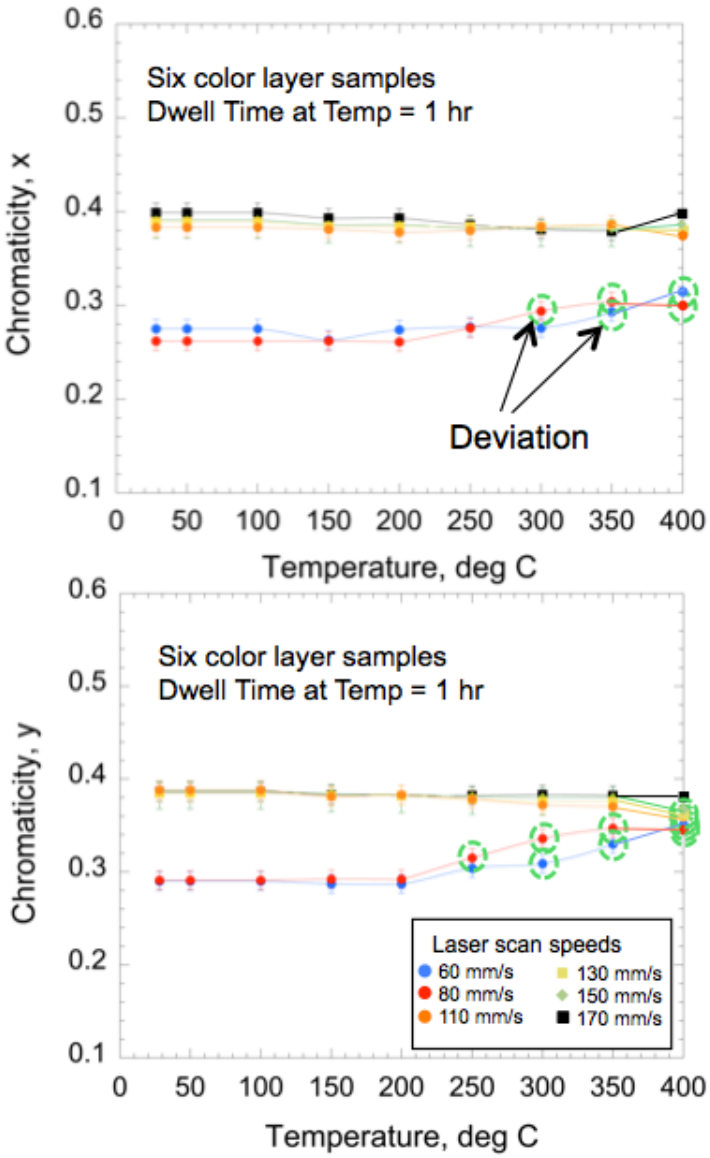

Figure 73. Results from elevated temperature tests of six samples. These plots indicate no change in chromaticity for elevated temperatures up to 250°C (tests for 1 hr. each). The x and y chromaticity are included in separate plots. The legend lists the laser scan speeds used for oxide layer fabrication along with P_{avg} = 5.6 W.

4.7. Method for Marking Non-Planar Surfaces

Working with Nutfield, Inc., we have inspired this company to expand their current product set to offer a different scan head that allows one to laser color mark much larger areas up to 1 m^2.

The instrument (referred to as the 3XB series) is a compact scanning solution that offers 3-axis capability at a cost comparable to 2-axis systems. This means the scan head provides a new capability to laser mark curved surfaces, such as a cylinder, sloped solid, etc. A photograph of this device is included in Fig. 74 below. It is installed in our laboratory and will be the centerpiece of future marking research.

Figure 74. Nutfield Technology's 3-Axis Contour designed for laser color marking large surface areas and shaped, nonplanar solids. Enclosure is approximately 30 x 30 x 70 cm.

5. LASER INDUCED PERIODIC SURFACE RIPPLE PATTERNS

5.1. Background

Periodic surface ripples formed by scanned, pulsed laser irradiation represent a second form of intrinsic marking that can be applied to virtually all solids. Much like laser color markings, ripple markings can contain programmed information as well as elements of randomness. Once cataloged, features can be used to assure the authenticity of critical assets and help protect against counterfeiting and substitution.

Formed by scanning an ultrashort-pulsed laser beam across a component's surface, periodic ripples generally develop as the beam encounters local maxima on a surface. A rough hill-and-valley surface, such as that produced from mechanical machining, provides ample sites for light scattering and interference, which underlies the formation of periodic morphologies near asperities. Alternatively, if a surface is initially polished, then a first laser pass can be used to roughen the surface so that a second pass generates ripples.

The characteristics of periodic ripple features that can be cataloged include amplitude and ripple wavelength. Additionally, the location of ripple patterns can also be recorded if forming sparsely across a surface.

5.2. Origin of Ripples and Time Scales for their Formation

Laser induced periodic surface structures (LIPSS) formation have been predicted for many different materials and pulse lengths, ranging from continuous wave to femtosecond pulsed laser irradiation. In general, LIPSS formation is the result of diffraction patterns first established on surfaces by light scattering from surface defects or engineered surface features. A spatially-modulated intensity distribution of light then leads to a corrugation of the surface.

When working with an atomically smooth surface, LIPSS usually form after irradiation by more than one laser pulse, because an initial pulse must induce surface roughness that is sufficient for light scattering [101,102]. On the other hand, optically rough surfaces scatter laser light beginning with the first pulse, as interference of scattered light with an incoming laser pulse leads to a periodic variation in the intensity of absorbed laser light at the material surface [101,103]. It has been further hypothesized that low-spatial frequency LIPSS (LSFL) formation occurs after surface melting[3,4]. Diffraction was employed after irradiation by a 20 ns pump pulse to show that LIPSS form several ns after irradiation of semiconducting surfaces [104]. Such studies are complicated, however, by the fact that LIPSS usually form after irradiation with multiple laser pulses; therefore, it is difficult to determine when LIPSS first appear on the surface. Also, LSFL typically have sub-micron periodicities, making pump-probe optical imaging difficult. As a result, the mechanisms of material movement, which lead to LSFL formation, are not well-established.

Recent studies provide evidence for how the electron sub-lattice of a target material can participate in the formation of LIPSS. Ultrafast laser irradiation of fused silica led to periodic ordering of excited conduction band electrons into a grating pattern. The authors suggest material is preferentially removed from local sites due to self-trapped excitons [105]. It is noted that this

behavior does not occur with semiconductors, and the material removal and ablation dynamics is quite different for semiconductors [106].

In this work, pump-probe microscopy is employed to observe LSFL formation on a Si surface after irradiation by two ultrafast laser pulses. Pump-probe studies of ultrafast pulsed light interactions with surfaces are simpler than long pump time experiments, since LIPSS form long after the laser pulse turns off [102,107]. Also, white light is used as probe light, allowing for enhanced lateral resolution. A similar approach has been used to observe crater formation on Si surfaces after irradiation by ultrafast laser light [108]. We will show, by repeating the same irradiation conditions and probing at different times after arrival of a pump pulse, LIPSS formation occurs after the onset of surface melting. Furthermore, LSFL appear on the Si surface on the same time-scales as material removal after irradiation. These results suggest that LSFL formation is the result of material removal from the Si surface.

A Clark-MXR CPA-2001 Ti:sapphire pulsed laser with a 150 fs pulse length, centered at a wavelength of 780 nm, with a repetition rate of 1 kHz, a maximum pulse energy of 1 mJ, and a Gaussian intensity profile, was split into two separate beams by a beamsplitter. One beam is employed as the "pump" beam and the other as the "probe" beam, which illuminates the material response initiated by the pump beam. Shown in Fig. 75, the pump beam is focused onto a Si substrate at a 45° angle using a 10 cm focal length lens. At normal incidence, the radius of the focused pump beam was measured with a DataRay Inc. WinCamD 14-bit beam profiling camera and was found to be 16 μm. The probe beam is focused into a beaker of water using a 5 cm focal length lens in order to generate white light [109]. This semi-coherent white light beam is temporally dispersive within the water and glass beaker, and it was estimated that the probe beam pulse length increases to ~ 4 ps after exiting the beaker. An InfiniTube™ in-line assembly reflects

the white light through a Mitutoyo 50X infinity-corrected objective with a numerical aperture of 0.55 and a working distance of 13 mm. The white light irradiates the sample, reflects from the sample, travels through a 20 cm focal length imaging lens, and is imaged by the CCD camera. Samples were affixed within the focus of both beams using a Newport 4-axis translation stage which allows for positioning in the x, y, z, and θ lab directions with 2 μm accuracy. Single laser pulses were isolated from the 1 kHz pulse train using a Thorlabs optical chopper and a Uniblitz mechanical shutter. All irradiation experiments were conducted in air.

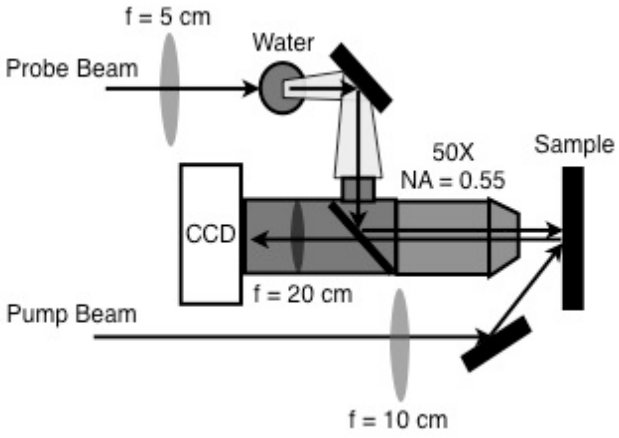

Figure 75. Pump-probe microscopy setup for imaging LIPSS formation at normal incidence. White light illumination is produced by nonlinear interactions of the probe beam with water. A 150 fs pulse broadens to 4 ps after traveling through the water. Arrows indicate the path of the white probe light as it illuminates the region of the sample irradiated with the pump beam. Pump beam irradiates the sample at a 45 degree angle with s-polarized light.

The sample position was varied near the focus of the microscope objective until circular, optical fringes surrounding the viewing plane were clearly visible using probe beam illumination, shown in Fig. 76(a). Nomarski contrast imaging of the crater was performed using a 40X objective and a commercially available microscope, Fig. 76(c). The resolution in Fig. 76(b) is comparable to a commercial, Nomarski contrast microscope and LIPSS are visible. If surface

features are imaged in the center of the imaging plane in Fig. 76(a), only crater edges are visible and sub-micron LIPSS cannot be imaged.

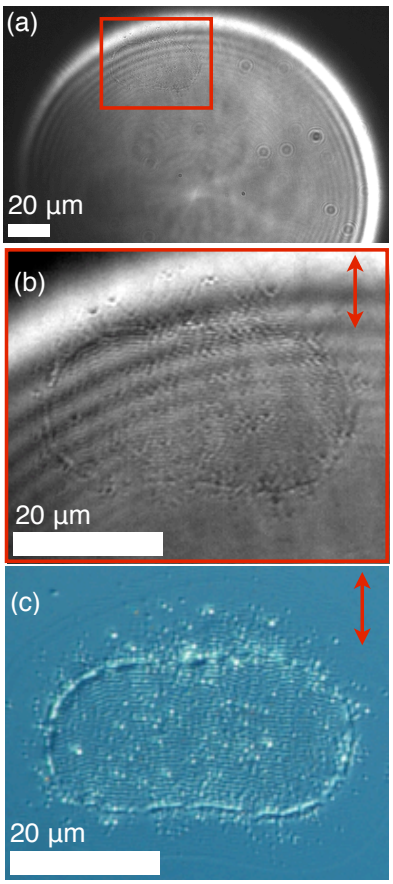

Figure 76. Images of a crater and LIPSS formed on a Si surface after irradiation of a Si substrate with two pump laser pulses. The double arrows indicate the direction of the electric field vector of the pump pulse. The crater is elongated in the horizontal direction due to pump pulse irradiation at an angle. (a) CCD image of probe pulse optical fringes illuminating a Si substrate after crater and LIPSS formation in the outlined area. (b) Enlarged view of the crater and LIPSS on a Si surface. LIPSS contrast on Si surfaces is enhanced when LIPSS are illuminated with fringes. (c) Nomarski contrast image from a commercially available microscope of the same crater and LIPSS as in (b).

The temporal precision of imaging a Si surface was confirmed by studying the onset of surface melting and subsequent material removal after ultrafast irradiation. It is well known that after irradiation by a single ultrafast laser pulse, the Si surface melts and becomes more reflective

[108]. Furthermore, material removal is apparent at later time steps when the surface begins to darken. For irradiation by a single laser pulse at 0.45 J/cm^2, molten Si was visible in the probe images using the setup in Fig. 75 within 4 ps after irradiation by the pump pulse. Evidence of material removal was seen ~ 40 ps after irradiation when the center of the images first began to darken. These times are consistent with previous reports that monitor the change in reflectance with respect to the arrival time of an ultrafast laser pump pulse [108].

After forming a crater on the Si surface using a 0.45 J/cm^2 pulse, the Si was irradiated with a second laser pulse in the same region several seconds later. However, to avoid ejected material obscuring imaging of LIPSS formation at early time steps, the fluence of the second laser pulse was decreased to 0.34 J/cm^2. A lower pump fluence leads to a lower velocity of molten Si lifting off the surface [110]; therefore, changes to the Si surface can be observed before material removal obscures the surface. Figures 77(a)-(c) show the time-evolution of the Si surface after irradiation by the second laser pulse. Each image was obtained in a different, irradiated area of the sample.

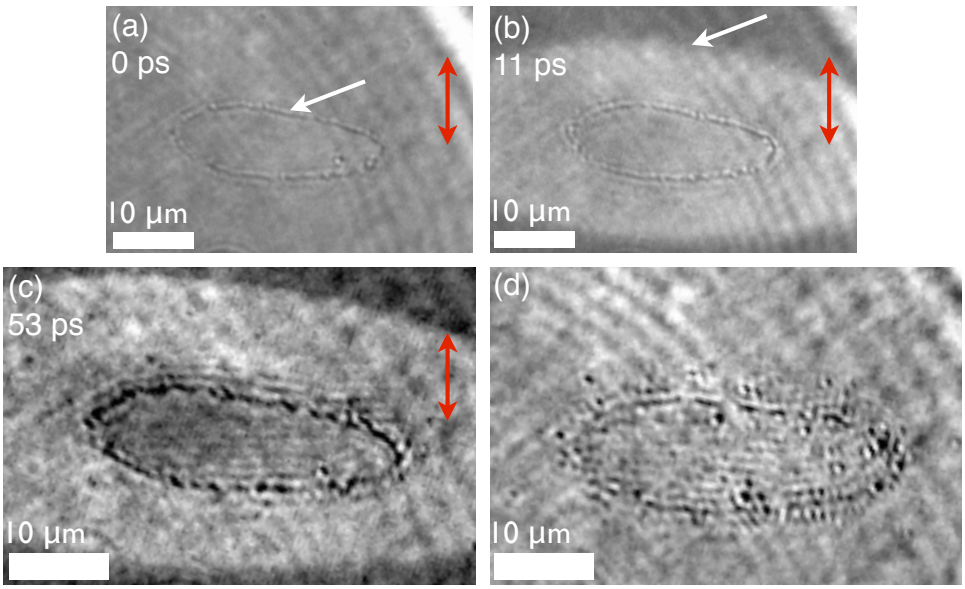

Figure 77. Pump-probe microscopy of LSFL formation. The double arrows indicate the direction of the electric field vector of the pump pulse. a) White light image of a crater formed after irradiation by a 0.45 J/cm^2 pulse. The crater edge is indicated by the single arrow. This image was taken several seconds after irradiation by the first pulse but prior

to the second pulse (designated as t = 0 ps). b) White light image of the same area shown in Fig. (a) taken 11 ps after irradiation by a 0.34 J/cm^2 laser pulse. The boundary of the lighter contrast molten Si region is indicated by the single arrow. c) LSFL are visible on the molten Si surface ~ 53 ps after arrival of the pump laser pulse. d) LSFL on the Si surface after the Si surface has cooled and resolidified.

Fig. 77(a) shows a crater, whose edge is indicated by the single arrow, which has formed on a Si surface after irradiation by the first higher fluence pump pulse and just before arrival of the second pump laser pulse. Fig. 77(b) shows molten Si formation within and around the crater 11 ps after irradiation by the lower fluence pump pulse. While the surface is molten, periodic structures perpendicular to the laser polarization form within the crater beginning at ~ 53 ps after irradiation. The dark contrast in the center of the crater in Fig. 77(c) is evidence for the beginning stages of material removal. Imaging at time steps > ~ 90 ps after irradiation are complicated by ejected material which completely obscures the periodic structures. These images are not included for brevity.

Previous single pulse pump-probe microscopy studies of high power ultrafast laser irradiation show concentric rings in the images and these are attributed to interference of probe light from a molten dome of Si lifting from the substrate[8]. Since parallel, periodic structures are present in Fig. 77(c) rather than concentric rings and parallel, periodic structures are not visible after single pulse irradiation, these images are direct evidence of the early stages of LSFL formation.

By irradiating the Si surface with two pump laser pulses, we are able to distinguish when LSFL first appear on Si surfaces and avoid complications due to irradiation by many laser pulses [111]. The first laser pulse forms a crater with a depth of ~ 15 nm. We show in Fig. 77(a) that no LIPSS form after irradiation by a single laser pulse, and the only significant surface features are crater edges. Analysis of Fig. 77(c) demonstrates that LIPSS appear on the surface after irradiation

by one more laser pulse. After cooling, LIPSS are seen throughout the crater. In Fig. 77(c), ~ 53 ps after irradiation by the second pump pulse, molten Si is still present and LIPSS have now appeared on the surface. Since the irradiated area is already molten at this time, the contrast in the image is due to height variations from LIPSS formation. The LIPSS wavevectors are parallel to the laser polarization as is typical for LSFL formation and AFM analysis shows their periods range from 600 nm to 770 nm. Finally in Fig. 77(d) LIPSS are shown long after irradiation by the pump pulse.

Material removal after ultrafast laser irradiation is attributed to rapid expansion of molten material under extreme pressures [108,112], and it has been shown that LIPSS formation is due to variations in laser intensity and molten Si temperatures over irradiated regions [103]. LIPSS formation in Fig. 77 begins before any evidence of material removal is observed and ~ 90 ps after irradiation, the Si surface and LIPSS are completely obscured by a dark contrast in the middle of the irradiated region. This dark contrast is the first evidence of molten Si lifting from the surface after irradiation which means material removal has begun within 90 ps of irradiation. Since LSFL form before the LIPSS are crater surface are obscured, it is hypothesized here that rapid expansion of molten Si and periodic variations in the amount of removed material are responsible for LSFL formation. Long after irradiation, a portion of the molten Si is ejected from the surface and LIPSS are visible on the Si surface again.

In conclusion, when irradiating polished Si surfaces, LIPSS form after irradiation by more than one laser pulse. In this manner the dynamics of LIPSS formation was studied and could be distinguished from other phenomena such as melting and ejection of material. LIPSS are observed on the same timescale as material removal, suggesting that their formation involves material ejection. For a given target material, it is expected that the pump laser pulse fluence will

determine the onset time of LIPSS formation by controlling the velocity and amount of material lifting from the irradiated surface. These studies open the possibility for studying the dynamics of LIPSS under varying circumstances such as different pulse fluences, lengths, pulse number, and materials.

5.3. Effects of Laser Parameters and Starting Surface on Ripple Patterns

5.3.1 Experimental Results

In this section, we describe the contributions of surface plasmon polariton (SPP) excitation and diffraction on the formation of LIPSS during single pulse irradiation. To accomplish this, we align the laser polarization vector in different directions with respect to well-defined, isolated step edges. Regions around the step edge are initially smooth and free of contamination or significant surface roughness. By varying the laser polarization vector orientation between experiments, SPP excitation plays a significant role in one test, and in other cases SPP excitation is minimized and Fresnel diffraction dominates. The use of a single pulse allows investigation of the multiple mechanisms responsible for LIPSS formation before one mechanism (i.e., SPP) dominates. Since only LSFL formation is discussed in this work, LSFL will be referred to as LIPSS throughout this study.

A lift-off process comprised of photolithography and sputter deposition was used to make isolated Au mesas adhered on the (100) plane of a Si wafer for subsequent laser irradiation. Photolithography involved sequential spin-coating of 5214 resist, solvent bakeout, UV exposure of the resist through a pre-fabricated mask, pattern development and, finally, rinse. With features created in resist, the wafer was cleaned in an oxygen plasma prior to loading into a Unifilm, Inc. PVD-300 sputter deposition chamber. Direct current magnetron sputter deposition coated the entire wafer with Ti/Au to a thickness of 110 nm (i.e., 10 nm Ti and a 100 nm Au cap). The Ti/Au deposited on to patterned resist was then lifted off (removed) by soaking in acetone and isopropyl

alcohol to leave only the Ti/Au deposited onto Si. All horizontal edges of the resulting mesas were aligned along the [110] direction of the Si wafer.

A Clark-MXR CPA-2001 Ti:sapphire pulsed laser with a 150 fs pulse length, centered at a wavelength of 780 nm, with a repetition rate of 1 kHz, a maximum pulse energy of 1 mJ, and a Gaussian intensity profile, was focused to a $\frac{1}{e^2}$ diameter of ~ 60 μm using a 20 cm focal length lens. Samples were affixed within the focus of the beam using a Newport 4-axis translation stage, which allows for positioning in the x, y, z, and θ lab directions with 2 μm accuracy. Single laser pulses were isolated from the 1 kHz pulse train using a Thorlabs optical chopper and a Uniblitz fast mechanical shutter. All irradiation experiments were conducted in air at normal incidence, and the focus of the laser beam was centered on mesa edges. More details of the experimental setup can be found in a previous publication[6].

After laser irradiation, the damage spots were investigated optically using an Olympus BX-51 fluorescence microscope with differential interference contrast (DIC) and height profiles were obtained with a Veeco Dimension Icon atomic force microscope (AFM) operated in tapping mode. All stated fluences are peak fluences and were calculated using the formula $F = \frac{2E}{\pi ab}$ where F is the peak fluence, E is the energy per pulse calculated by dividing the average power measured using an Ophir Optics, LLC thermal power sensor by the repetition rate, and a/b are the major and minor radii at $\frac{1}{e^2}$ intensity of the elliptical, focused beam measured using a DataRay Inc. WinCamD 14-bit beam profiling CCD camera with a 20X objective attachment. Variations in the measured beam area and power corresponded to a ± 0.02 J/cm^2 variation in reported fluences.

The effects of irradiating one edge of a square mesa with a single, linearly polarized laser pulse at a fluence 0.50 J/cm^2 are shown in Fig. 78. LIPSS form on both the Au film and Si

substrate near the mesa step-edge when the polarization vector is perpendicular to the step edge. In this case, LIPSS are visible more than 10 mm from the edge, but the centrally-irradiated areas are damaged due to a locally-high light intensity. LIPSS may initially form when material removal is at its beginning stages, but eventual material removal, re-deposition, and debris formation render measurement of a LIPSS period impossible.

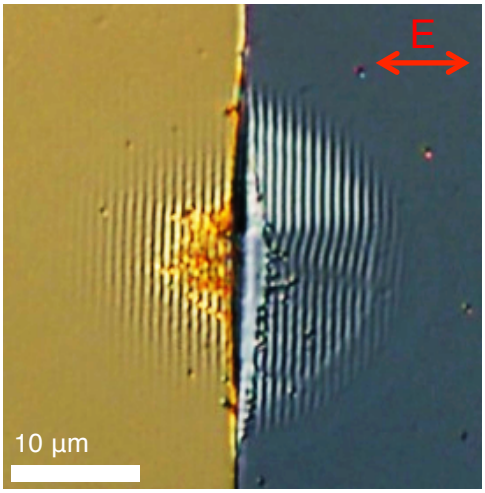

Figure 78. LIPSS formation on Au and Si surfaces after irradiation of a mesa edge at a fluence of 0.50 J/cm^2. For local fluences ≥ 0.50 J/cm^2 it is not possible to determine a LIPSS period. In this case, material removal, re-deposition, and debris formation damage LIPSS which may have initially formed on the surface after irradiation.

The effects of irradiating one edge of a square mesa with a single, linearly polarized laser pulse at a fluence of 0.30 J/cm^2 are shown in Fig. 79. This fluence is equal to the measured, wavelength-dependent threshold for removing material from a Si surface by a single laser pulse when irradiation is completed away from Au mesas. Irradiation of the mesa in Fig. 79 results in LIPSS formation on the Si surface. Periodic structures are also present on one of the Au surfaces (in Fig. 79a), which involved a perpendicular polarization relative to a step edge, although less apparent. AFM measurements have shown the LIPSS on the Si surface are a series of peaks above

and valleys below the original Si surface, and their magnitudes decrease with increasing distance from the mesa edge. LIPSS periodicity distributions within the irradiated region were determined by performing Fourier transforms on AFM height traces of individual LIPSS periods, calibrated to ± 10 nm in-plane. AFM traces were obtained from at least 30 different regions where LIPSS formed, and the resulting distributions of periods are graphed in Fig. 79.

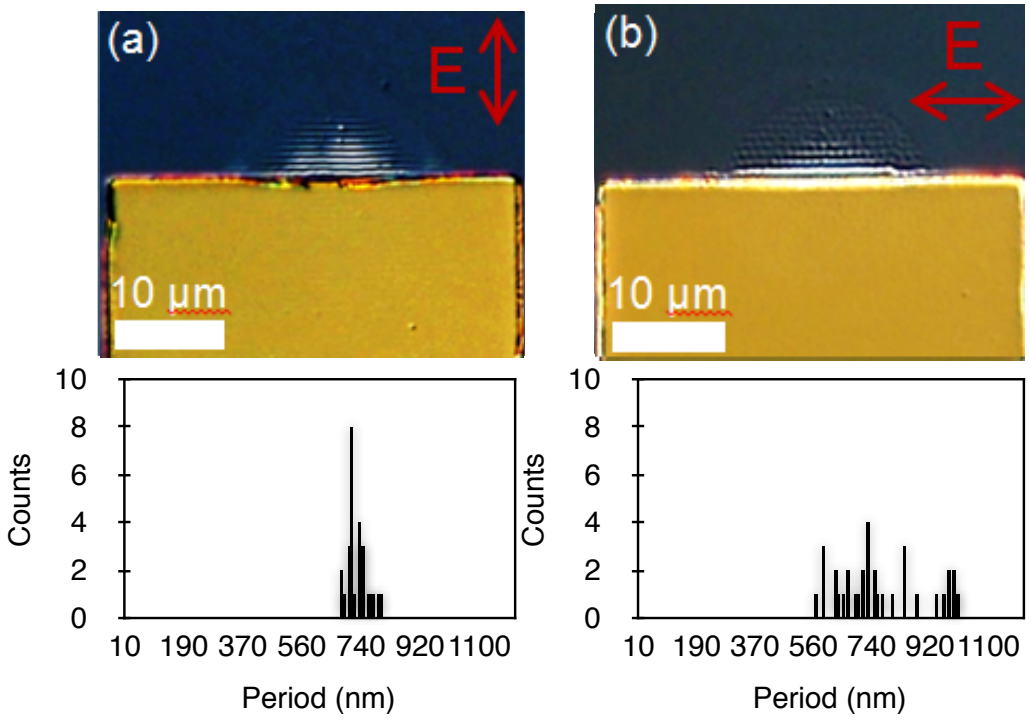

Figure 79. Optical images after irradiation of a mesa edge at a fluence of 0.30 J/cm^2 for two different laser polarizations. The histogram plots below each image show the distributions of LIPSS periods on the Si surface for each laser polarization, measured in a direction perpendicular to the Au step edge. (a) When the laser polarization vector is perpendicular to the mesa edge, the distribution of measured LIPSS periods is peaked near a single value. (b) When the laser polarization vector is parallel to the mesa edge, the distribution of periods is not peaked near a particular value.

When the electric field vector is perpendicular to a mesa edge, LIPSS mostly form with wavevectors perpendicular to the edge. A distribution of periods peaked near a value of 710 nm results, seen in Fig. 79(a). If the fluence is increased to 0.38 J/cm^2, the peak of the period

distribution shifts to 740 nm (not shown for brevity). For electric field vectors parallel to mesa edges, as in Fig. 79(b), LIPSS form on Si with wavevectors both perpendicular to the edge and at other orientations. In this case, the distribution of periods measured in directions perpendicular to the mesa edge is not peaked near a single wavelength. AFM height traces, taken perpendicular to mesa edges from Figures 79(a) and (b), show that LIPSS valleys below the original Si surface have larger amplitudes than peaks above the original surface. LIPSS for laser electric field vectors perpendicular to mesa edges have average peak-to-peak amplitudes approximately three times greater than when the polarization vector is parallel to mesa edges. LIPSS are not detected on the Au mesa for a fluence of 0.30 J/cm^2 when the polarization vector is parallel to the mesa edge.

After irradiation of a mesa edge at 0.20 J/cm^2, it was found that periodic structures are visible on the Au and Si surfaces for electric field vectors perpendicular to mesa edges, seen in Fig. 80(a). This fluence is at the measured ~ 0.20 J/cm^2 threshold for melting bulk Si surfaces. The melt threshold of bulk Si was determined by observing changes in the Si surface reflectivity due to amorphization far away from mesa microstructures after irradiation. AFM measurements of the periodic structures on the Si surface in Fig. 80(a) did not detect height changes. The AFM image in Fig. 80(b) shows height variations on the Au surface, and the AFM height trace in Fig. 80(c) shows periodic valleys and hills with amplitudes on the order of 1 – 2 nm. To reduce noise, the height trace in Fig. 80(c) is an average of 10 different traces within the region bounded by the dashed lines in Fig. 80(b). After irradiation at the same fluence for electric field vectors parallel to mesa edges, no periodic structures are visible on either the Au or Si surfaces. Below 0.20 J/cm^2, no periodic structures were observed on either the Au film or Si substrate for any in-plane orientation of the laser polarization vector.

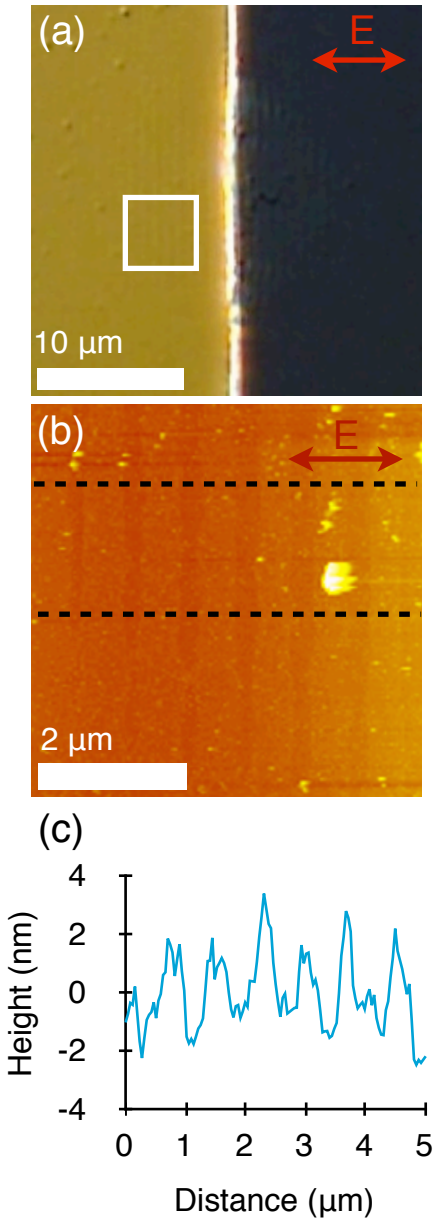

Figure 80. (a) Periodic structure formation on Au and Si surfaces after irradiation by a single laser pulse at a fluence of 0.20 J/cm^2. The laser polarization vector was perpendicular to the mesa edge. (b) AFM image of the Au surface from the inset in (a). (c) Average height trace from the region bounded by the dashed lines in (b). The trace shows periodic valleys and hills on the Au surface without a significant presence of hills. Height = 0 corresponds to the original Au surface.

During laser irradiation, the spatial distribution of laser light at material surfaces directly affects the laser-material interaction through variations in the surface temperature [101,103].

Depending on the irradiation conditions, diffraction of laser light from surface features and SPP excitation[4] can participate in this process by changing the intensity and frequency of light which is absorbed by the surface. SPP excitation is a polarization dependent process which increases the local intensity of light at metallic surfaces when a component of the laser polarization is perpendicular to surface defects [102]. The excitation of SPPs increases the intensity of light at the surface and is reported to shift the wavelength of coupled light below that of the incident light.reference When the laser polarization vector is parallel to edges, SPP excitation is minimized and Fresnel diffraction dominates [111].

In this work, mesa edges are surface defects, which may, in turn, excite SPPs during laser irradiation. After irradiation of mesa edges by a single laser pulse, when the laser polarization vector is perpendicular to an edge, it was found that the amplitude of LIPSS valleys and hills on the Si surfaces were greater than when the polarization vector was parallel to edges. This is consistent with SPP excitation playing a significant role in LIPSS formation for this single polarization vector relative to mesa edges. SPP excitation increases the local intensity of light at the Si surface, and, compared to when SPP excitation is not allowed, more light will be absorbed by the Si surface. While Si is an intrinsic semiconductor, Si surfaces become metallic once a critical carrier density is reached after irradiation by the first few cycles of the incident laser pulse [112]. Therefore, due to changes in reflectivity during irradiation, the laser fluence which is absorbed by the Si surface will be lower than the incident fluence, and lower than that predicted by assuming the reflectivity of bulk Si. The remainder of the laser pulse may then couple with electric fields on both the Au and Si surfaces and form SPPs when the electric field vector is perpendicular to surface features.

For local fluences > 0.50 J/cm^2, the LIPSS period on Si surfaces is predicted to approach the fundamental laser wavelength due to SPP excitation[8], it was not possible to reliably measure the LIPSS period due to large amounts of material removal and possibly flow. For fluences of 0.30 J/cm^2 in Fig. 79(a), when SPP excitation is allowed, the periodicity is peaked near a single period. Under ideal conditions, this period shift due to SPP excitation can be predicted[8]. However, for statistical purposes, more than one LIPSS period is necessary to determine a representative periodicity. When SPP excitation is allowed, the LIPSS period varies with laser fluence. Due to the Gaussian intensity profile, the local fluence continuously varies over the regions where AFM measurements were taken in Fig. 79, making it difficult to correlate a single fluence to a single LIPSS period. Electric field enhancement at the mesa edge could also increase the electric field value above that initially set by the laser fluence, and the flow of molten material may also affect the LIPSS periodicity as they are forming. Nevertheless, the peak of the LIPSS distribution for irradiation of mesa edges slightly above the Si removal threshold is within the range predicted by Bonse, et. al. [113].

In Fig. 79(b), LIPSS on the Si surface are not centered near a particular wavelength and they span part of the visible and near-infrared regions of the electromagnetic spectrum. A wider distribution of periods likely results from the activation of more than one LIPSS formation mechanism, and consequently, LIPSS form in multiple directions, seen as the cross-hatch pattern. SPP excitation and a previously discussed Fresnel diffraction mechanism[6] are suggested to both play a role in LIPSS formation on Si surfaces when the polarization vector is parallel to mesa edges. Since the exact roughness of edges is not known, it could not be determined if SPP excitation is completely diminished when the laser polarization is parallel to mesa edges. However, SPP excitation is at least minimized in this case, Fresnel diffraction dominates, and

lower amplitude LIPSS are formed. SPP excitation near surface defects on the mesa edge may be responsible for LIPSS formation with wavevectors at other orientations in Fig. 79(b).

The threshold for the formation of any periodic structure on the Au and Si surfaces is evident in Fig. 80. AFM measurements show the periodic structures on the Au surface in Fig. 80(a) are a series of hills and valleys with equal amplitudes. Since the amplitude of these structures does not significantly vary with distance, as is the case for LIPSS on the Si surface, the SPP boundary conditions on the Au surface may be significantly different than those on the Si surface. The electric field intensity distribution at Au mesa surfaces will be a subject of future study.

When SPP excitation is minimized for laser polarization vectors parallel to the mesa edge, no periodic structures on either surface are visible after irradiation at 0.20 J/cm^2. Therefore, for laser polarization vectors perpendicular to the mesa edge in Fig. 80, SPP excitation is responsible for the polarization dependence of periodic variations in the temperature of the Au and Si surfaces and subsequent periodic structure formation. The presence of periodic variations of higher reflectivity Si, also seen by other groups [113], without any height variation suggests these structures are due to either amorphous or polycrystalline Si formation after surface melting. Since the Au and Si melt thresholds are ~ 0.50 J/cm^2 [114] and ~ 0.20 J/cm^2 respectively, differences in carrier densities are likely responsible for the formation of periodic hills and valleys on the Au surface before any height variation is observed on the Si surface. Au has an intrinsic carrier density of ~ 10^{22}/cm^3 [115], an order of magnitude higher than the critical carrier density Si during irradiation (~ 10^{21}/cm^3) [116]. A higher carrier density allows for SPP excitation on the Au surface at lower fluences than those required for Si; therefore, the Au surface may be reaching higher temperatures than the Si surface after irradiation by the same fluence.

From these results, both SPP excitation and Fresnel diffraction likely play a role in the beginning stages of LIPSS formation after irradiation of bulk substrates with multiple laser pulses. Depending on the laser fluence, the first few laser pulses will form defects and/or crater edges. Subsequent laser pulses will diffract laser light near surface features and Fresnel diffraction forms LIPSS for all in-plane angles of the electric vector with respect to features. When the electric field vector is perpendicular to surface features, SPP excitation increases the local intensity of laser light absorbed at the Si surface. Increased light absorption leads to higher molten Si temperatures, more material removal from the surface, and deeper LIPSS for wavevectors parallel to the laser polarization vector.

In conclusion, both SPP excitation and Fresnel diffraction are shown to play roles in LIPSS formation during ultrafast irradiation of Au mesa microstructures. The activation of either mechanism is dependent on the orientation of the laser polarization vector with respect to mesa edges. Subsequently, the formed LIPSS period and amplitude are dependent on which mechanism is activated. Since the reflectivity of the Si is different after irradiation than bulk Si, such periodic formation of amorphous and/or polycrystalline Si may be important for applications where periodic variations in the refractive index of a surface are desired.

5.3.2 Model Results

In order to confirm our hypothesis and develop an improved understanding of why surface ripples form, we have completed predictive model simulations using an Electromagnetic Solver (COMSOL). This numerical modeling approach has investigated the relative roles of beam

characteristics such as (peak intensity, light polarization, wavelength) and expanded this to study the potential role of surface plasmon polaritons, Fresnel diffraction and other potential effects.

Generally, we reproduce in the model the key characteristics of the incident single pulse of laser light. Also, the single step edge structure (constructed in the laboratory by photolithography, sputter deposition and liftoff) is included. This has more often involved a ~100 nm high Au mesa structure on Si although our recent models have expanded to include additional materials. Once constructed, the EM solver predicts how the electric field varies across all surfaces. Figure 80 depicts some of the key characteristics of the model.

It is surmised that the periodic, intensity maxima present on the surfaces correlate with the selective ablation/evaporation of material from different sites on a surface that results in a periodic ripple morphology. Thus, conditions, such as intensity and polarization were intentionally varied to match experiments and compare.

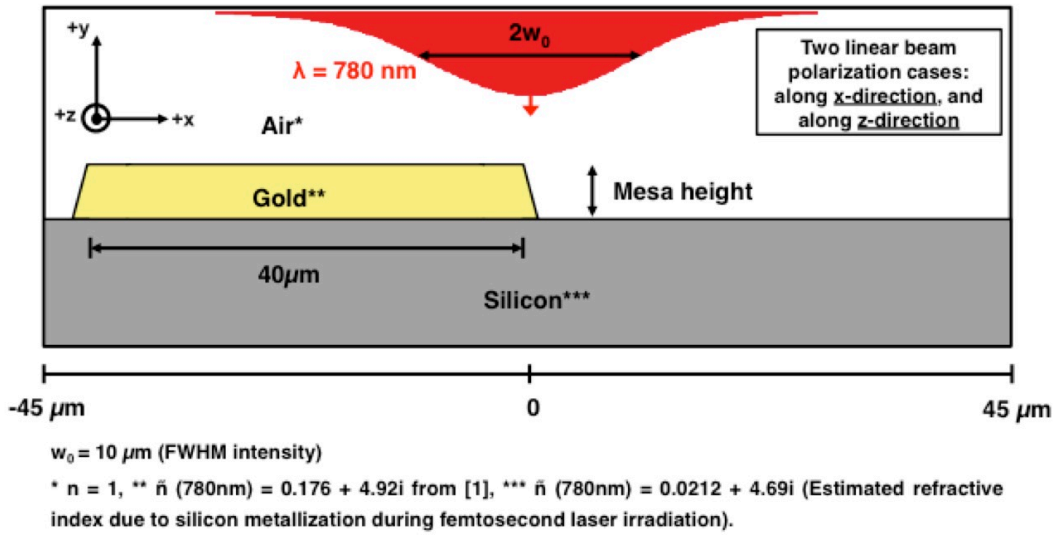

Figure 81. Characteristics of the incident laser beam and starting surface structure included within our predictive model simulations and general nomenclature therein. These generally match the characteristics used prior experiments.

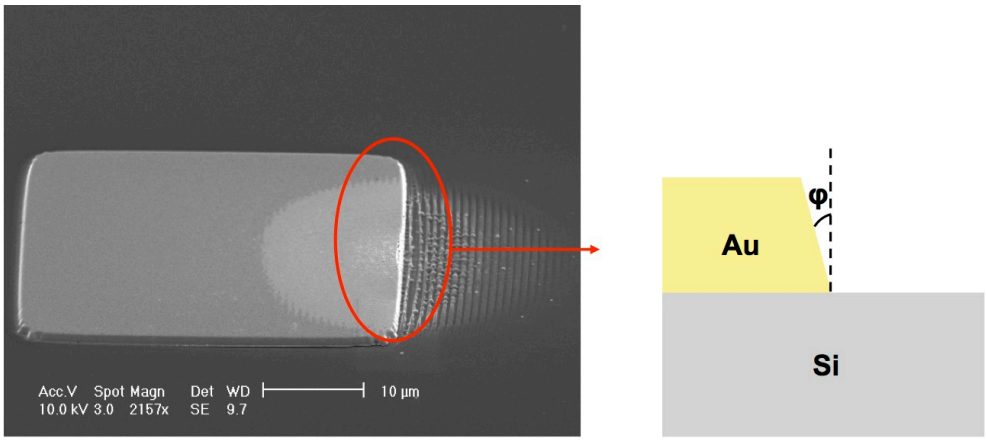

Figure 82. The scanning electron microscope image on the left shows a Au mesa structure after single pulsed laser irradiation. The depiction on the right reports that our mesa structures have a measurable sidewall angle, which is found to be important to the produced ripple characteristics.

Taking into account the various structural/compositional details of initial surfaces and the shape, size, pulse duration, etc. of incident light, our model simulations have successfully predicted periodic variations in electric field intensity that share many of the same characteristics of produced ripple patterns.

Generally, the electric field variations are produced because of Fresnel diffraction. A portion of the incoming pulsed light is diffracted from the edge of the mesa. Interference of waves is seen in Figure 83 both at the surfaces of the specimen and in free space. Results are shown in Figure 83 for different mesa heights, which strongly affects the intensity at the surface. Also evident in these figures nonzero sidewall angles have an effect on the intense variations in electric field present at surfaces. In particular, a tapered sidewall leads to a much stronger average intensity variation for the case of the 585 and 780 nm tall mesas. Note: the sidewall is taken to be representative of that measured in experiments by scanning electron microscopy.

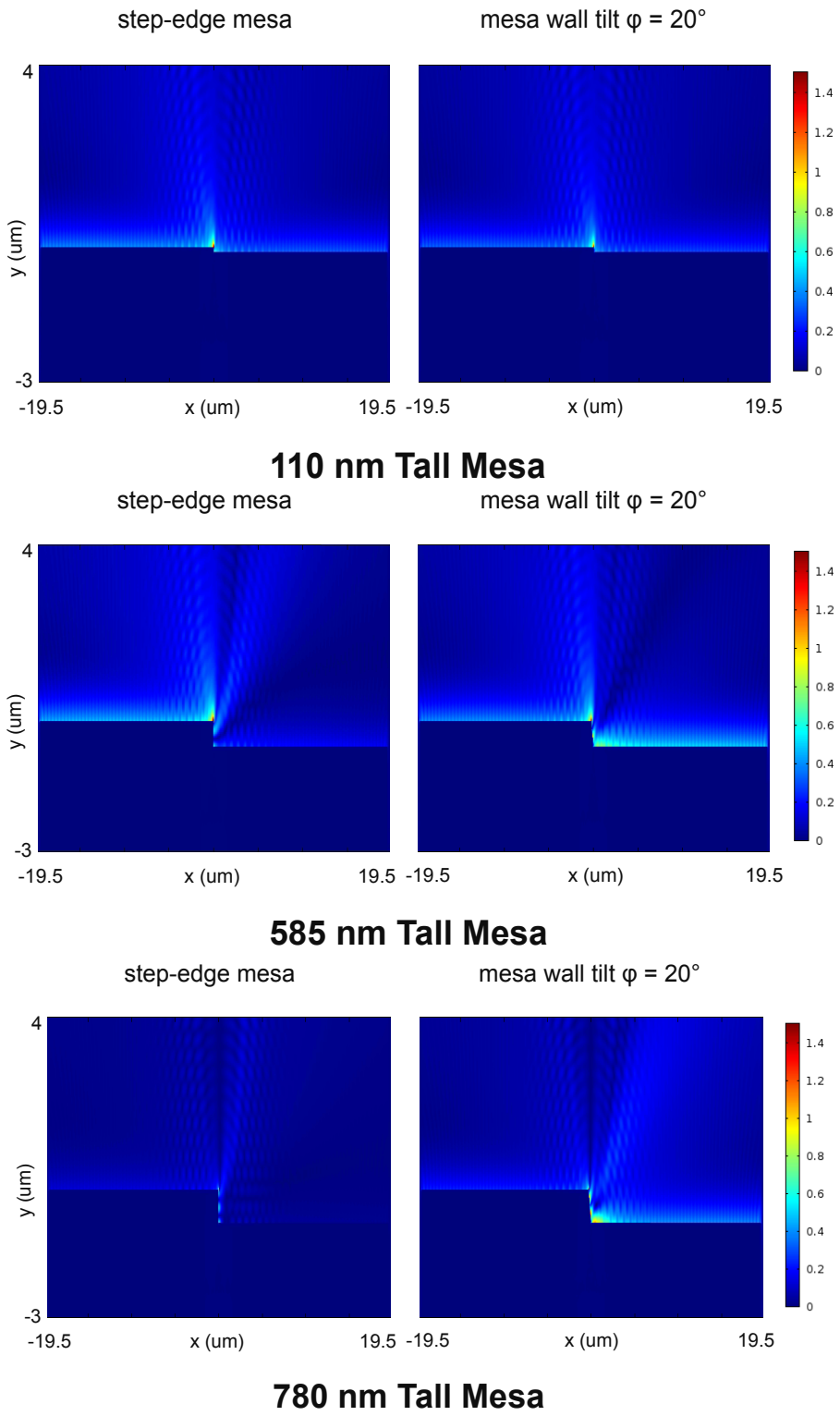

Figure 83. Model predictions of electric field variations (shown in cross section) across a mesa structure of a given, specified height. Two cases are shown for each mesa including vertical sidewall steps (shown on left) and those having a 20° sidewall angle. In each representation, the mesa is shown on the left and the lower surface (Si) is shown on right.

Several characteristics of periodic ripple structures predicted by model simulations were validated in the laboratory through measurement. For example, model simulations has been used to predict the variations in electric field intensity across a Si and Au surface for different polarization directions. In Figure 84, results are shown for the case wherein the polarization direction is oriented perpendicular with respect to the irradiated edge of a mesa. Furthermore, the average period of the electric field (on both surfaces) is less than the wavelength of incident light. The two bottom plots (one for Au surface and one for Si) show a decreasing amplitude with distance away from the edge, consistent with the general effect shown in Figure 82. Variations are, additionally, predicted in Figure 84 as a function of mesa height. Of note, there are mesa heights (390 nm and 720 nm) wherein predicted amplitudes (on Au) are minimal.

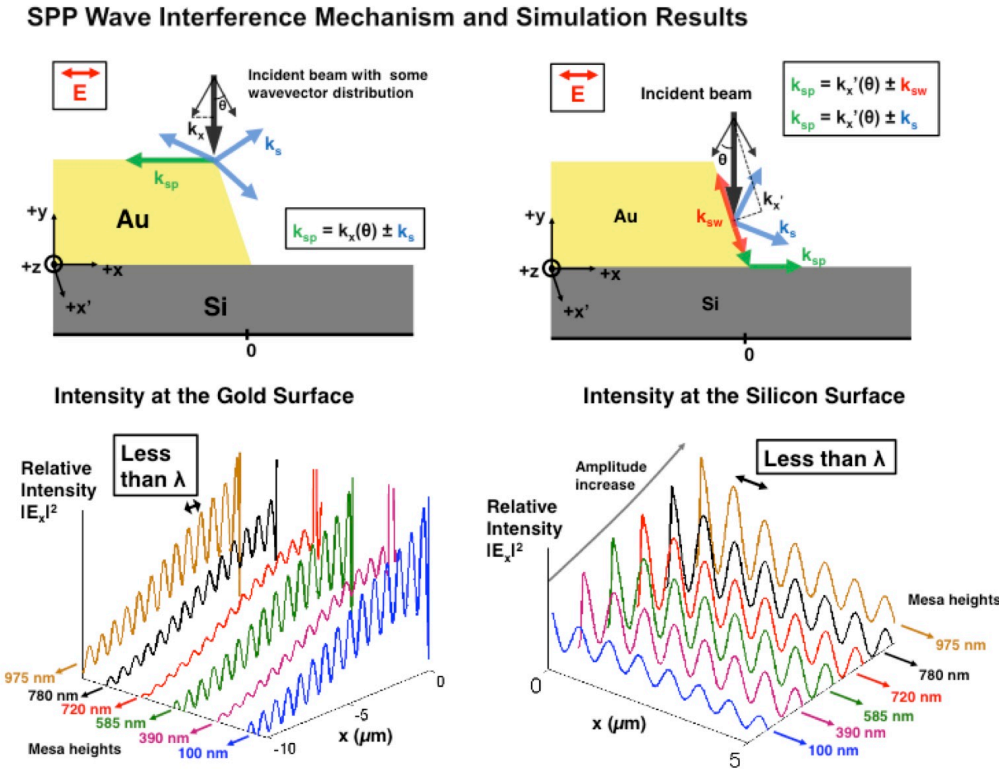

Figure 84. Model predictions of electric field variations as a function of mesa height for the case where incident, pulsed light is polarized with a wavevector that is aligned perpendicular to the mesa edge (oriented into the page of this drawing). Results shown include the intensity variations on the Au and on the lower Si surface.

Laboratory experiments have been used to validate many of the model predictions. For example, two sets of results are shown in Figure 85 that are quite consistent with the aforementioned model results for the case considering polarized light oriented perpendicular to a step edge. On the left is the experiment involving a 100 nm high Au mesa. Ripples are formed on both Si and Au, with those on Si being more prevalent (similar to model predictions). Other consistent features include a decaying amplitude away from the step edge on both Au and Si. Of note, the measured period of this rippled morphology is less than the incident wavelength of pulsed light (780 nm, shown in red in the graph).

The experiment shown on the right side of Figure 85 similarities and differences that are each consistent with model predictions. Again amplitude decays away from the edge as in the 100 nm case and the average period is suppressed compared with the incident wavelength. In addition, no evidence of ripples is found on the Au for the case of the 720 nm high structure. Recall from Figure 85 that this is a height, that is predicted to produce minimally varying electric field intensity on gold.

In general, one of the most recognizable features of ripples (and one that is likely to vary when a focused laser beam is scanned across a rough surface) is its period. In the case of the models and experiments in these figures, the conditions are optimized for surface plasmon polariton generation. The alignment of the polarization gives rise to collective electron excitation which can distort the local electric field. For this reason, we argue that both models and experiments support our hypothesis that surface plasmons affect diffracted laser light in such a way as to decrease the period of electric field variations, and this leads to a reduced ripple wavelength.

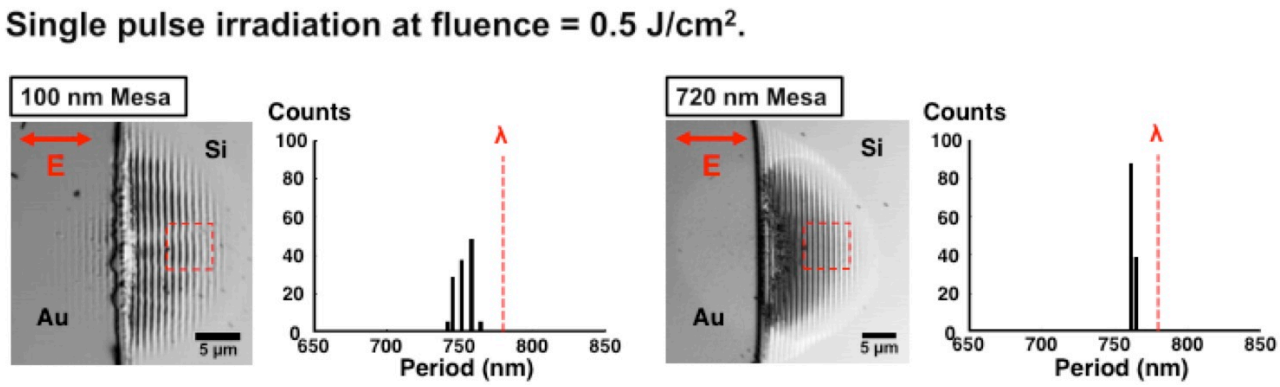

Figure 85. Results from validation experiments involving two different mesa heights, 100 and 720 nm. Plan view images show the formed ripple patterns produced on Au and on Si after single pulse irradiation. In these two experiments, the polarization direction is aligned normal to the irradiated mesa edge as shown. Plots next to each image summarize measured ripple periods. This example shows ripple periods that are less than the wavelength of incident light, which is consistent with model predictions.

Additional model simulations and validation experiments have been completed to explore the opposite polarization orientation, one in which its direction is aligned parallel to a linear mesa edge. Results from model simulations are shown in Fig. 86.

Model simulations again show that electric field intensity should vary across the surface – an effect of Fresnel diffraction. In addition, similar to the earlier case, ripple amplitude decays with distance away from a step edge. Nevertheless, there are several differences noted. On the right, the plot shows that the period of electric field variations is of the order of the incident light wavelength with some variation along the path. This is different than the previous case, which was optimal for surface plasmon generation.

Validation experiments shown in Fig. 87 demonstrate many of the predicted characteristics. The ripple period was measured by Atomic Force Microscopy (AFM) and found to be equal (on average) to the wavelength of incident light, although some variation was found. With this similarity and knowing that conditions are not optimal for collective electronic excitations, Fresnel diffraction is thought to be largely responsible for formed patterns.

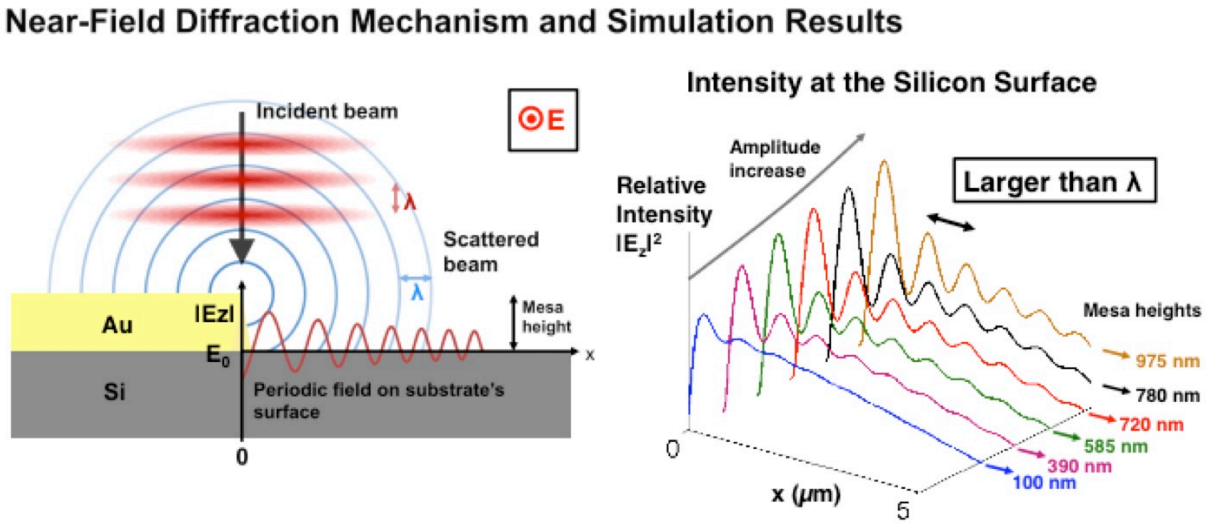

Figure 86. Model predictions of electric field variations as a function of mesa height for the case where incident, pulsed light is polarized with a wavevector that is aligned parallel to the mesa edge (oriented into the page of this drawing). Results shown include the intensity variations on lower Si surface.

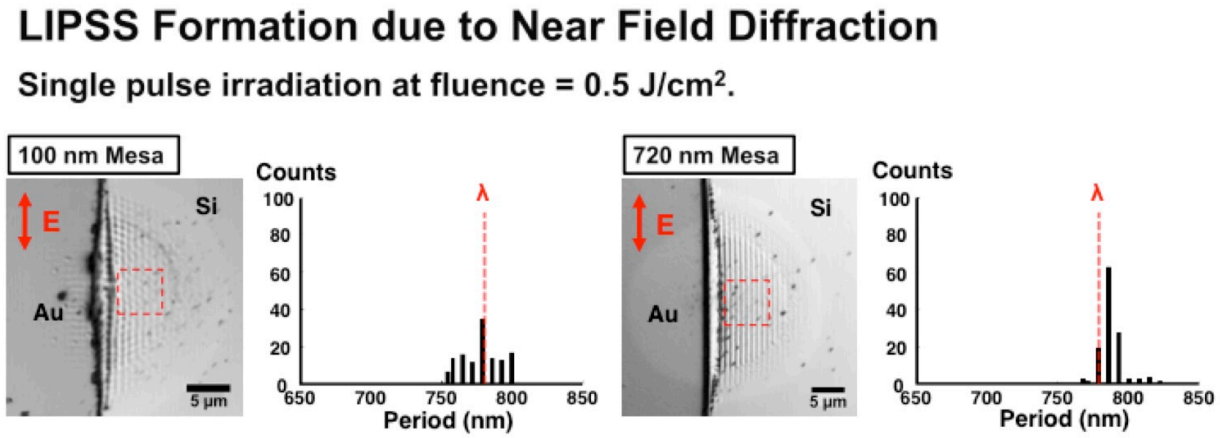

Figure 87. Results from validation experiments involving two different mesa heights, 100 and 720 nm. Plan view images show the ripple patterns produced on Au and on Si after single pulse irradiation. In these two experiments, the polarization direction is aligned parallel to the irradiated mesa edge as shown. Plots next to each image summarize measured ripple periods. This example shows ripples whose mean period is equal to the wavelength of incident light - consistent with model predictions.

6. INTERROGATION METHODS

6.1. Methods for Interrogating Color Markings

6.1.1 Interrogating Macro-scale Patterns

In general, macro-scale color barcodes can be scanned or photographed using a common device such as a cellular telephone camera. Most barcode readers currently do not incorporate color information, so a grayscale rendition is useful at this time. QR type bar codes, such as the one in Figure 88, have been interrogated successfully using common, commercially-available applications.

Restricted to working with grayscale versions of an existing color pattern can nevertheless provide additional capability. The color information can indicate other important details, such as

Figure 88. Multicolor, two dimensional bar code (QR type) created on Ti by scanned laser stimulated oxidation.

date of manufacture, country origin, etc. that is not encrypted in the barcode.

Additionally, the spectral signature of colored regions can be captured using a spectrophotometer operating with a submillimeter beam size. Spectra (or colors) can be captured pixel by pixel and catalogued like that in Figure 89.

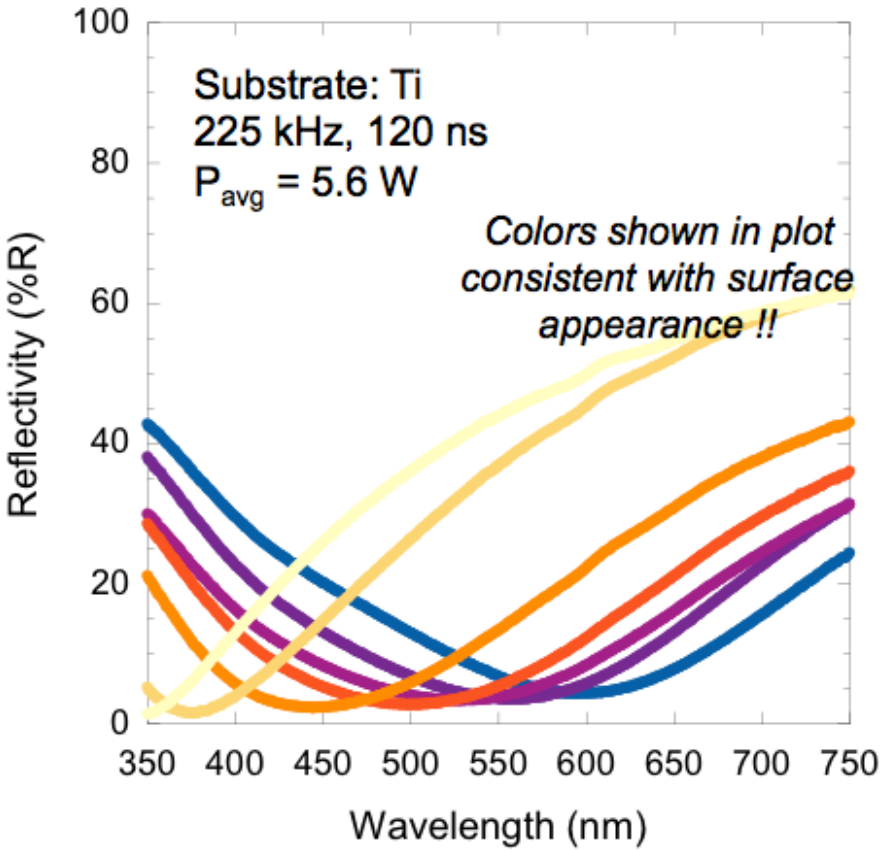

Figure 89. Reflectivity spectra obtained from different square color pixels created on a Ti surface.

Other characteristics of laser marked surfaces require laboratory-based methods for interrogation. For example, laser scan lines represent a unique identifier and the direction of scanning can be rotated in neighboring square pixels to add complexity. As shown with a

depiction in Figure 90, the average color of a square pixel can be tailored while independently adjusting the laser scan direction. Thus, a targeted macro-scale color pattern can be achieved to have barcoded information in addition to having complex micro-scale features. In this drawing, the parallel lines drawn within each square feature indicate the associated laser scan directions. The periodicity of scan lines owes to the hatch utilized in the process, of the order ~ 10 μm.

Speckle – based methods are then used to interrogate individual square pixels of the pattern. Characterization involves directing polarized, coherent light onto individual color features and capturing the reflected light on a neighboring CCD camera. For this, a HeNe laser pointer was utilized and measured, reflected light was specular. The laser – to – sample distance was varied up to ~1.0 m and the sample – to – detector distance was of similar length.

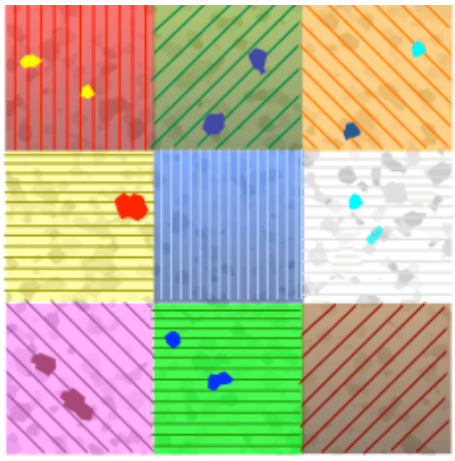

Figure 90. Depicted laser color pattern wherein laser scan direction is varied in neighboring square pixels.

As demonstrated in Fig. 91, laser speckle is able to resolve the wavevector of the roughness formed as a result of laser scanning. Sixteen different color features are shown on this particular specimen, wherein the laser scan direction was fixed for a given square pixel, but then rotated in

neighboring pixels. The laser speckle patterns obtained from three of these features are included at the top of the figure. Analysis of patterns shows that the semi-major axis of the laser speckle ellipse is aligned with the direction of laser scanning (indicated with arrows in the top three patterns). Scan lines of square pixels are sometimes (but not always) evident to the eye.

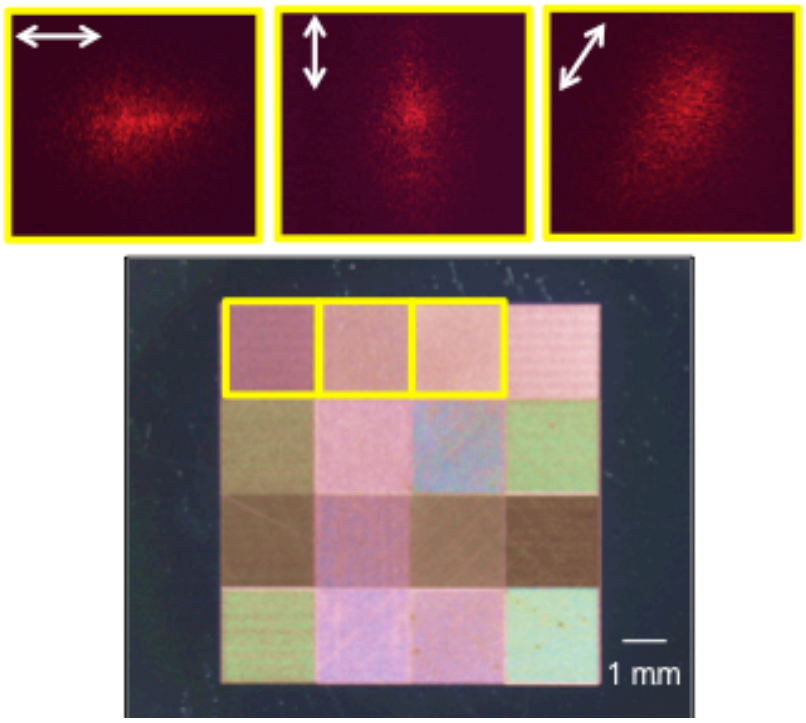

Figure 91. (bottom) Laser color pattern wherein the laser scan direction was varied in neighboring square pixels. (top) Laser speckle patterns obtained from the three color pixels identified with yellow squares. Each of these three square pixels had laser scan directions aligned with the arrows shown above.

6.1.2 Interrogating Micro-scale Color Islands

Laser-color markings produced on bulk metal samples were also evaluated by UV-Vis-IR microspectrophotometry. This technique is a new, non-contact, light-based method capable of rapid, accurate interrogation of color islands and surrounding features. The instrument selected for characterization is a commercially-available microspectrometer from CRAIC, Inc. A picture of

this instrument is included in Figure 92. We find that this unit can determine the spectral reflectance of microscopic planar areas and generate spatial maps of color (or spectral reflectance).

By spectral reflectance, we specifically mean the reflectance over a range of different wavelengths. A 20X objective is used for both identifying regions of interest and for evaluating spectral response of areas within the field of view. The OEM claims that the instrument is calibrated using filters that are traceable to NIST Standard Reference Materials.

Figure 92. Microspectrophotometer used for the evaluation of microscale regions (including color islands) on laser marked, bulk metal samples. Image from CRAIC website.

First, samples produced with no color islands (such as that shown in Figure 93 made using a fluence of 200 J/cm^2) were scanned to determine spectral reflectance point-by-point. Areas such as the 10 x 10 μm area highlighted with a red-outlined box in this figure were evaluated over a

range of wavelengths from 400 to 700 nm and stitched to form a color map. The particular highlighted (box) area spans two laser scan lines.

As demonstrated with a few representative maps in Figure 94, this method proved useful in determining the many color variations across a sampled area. The particular wavelength listed to the right of a given color map was incident on the specimen and the reflectance values are wavelength specific. Sample acquisition time was rapid with 10 x 10 μm areas requiring seconds.

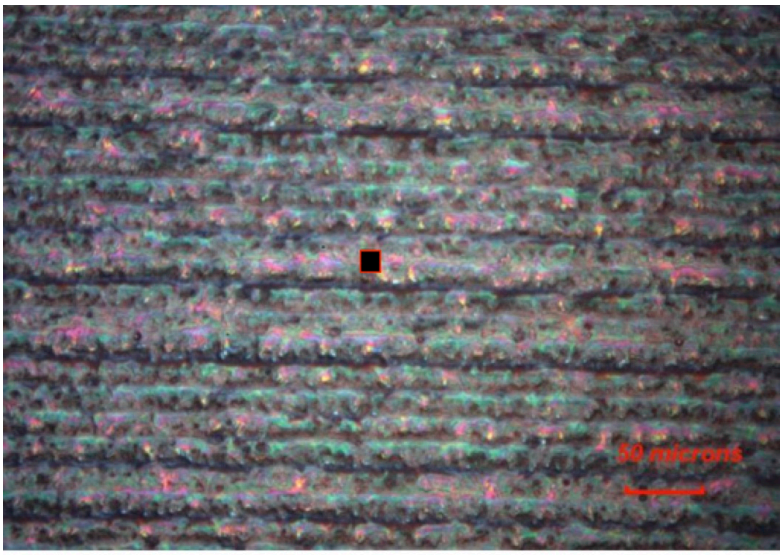

Figure 93. Optical image of a laser colored area on SS304L that has not formed colored islands. This entire area was sampled using the UV-Vis-IR microspectrophotometer. The microscopic area shown with a red outlined box was sampled to produce the spatially resolved reflectance/color maps included below.

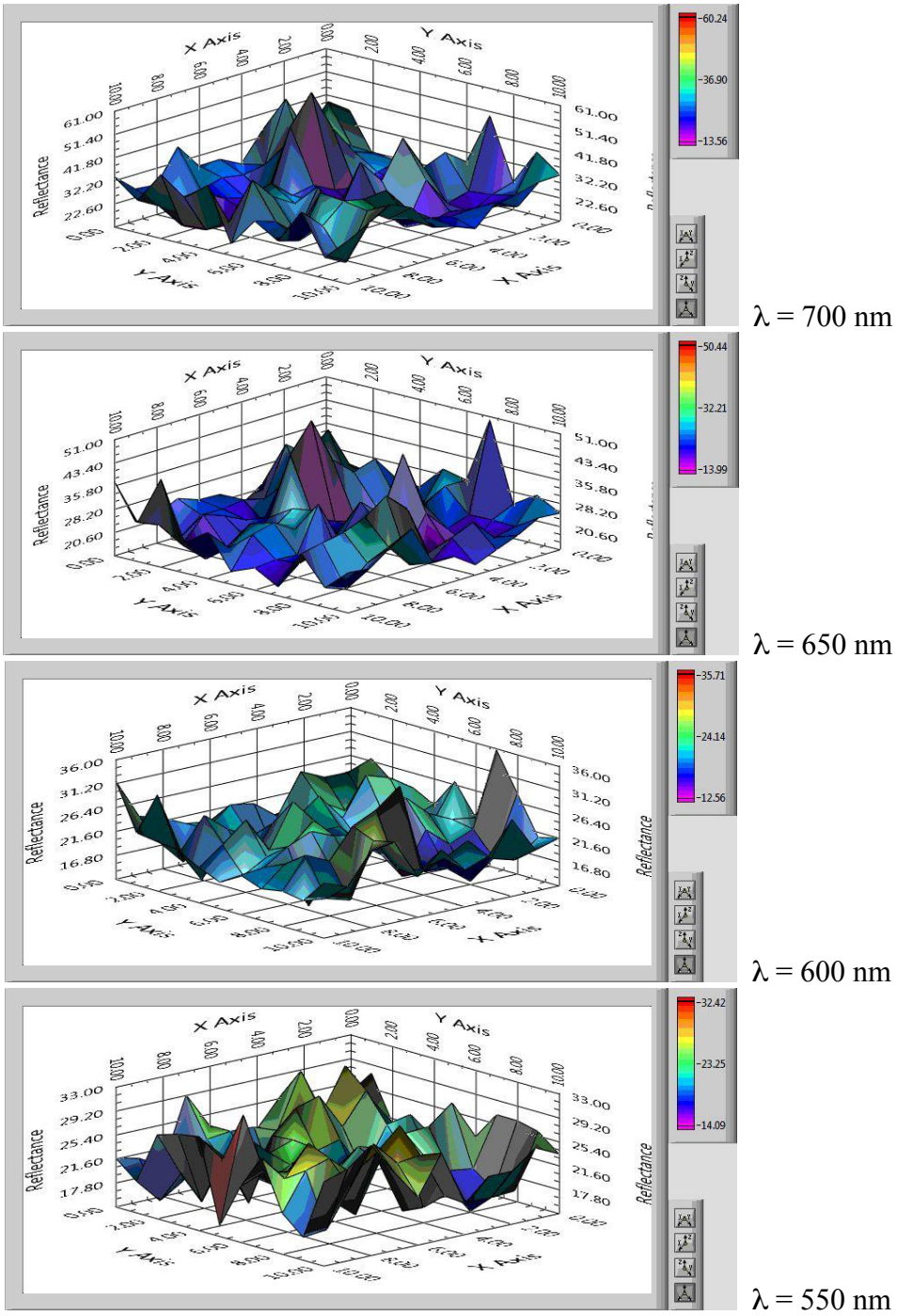

Figure 94. Spatially resolved color/reflectance maps of a laser-treated stainless steel sample. Little variation is found across the 10 x 10 μm area. No color islands were present on this sample's surface.

Additional, laser-color marked stainless steel samples comprised of microscale color islands were also evaluated using the same method in order to determine if islands could be

identified and, if so, whether they exhibit unique spectral reflectance. The image in Figure 95 shows an area treated with a single, uniform laser fluence. The microscopic area highlighted with a red-outlined box was selected for demonstration, as it contains a portion of one color island. This is shown in more with a high magnification view in the bottom image of Figure 95. Wavelength specific color maps of this microscopic region are included in Figure 96.

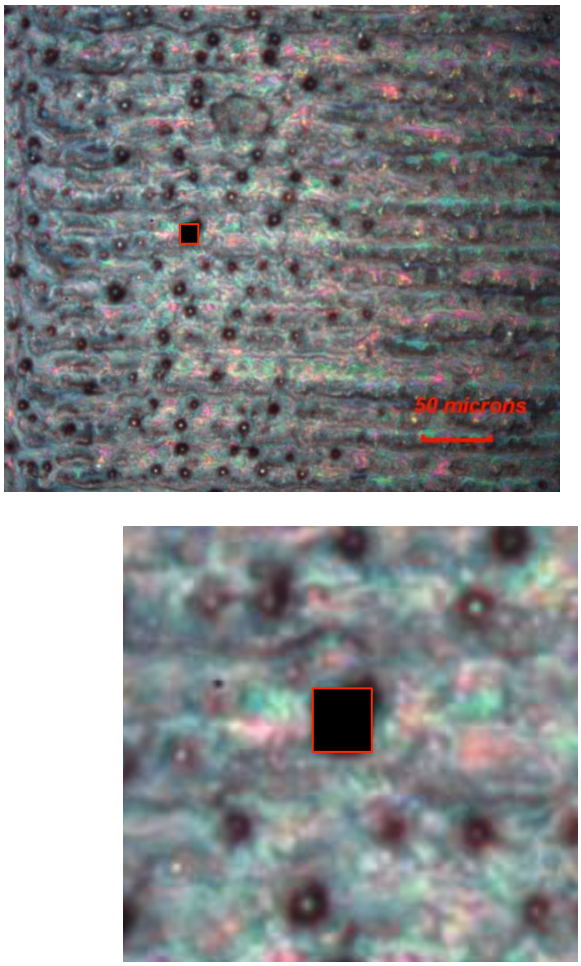

Figure 95. Optical images of a laser colored area having embedded, color islands of dimension 5-10 μm on average. The highlighted area was sampled using the UV-Vis-IR microspectrophotometer to produce the spatially resolved reflectance maps included in the next figure. Note, this area partially includes a color island.

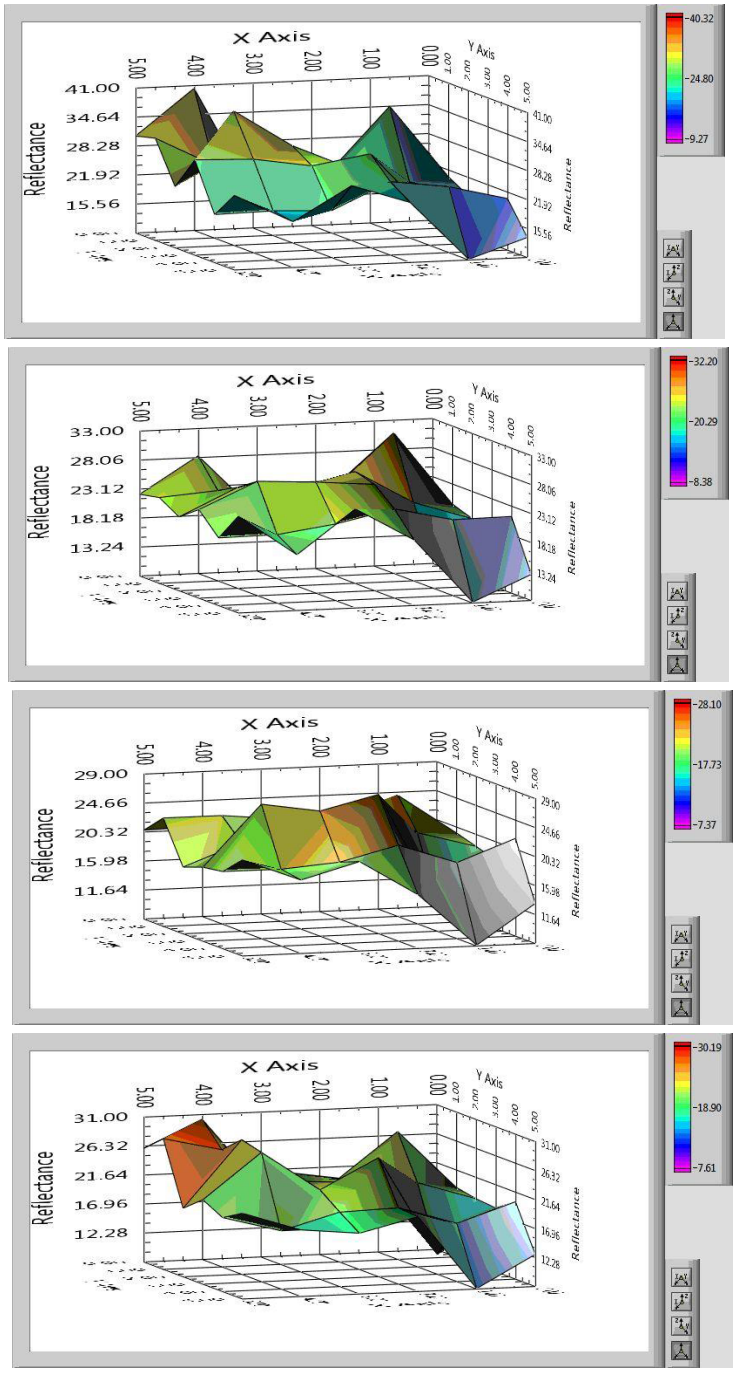

λ = 700 nm

λ =650 nm

λ =600 nm

λ = 550 nm

Figure 96. Spatially resolved color/reflectance maps of a laser-treated stainless steel sample containing micron-scale color islands. A single island (of low average reflectance) is included in the bottom right corner of these maps.

A full spectral analysis was completed on islands and this was compared with surrounding areas (treated with equal laser fluence). In general, the islands exhibited a low average reflectance with a minima in the range of 450 to 650 nm. An example of this is shown in Figure 97 with the lower (black) curve showing the results obtained from one representative island. A spectra obtained from surrounding, non-islanded regions is shown in green (#1).

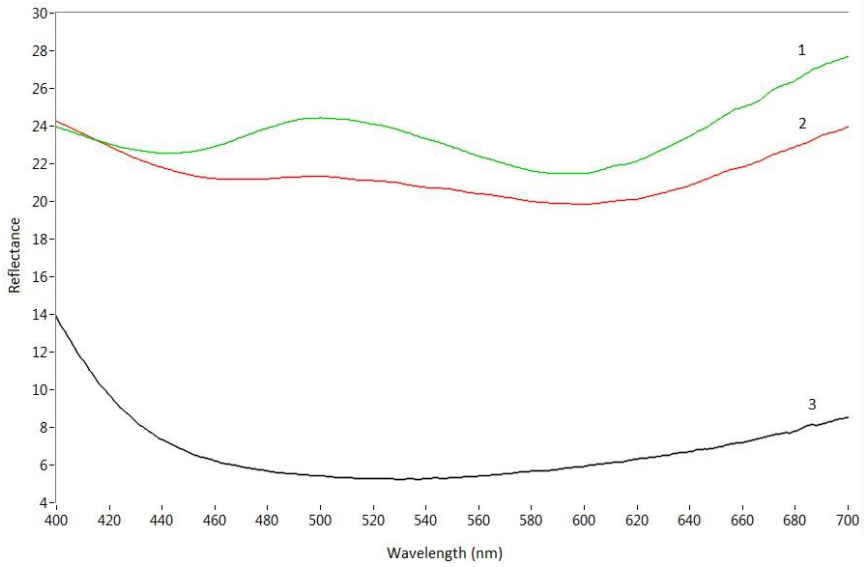

Figure 97. Spectral reflectance of two laser-treated stainless steel samples. The red curve is obtained from sampling a large area of a specimen not having color islands. The green and black curves are obtained from a sample containing micron-scale color islands, wherin the black curve (#3) is obtained from a single island and the green curve (#1) is obtained from large area scans of surrounding areas.

The green and red curves obtained from large-area scans show multiple interference maxima at different wavelengths compared with that formed on islands. Multiple maxima in curve #1 (green) suggest a much thicker oxide in areas surrounding islands compared with the oxide thickness associated with islands. This is consistent with the information provided by cross section scanning electron microscopy shown earlier. The chromaticities of islands (and surrounding regions) derived from spectra such as these are included in a plot (Figure 98). These

are shown with red circles. The average chromaticity of the entire colored feature is shown with a "+" symbol. Dfferences are observed in additional to detectable difference in spectral reflectance. Color differences are detectable using this methodology.

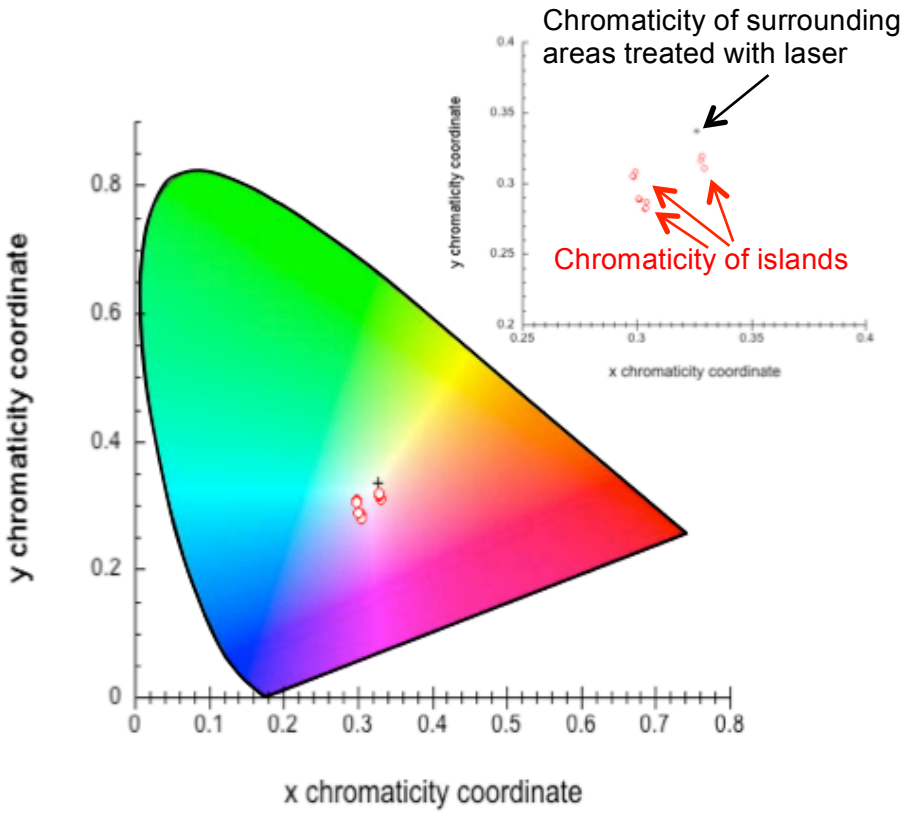

Figure 98. Chromaticities derived from microspectrophotometry. This includes results for color islands and surrounding oxides produced using equivalent fluence.

6.2. Methods for Interrogating Ripple Patterns

Ripple patterns (such as the one in Figure 98) can be interrogated using light diffraction, interferometic microscopy or more involved methods such as atomic force microscopy. This particular ripple pattern is isolated from other rippled areas (and formed near an asperity on the original surface) making it amenable for rapid location and characterization. In terms of documented characteristics of this pattern, there is a dominant wavevector that is aligned with the electric field vector of the polarized light. The average wavelength of the ripple pattern is also readily extracted.

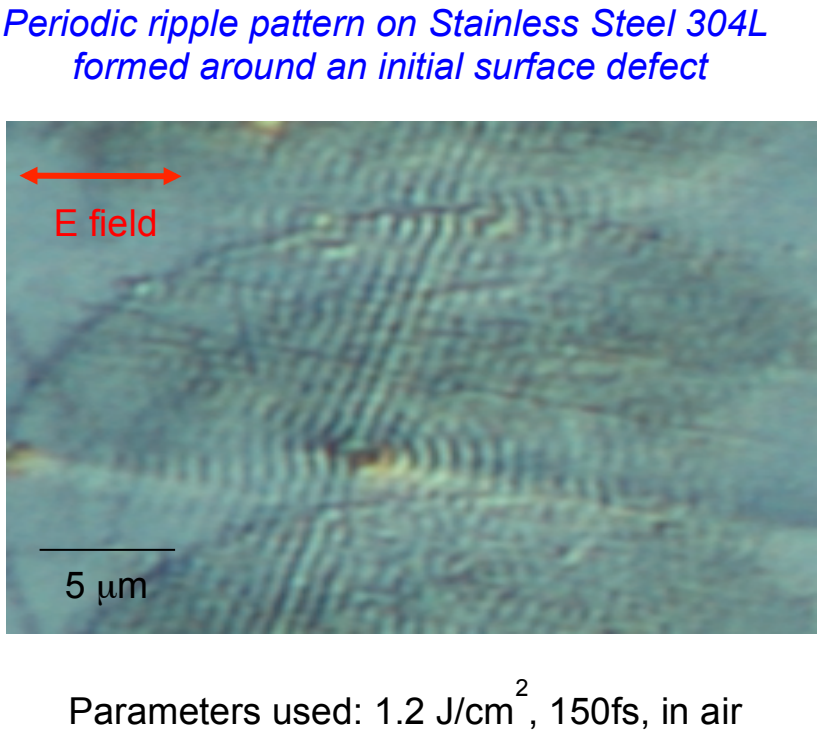

Figure 99. Example of local ripple pattern formed near an asperity on a stainless steel surface.

7. PUBLISHED PAPERS, PRESENTATIONS AND PATENT

The papers published from this research include the following:

Environmental Resistance of Oxide Tags Fabricated on 304L Stainless Steel via Nanosecond Pulsed Laser Irradiation, S.K. Lawrence, D.P. Adams, N.R. Moody, D.F. Bahr, Surf. & Coat., **285**, 87-97 (2015). DOI: 10.1016/j.surfcoat.2015.11.021

Nanosecond pulsed laser irradiation of titanium: Oxide growth and effects on underlying metal, D.P. Adams, R.D. Murphy, D.J. Saiz, D.A. Hirschfeld, M.A. Rodriguez, P.G. Kotula, B.H. Jared, Surf. & Coat. **248**, 38-45 (2014).

Polarization dependent formation of femtosecond laser-induced periodic surface structures near stepped features, R.D. Murphy, B. Torralva, D.P. Adams, S.M. Yalisove, Appl. Phys. Lett. **104(23)**, Art. 231117 (2014).

Mechanical and electromechanical behavior of oxide coatings grown on stainless steel 304L by nanosecond pulsed laser irradiation, S.K. Lawrence, D.P. Adams, D.F. Bahr, N.R. Moody, Surf. & Coat. Tech. **48(11**), 4050-4058 (2013).

Pump-probe imaging of laser-induced periodic surface structures after ultrafast irradiation of Si, R.D. Murphy, B. Torralva, D.P. Adams, S.M. Yalisove, Appl. Phys. Lett. **103(14)**, Art. 141104 (2013).

Deformation and fracture of a mudflat-cracked, laser-fabricated oxide on Ti, S.K. Lawrence, D.P. Adams, D.F. Bahr and N.R. Moody, J. Mater. Sci. **48(11)**, 4050-4058 (2013).

Laser induced periodic structure formation resulting from single-pulse ultrafast irradiation of Au microstructures on a Si substrate, R.D. Murphy, B. Torralva, D.P. Adams and S.M. Yalisove, Appl. Phys. Lett. **102(21)**, Art. 211101 (2013).

Nanosecond pulsed laser irradiation of stainless steel 304L: Oxide growth and effects on underlying metal, D.P. Adams, V.C. Hodges, D.A. Hirschfeld, M.A. Rodriguez, J.P. McDonald, and P.G. Kotula, Surface & Coatings Technology **222** 1-8 (2013).

An additional paper is pending review:

The sensitivity of laser-grown Ti-oxide system optical properties to layer composition and structure, R.D. Murphy, D.J. Saiz, M.A. Rodriguez, P.G. Kotula, D.P. Adams, *submitted to* Appl. Surf. Sci. (2015).

The following presentations were delivered as part of this research:

Award #	Presentation Type	Presentation (Paper) Title	Conference Date	Conference Name	Conference Location City, State	Author(s)	Personnel Type	Acknowledgement of DTRA Support
IACRO14-XXXXX	***Poster***	Structural Dependence and Mechanisms of LIPSS Formation at a Step Edge due to Single-pulsed Femtosecond Laser Irradiation	2/10/15	SPIE Photonics West	San Francisco, CA	R.S. Cahyadi, B. Torralva, S.M. Yalisove, D.P. Adams, R.D. Murphy	Student	Yes
IACRO14-XXXXX	***Oral***	Development of Mechanically and Environmentally Stable Oxide Coatings using Pulsed Laser Irradiation	10/13/14	Mat. Sci. Tech. 2014	Pittsburgh, PA	S.K. Lawrence, D.P. Adams, D.F. Bahr, N.R. Moody	Student	Yes
IACRO14-XXXXX	***Oral - Invited***	Assessing the Role of Adhesion and Fracture on the Performance of Thin Film Systems	10/12/14	Mat. Sci. Tech. 2014	Pittsburgh, PA	N.R. Moody, M.J. Cordill, M.S. Kennedy, D.P. Adams, E.D. Reedy, D.F. Bahr, W.W. Gerberich	Staff	Yes
IACRO14-XXXXX	***Poster***	Development of Mechanically and Environmentally Stable Oxide Coatings using Pulsed Laser Irradiation	7/11/14	Gordon Research Conference on Thin Film and Small Scale Mechanical Behavior	Waltham, MA	S.K. Lawrence, D.P. Adams, D.F. Bahr, N.R. Moody	Student	Yes
IACRO 13-5897I	***Poster***	Ellipsometric analysis of Laser Fabricated Oxides on Titanium	6/2/14	Surface Analysis 2014	Albuquerque, NM	R.D. Murphy, D.P. Adams, D.J. Saiz, R.S. Goeke	Post Doc	Yes
IACRO 13-5897I	***Oral***	Electromechanical and Chemomechanical Performance of Laser Oxide Coatings on Metallic Substrates	4/28/14	Intern. Conf. on Metall. Coatings and Thin Films	San Diego, CA	S.K. Lawrence, D.P. Adams, D.F. Bahr, N. Moody	Student	Yes
IACRO 13-5897I	**Poster**	Stability of Colored Oxide Films fabricated on Titanium	10/3/13	Rio Grande Symposium on Advanced Materials	Albuquerque, NM	G. Neiser, D.P. Adams, D. Saiz, R.D. Murphy, M. Rodriguez	Student	Yes
IACRO (12-2026I)	***Oral Invited***	Identification Tags created by Laser Color Marking	11/14/12	ASM-ASME Local Chapter Symposium	Albuquerque, NM	D. Hirschfeld, D.P. Adams	Research Associate/Scientist	Yes
IACRO (12-2026I)	***Oral***	Deformation and Fracture of Wear-Resistant Laser Oxide Coatings on Metallic Substrates	5/1/13	Intern. Conf. on Metall. Coatings and Thin Films	San Diego, CA	S. Lawrence, D.P. Adams, D. Bahr, N. Moody	Graduate Student	Yes
IACRO (12-2026I)	***Oral***	The Role of Surface Plasmon Polariton Excitation in Periodic Structure Formation after Single Shot Ultrafast Irradiation	6/11/13	2013 Conference on Lasers and Electrooptics (CLEO)	San Jose, CA	R.D. Murphy, B. Torralva, D.P. Adams, S.M. Yalisove	Post-Doc	Yes
IACRO (12-2026I)	***Oral***	Nanosecond Pulsed Laser Color Marking of Titanium: Analysis of Oxide Layer Phase	6/10/13	2013 Conference on Lasers and Electrooptics (CLEO)	San Jose, CA	D.P. Adams, R.D. Murphy, D. Saiz, M.A. Rodriguez, D. Hirschfeld	Staff	Yes
IACRO (12-2026I)	***Oral***	Formation of Laser Induced Periodic Structures in Si and Au after the Ultrafast Irradiation of Au Nanostructures	11/29/12	Materials Research Society Fall Meeting	Boston, MA	R.D. Murphy, B. Torralva, D.P. Adams, S.M. Yalisove	Graduate Student	Yes
IACRO (12-2026I)	***Oral***	Size and Environmental Effects on Fracture of Wear-Resistant Oxide Coatings	3/5/2013	TMS Annual Meeting	San Antonio, TX	S.K. Lawrence, D.P. Adams, N.Moody, D.F. Bahr, H.M. Zbib	Graduate Student	Yes
IACRO (12-2026I)	***Oral***	Mechancial and Electrochemical Behavior of Laser-Fabricated Oxides on Stainless steel	3/18/13	Corrosion 2013	Orlando, FL	S.K. Lawrence, D.P. Adams, N.Moody, D.F. Bahr, H.M. Zbib	Graduate Student	Yes
IACRO (12-2026I)	***Oral***	Electromechanical Behavior and Environmental Resistance of Laser Fabricated oxides on Stainless Steel	6/26/13	SSGF 2013 Annual Meeting	Santa Fe, NM	S.K. Lawrence, D.P. Adams, D.F. Bahr, N. Moody	Graduate Student	Yes
IACRO (12-2026I)	***Poster***	Formation of Laser Induced Periodic Structures	5/22/13	AVS NM Chapter Symposium	Albuquerque, NM	R.D. Murphy, B. Torralva, D.P. Adams, S.M. Yalisove	Post-Doc	Yes
IACRO (12-2026I)	***Poster***	Deformation and Fracture of Laser-Fabricated Oxides on Metallic Substrates	11/27/12	Materials Research Society Fall Meeting	Boston, MA	S.K. Lawrence, D.P. Adams, D.F. Bahr, N. Moody	Graduate Student	Yes

Continued on next page

IACRO (12-2026I)	***Poster***	Relative Humidity Effects on Pulsed Laser Oxide Growth	5/22/13	AVS NM Chapter Symposium	Albuquerque, NM	D.J. Saiz, D.P. Adams, E. Jones Jr. V.C. Hodges, R.D. Murphy	Technician	Yes
IACRO (11-4471I)	***Oral - Invited***	Deformation and Fracture of of Pulsed Laser Oxides on 304L Stainless Steel	1/5/12	18th International Symposium on Plasticity	San Juan, PR	N.R. Moody, D.P. Adams, S.K. Lawrence, D.D. Stauffer, W.W. Gerberich, D.F. Bahr	Staff	Yes
IACRO (11-4471I)	***Poster***	Deformation and Fracture of Colored Laser-Fabricated Oxides on Titanium	7/23/12	Gordon Research Conference on Thin Film and Small Scale Mechanical Behavior	Waterville, ME	S.K. Lawrence, N.R. Moody, D.P. Adams, D.F. Bahr	Student	Yes
IACRO (11-4471I)	***Poster***	Colorization by Pulsed Laser Irradiation	10/20/11	Rio Grande Symposium on Advanced Materials	Albuquerque, NM	D.J. Saiz, D.P. Adams, V.C. Hodges, E.D. Jones, Jr., D. Hirschfeld	Technician	Yes
IACRO (11-4471I)	***Poster***	Deformation and Fracture of Pulsed Laser Oxides	11/29/11	Materials Research Society Symposium	Boston, MA	S.K. Lawrence, D.D. Stauffer, R.C. Major, D.P. Adams, W.W. Gerberich, D.F. Bahr, N.R. Moody	Student	Yes
IACRO (11-4471I)	***Poster***	Delamination Dynamics of compliant Substrate Systems	11/30/11	Materials Research Society Symposium	Boston, MA	D.D. Stauffer, D.J. Sprouster, S. Bhowmick, D.P. Adams, N.R. Moody, R.C. Major	Student	Yes
IACRO (11-4471I)	***Oral***	Time Evolution of Periodic Structures induced by Femtosecond Laser Pulses	11/30/11	Materials Research Society Symposium	Boston, MA	R.D. Murphy, M.J. Abere, B. Torralva, D.P. Adams, S.M. Yalisove	Student	Yes
IACRO (11-4471I)	***Oral***	Deformation and Fracture of Pulsed Laser Colorized Oxides on Stainless Steel	3/11/12	TMS Annual Meeting	Orlando, FL	S.K. Lawrence, N.R. Moody, D.P. Adams, D.D. Stauffer, R.C. Major, D.F. Bahr, W.W. Gerberich	Student	Yes

Several presentations were awarded with top prizes as follows:

1. Graduate Student Award Winner for best Paper (2nd place), International Conference on Metallurgical Coatings and thing Films, Samantha Lawrence (Purdue University), 4/28/14. Weblink: www2.avs.org/conferences/icmctf/pdgs/program.pdf

2. Graduate Student /Technologist Award Winner for best Poster (1st place), American Vacuum Science NM Chapter Symposium, Ryan Murphy (University of Michigan), 5/21/13.

3. Undergraduate Student Award Winner for best Poster (1st place), Rio Grande Symposium of Advanced Materials, Geneva Neiser (New Mexico School of Mines and Technology), 10/7/13. Weblink: www.nm-materials.org/RGSAM/RGSAM_2013/index.html

4. Graduate Student /Technologist Award Winner for best Paper (1st place), American Vacuum Science NM Chapter Symposium, David Saiz (Technologist, Sandia Labs), 5/22/12.

A single U.S. patent was awarded for this research. Information as follows:

1. *Method of Intrinsic Marking*, D.P. Adams, J. McDonald, B.H. Jared, V. Carter Hodges, D. Hirschfeld, D.S. Blair. US Patent # 8,685,599 April 1, 2014.

8. STUDENT METRICS

Three students were involved with this basic research. This includes Ryan Murphy (Graduate Student, University of Michigan), Samantha Lawrence (Graduate Student, first at Washington State University and then Purdue University) and Geneva Neiser (Undergraduate Student, New Mexico Institute of Mines and Technology). Ryan Murphy and Samantha Lawrence completed their PhDs in Applied Physics and Materials Science/Engineering, respectively, in large part due to the funding provided by this project. Ryan was granted his PhD on 1/15/13; his advisor was Prof. Steven Yalisove. Samantha was granted a PhD on 5/1/13; her advisor was Prof. (Dept. Chair) David Bahr. Geneva is planning to complete her Master's degree in May, 2016. All three students won awards for their presentations and posters (see the previous section of this Final Report for details). Additionally, Samantha Lawrence was granted a DOE NNSA Stewardship Science Graduate Fellowship. Samantha also participated as a Graduate Student Discussion leader at the Gordon Research Seminar on Thin Film and Small Scale Mechanical Behavior (7/13/14).

9. REFERENCES

1. M. Wautelet, Appl Phys A Mater Sci Process 50 (1990) 131-139.
2. D. Bäuerle, Laser Processing and Chemistry, Third Edition, Springer, Berlin-Heidelberg, 2000.
3. M. Wautelet, L.D. Laude, F. Hanus, K.-H. Heinig, Appl Phys A Mater Sci Process 47 (1988) 313-316.
4. M. Wautelet, R. Andrew, Phil Mag B 55 (1987) 261 - 269.
5. L. Baufay, F.A. Houle, R. Wilson, J Appl Phys 61 (1987) 4640 - 4651.
6. A. Pérez del Pino, J.M. Fernández-Pradas, P. Serra, J.L. Morenza, Surf Coat Technol 187 (2004) 106-112.
7. PDF4+ 2012 database, Manganochromite - $MnCr_2O_4$, entry # 00-054-0876. International Centre for Diffraction Data, Newtown Square, PA.
8. PDF4+ 2012 database, Chromium Iron Oxide - $FeCr_2O_4$, entry # 04-016-4072. International Centre for Diffraction Data, Newtown Square, PA.
9. PDF4+ 2012 database, Magnetite - Fe_3O_4, entry # 00-019-0629. International Centre for Diffraction Data, Newtown Square, PA.
10. H.St.C. O'Neill, W.A. Dollase, Phys Chem Miner 20 (1994) 541-555.
11. P.M. Raccah, R.J. Bouchard, A. Wold, J Appl Phys 37 (1966) 1436 - 1437.
12. E. Winkler, S. Blanco Canosa, F. Rivadulla, M.A. Lopez-Quintela, J. Rivas, A. Caneiro, M.T. Causa, M. Tovar, Phys Rev B 80 (2009) Art. ID 104418.
13. A. Leontyev, A. Semerok, D. Farcage, P.-Y. Thro, C. Grisolia, A. Widdowson, P. Coad, M. Rubel, Fusion Eng and Des 86 (2011) 1728-1731.
14. Handbook of Optical Constants of Solids II, Ed. by E.D. Palik, Academic Press, Boston, 1991.
15. J.D. Rancourt, Optical Thin Films User's Handbook, McGraw-Hill, New York, 1987.
16. A. Schlegel, S.F. Alvardo, P. Wachter, J Phys C Solid State Phys, 12 (1979) 1157-1164.
17. R.W.G. Hunt and M.R. Pointer, Measuring Colour, 4th Edition, John Wiley & Sons, Hoboken, New Jersey, 2011.
18. T. Smith, J. Guild, Trans Opt Soc 33 (1931-32) 73-134.
19. H.S. Fairman, M.H. Brill, H. Hemmendinger, Color Res Appl 23 (1997) 11-23.
20. Metals Handbook, Vol. 1 Properties and Selection of Metals 8th Edition, American Society for Metals, Metals Park, Ohio, 1961.
21. R.S. Graves, T.G. Kollie, D.L. McElroy, K.E. Gilchrist, Int J Thermophys 12 (1991) 409-415.
22. A. Siatou, D. Charalambous, V. Argyropoulos, P. Pouli, Laser Chem 2006 Art. ID 85324
23. B.D. Cullity and S.R. Stock, Elements of X-ray Diffraction, 3rd Edition, Prentice Hall, New Jersey, 2001.
24. D.F. Susan, G.A. Knorovsky, C.V. Robino, J.R. Michael, M.A. Rodriguez, M.J. Periocone, Sci Technol Weld Joining 17 (2012) 321-332.
25. PDF4+ 2012 Database Titanium Oxide TiO, entry # 01-071-5272, International Centre for Diffraction Data, Newtown Square, PA, 2012. S. Bartkowski, M. Neumann, E.Z. Kurmaev, V.V. Fedorenko, S.N. Shamin, V.M. Cherkashenko, S.N. Nemonov, A. Winiarski, D.C. Rubie, Phys Rev B, 56 10656 (1997).

26. PDF4+ 2012 Database Titanium Oxide TiO, entry # 01-075-0552, International Centre for Diffraction Data, Newtown Square, PA, 2012. H. Terauchi, J.B. Cohen, T.B. Reed, Phase Transitions 38 (1992) 127.
27. PDF4+ 2012 Database Titanium Oxide Ti2O3, entry # 04-02-0457, International Centre for Diffraction Data, Newtown Square, PA, 2012. V.A. Perelyaev, V.A. Tskhai, V.I. Potorocha, G.P. Shveikin, Inorg Mater 13 (1977) 241.
28. PDF4+ 2012 Database Titanium Oxide TiO2 Rutile, entry # 04-002-0288, International Centre for Diffraction Data, Newtown Square, PA, 2012. F.Y. Galakhov, G.I. Kosulina, I.G. Polyakova, D.P. Romanov, Inorg Mater 27 (1991) 1068.
29. PDF4+ 2012 Database Titanium Oxide TiO2 Anatase, entry # 04-001-7641, International Centre for Diffraction Data, Newtown Square, PA, 2012. Y.E. Roginskaya, V.I. Bystrov, D.M. Shub, Russ J Inorg Chem 22 (1977) 110.
30. PDF4+ 2012 Database Titanium Nitride Ti2N, entry # 00-017-0386, International Centre for Diffraction Data, Newtown Square, PA, 2012. B. Holmberg, Acta Chem Scand 16 (1962) 1255.
31. A. Pérez del Pino, P. Serra, J.L. Morenza, Thin Solid Films 415 (2002) 201-205.
32. A. Pérez del Pino, J.M. Fernández-Pradas, P. Serra, J.L. Morenza, Surf Coat Technol 187 (2004) 106-112.
33. PDF4+ 2012 Database Titanium Nitride TiN, entry # 01-072-2741, International Centre for Diffraction Data, Newtown Square, PA, 2012. A. Christensen, Acta Chem Scand 29 (1975) 563.
34. PDF4+ 2012 Database Titanium Nitride Ti6O, entry # 01-072-1807, International Centre for Diffraction Data, Newtown Square, PA, 2012. L.E. Fykin, V.V. Vavilova, I.I. Kornilov, R.P. Ozerov, S.P. Solov'ev, Dokl. Akad. SSSR, 191 (1970) 96.
35. G. Lütjering, J.C. Williams, A. Gysler, Microstructure and Properties of Materials, Vol. 2 edited by J.C.M. Li, World Scientific Publishing Company, 2000.
36. O. Banakh, P.E. Schmid, R. Sanjines, F. Levy, Surf Coat Technol 151-152 (2002) 272-275.
37. S.P. Denker, J Appl Phys 37(1966) 142-149.
38. J.D. Rancourt, Optical Thin Films User's Handbook, McGraw-Hill, New York, 1987.
39. J.H. Lee, G.E. Jang, Y.H. Jun, Ceram Inter 38 (2012) S661-S664.
40. R.W.G. Hunt, M.R. Pointer, Measuring Colour, 4th edition John Wiley & Sons, Hoboken, New Jersey, 2011.
41. M. Quinten, A Practical Guide to Optical Metrology for Thin Films, Wiley-VCH, Hoboken, NJ, 2012.
42. J. Lausmaa, J. Electron Spectrosc. **81**, 343 (1996).
43. I. Van De Keere, S. Svedhem, H. Högberg, J. Vereecken, B. Kasemo, and A. Hubin, ACS Appl. Mater. Inter. **1**, 301 (2008).
44. Ł. Skowroński, A. J. Antończak, M. Trzcinski, Ł. Łazarek, T. Hiller, A. Bukaluk, and A. A. Wronkowska, Appl. Surf. Sci. **304**, 107 (2014).
45. D. Schmidt, B. Booso, T. Hofmann, E. Schubert, A. Sarangan, and M. Schubert, Appl. Phys. Lett. **94**, 011914 (2009).
46. D. E. Aspnes, J. B. Theeten, and F. Hottier, Phys. Rev. B **20**, 3292 (1979).
47. J. P. Borgogno, F. Flory, P. Roche, B. Schmitt, G. Albrand, E. Pelletier, and H. A. Macleod, Appl. Opt. **23**, 3567 (1984).
48. T. E. Tiwald and M. Schubert, in *Proc. SPIE 4103*, *Optical Diagnostic Methods for Inorganic Materials II,* San Diego, CA, October 11, 2000, pp. 46-57.

49. A. Zhecheva, W. Sha, S. Malinov, and A. Long, Surf. Coat. Tech. **200**, 2192 (2005).
50. S.-H. Lee, E. Yamasue, H. Okumura, and K. N. Ishihara, Appl. Catal. A-Gen. **371**, 179 (2009).
51. D. C. Cronemeyer, Physical Review **113**, 1222 (1959).
52. N. Serpone, J. Phys. Chem. B **110**, 24287 (2006).
53. L. Liborio and N. Harrison, Phys. Rev. B **77**, 104104 (2008).
54. L. Lavisse, D. Grevey, C. Langlade, and B. Vannes, Appl. Surf. Sci. **186**, 150 (2002).
55. D. P. Adams, R. D. Murphy, D. J. Saiz, D. A. Hirschfeld, M. A. Rodriguez, P. G. Kotula, and B. H. Jared, Surf. Coat. Tech. **248**, 38 (2014).
56. M. Baster, F. Bourée, A. Kowalska, and Z. Latacz, J. Alloys Comp. **296**, 1 (2000).
57. J. A. Thornton, Ann. Rev. Mater. Sci. **7**, 239 (1977).
58. A. Atkinson, Rev. Mod. Phys. **57**, 437 (1985).
59. E. D. Palik, *Handbook of Optical Constants of Solids*. (Academic Press, Boston, 1991).
60. I. J.A. Woollam Co., *Guide to Using WVASE32®: Spectroscopic Ellipsometry Data Acquisition and Analysis Software*. (J.A. Woollam Co, Inc., New York, 2010).
61. D. Schmidt, B. Booso, T. Hofmann, E. Schubert, A. Sarangan, and M. Schubert, Optics Letters **34**, 992 (2009).
62. D. E. Aspnes, Thin Solid Films **89**, 249 (1982).
63. W.C. Oliver, G.M. Pharr, J. Mater. Res. **7**, 1564–1583 (1992).
64. D.P. Adams, V.C. Hodges, D.A. Hirschfeld, M.A. Rodriguez, J.P. Mcdonald, P.G. Kotula, Surf. Coat. Technol. **222,** 1–8 (2013).
65. S.K. Lawrence, D.D. Stauffer, R.C. Major, D.P. Adams, W.W. Gerberich, D.F. Bahr, et al., MRS Proceedings. **1424,** 73–78 (2012).
66. S.K. Lawrence, D.P. Adams, D.F. Bahr, N.R. Moody, J. Mater. Sci. **48,** 4050-4058 (2013).
67. R.E. Cuthrell, J. Vac. Sci.Technol. A: Vac, Surf, Films. **6,** 2914 (1988).
68. R. Saha, W.D. Nix, Acta Mater. **50,** 23–38 (2002).
69. W.-G. Jiang, J.-J. Su, X.-Q. Feng, **75,** 4965–4972 (2008).
70. W.C. Oliver, G.M. Pharr, J. Mater. Res. **19,** 3–20 (2004).
71. J.F. Archard, Appl. Phys. A: Mater. Sci. Process. **24,** 981 (1953).
72. T.L. Oberle, JOM, 3, 438 (1951).
73. R.C.D. Richardson, Wear, **11**, 245-275 (1968).
74. A. Leyland, A. Matthews, Wear, **246**, 1-11 (2000).
75. D.F. Bahr, C.L. Woodcock, M. Pang, K.D. Weaver, N.R. Moody, Internat. J. Fract. 119/120 (2003) 339–349.
76. J. Michler, E. Blank, Thin Solid Films. **381** 119–134 (2001).
77. S. Hainsworth, M.. McGurk, T. Page, Surf. Coat. Technol. **102** 97–107 (1998).
78. D. Tromans, J. Mech, Miner. Eng. **15** 1027–1041 (2002).
79. C.J. Boxley, H.S. White, C.E. Gardner, J.V. Macpherson J Phys Chem **107**, 9677-9680 (2003).
80. M. Pang, D.E. Eakins, M.G. Norton, D.F. Bahr Corrosion **57**, 523-531 (2001).
81. H.G. Jiang, M. Rühle, E.J. Lavernia J Mater Res **14**, 549-559 (2011).
82. P. Scherrer Nachr. Ges. Wiss. Göttingen **26**, 98-100 (1918).
83. S. Bartkowski, M.Neumann, E. Kurmaev, V. Fedorenko, S. Shamin, V. Cherkashenko, S. Nemnonov, A, Winiarski, D. Rubie Phys Rev B **56**, 10656-10667 (1997).
84. D. Kramer, H. Huang, M.Kriese, J. Robach Acta Mater **47**, 333-343 (1998).
85. D. Tabor (1951) The Hardness of Metals. Clarendon Press, Oxford.

86. K.R. Morasch, D.F. Bahr Thin Solid Films **515**, 3298-3304 (2007).
87. D.F. Bahr, C.L. Woodcock, M. Pang, K.D. Weaver, N.R. Moody Int J Fract **119/120**:339-349 (2003).
88. J. Li, S. Forberg, L. Hermansson, Biomaterials **12**, 438-440 (1991).
89. B.A. Latella, B.K. Gan, H. Li Surf Coat Technol **201**, 6325-6331 (2007).
90. M.D. Thouless, Ann. Rev. of Mat. 69-96 (1995).
91. R.H.U. Khan, A.L. Yerokhin, A. Matthews, Phil. Mag. **88**, 795-807 (2008).
92. C-C Lee, H-C Chen, C-C Jaing. Appl Optics **45**, 3091-3096 (2006).
93. B. Major, R. Ebner, P. Zieba , W. Wolczynski (1999) Appl Phys A **923**, 921-923 (1999).
94. R. Nowak, D. Chrobak, S. Nagao Nature Nanotechnology **4**, 287-291 (2009),
95. A.F. Holleman, E. Wiberg 2001 Inorganic Chemistry. Academic Press, San Diego.
96. P. Kofstad, 1972, Nonstoichiometry, Diffusion, and Electrical Conductivity in Binary Metal Oxides. Wiley-Interscience, New York.
97. S.K. Lawrence, D.D. Stauffer, R.C. Major, D.P. Adams, W.W. Gerberich, D.F. Bahr, N.R. Moody MRS Proceedings **1424**, 73-78 (2012).
98. H.S. Khatak, B. Raj, Corrosion of Austenitic Stainless steels: Mechanism, Mitigation and Monitoring, Woodhead, Materials Park, OH, 2002.
99. J.R. Davis, Stainless Steels, ASM International, Materials Park, OH, 1994
100. R.V. Trax, J.C. Holzwarth, Corrosion. **16,** 271t–274t (1960).
101. J. E. Sipe, J. F. Young, J. S. Preston, H. M. van Driel, Phys. Rev. B **27**, 1141 (1983).
102. M. Huang, F. Zhao, Y. Cheng, N. Xu, Z. Xu, ACS Nano **3**, 4062 (2009).
103. Z. Guosheng, P. M. Fauchet, A. E. Siegman, Phys. Rev. B **26**, 5366 (1982).
104. J.F. Young, J. E. Sipe, H. M. van Driel, Phys. Rev. B **30**, 2001 (1984).
105. S. Hohm, A. Rosenfeld, J. Kruger, J. Bonse, Appl. Phys. Lett. **102** (2013).
106. J. Reif, F. Costache, M. Henyk, S.V. Pandelov, Appl. Surf. Sci. **197**, 891 (2002).
107. J. Bonse, J. Kruger, S. Hohm, A. Rosenfeld, J. Laser Applications **24** (2012).
108. M.C. Downer, R. L. Fork, C.V. Shank, J. Opt. Soc. Am. B **2**, 595 (1985).
109. A. Brodeur and S. L. Chin, Phys. Rev. Lett. **80**, 4406 (1998).
110. K. Sokolowski-Tinten, J. Bialkowski, A. Cavalleri, M. Boing, H. Schueler, D. von der Linde, 46 (1998).
111. R.D. Murphy. B. Torralva, D.P. Adams, S.M. Yalisove, Appl. Phys. Lett. **102**, 211101 (2013).
112. K. Sokolowski-Tinten, J. Bialkowski, D. von der Linde, Phys. Rev. B **51**, 14186 (1995).
113. J. Bonse, A. Rosenfeld, J. Krüger, J. Appl. Phys. **106** (2009).
114. F. Korte, J. Koch, B. N. Chichkov, Appl. Phys. A **79**, 879 (2004).

DISTRIBUTION

4	MS0959	David P. Adams	1832
1	MS0959	Deidre Hirschfeld	1832
1	MS1371	Dianna Blair	6830
1	MS0899	Technical Library	9536 (electronic copy)


Sandia National Laboratories